MEASUREMENT OF THE CHARGE RATIO OF ATMOSPHERIC MUONS AT THE COMPACT MUON SOLENOID IN EVENTS WITH MOMENTA BETWEEN 5 GEV/C AND 1 TEV/C

By

MICHAEL HOUSTON SCHMITT

A DISSERTATION PRESENTED TO THE GRADUATE SCHOOL
OF THE UNIVERSITY OF FLORIDA IN PARTIAL FULFILLMENT
OF THE REQUIREMENTS FOR THE DEGREE OF
DOCTOR OF PHILOSOPHY

UNIVERSITY OF FLORIDA

2010

To the American soldier – who stands opposed to tyranny, who protects the weak, who carries the beacon of that greatest bastion of liberty the world has ever known; of a shining city on a hill: one nation, unique in history, founded under God, and governed at the consent of the people; that she may never be banished from the earth, nor suffer of the rule of kings

ACKNOWLEDGMENTS

There are many people whom I would like to thank, and without whom I likely would not have reached this happy milestone. I thank my advisor and committee chair, Paul Avery, and former co-advisor Richard Cavanaugh (now at the University of Illinois at Chicago); John Mocko and Darin Acosta, for giving me my first opportunities to do physics as an undergraduate. Also, Ivan Furic; whom I thank for an inspired solution – lighting a path for the last several months of my graduate career (as Rudyard Kipling once wrote, “If you can meet with triumph and disaster \\ and treat those two imposters just the same. . . ”). I thank Bobby Scurlock; my political antithesis, who has provided a constant source of both entertainment and frustration (in addition to the rare piece of good advice), and who – had I not sprained my ankle – I would have beaten once on the hardcourt.

For their leadership and contributions to the charge ratio measurement – I thank Ivan Furic; his student, Nicholas Kypreos; and post-doctoral assistant, Jonatan Piedra. In addition, various others have provided significant support for my work: Dimitri Bourilkov, Bockjoo Kim, Yu Fu, Yujun Wu, and the experts at the High Performance Computing center – in particular, Craig Prescott (who, in addition, taught me practically everything I know about shell programming – when we used to work together doing data production back in the dark ages of Grid computing).

I would like to thank my family for their love and encouragement: my mother, Sue; my two brothers, David and Steve; Beverly and Richard Yerby, and their daughter – my wonderful wife, Heather – without whom I would (at this very moment) likely be disheveled, unshaven, and hunting in the pantry for asian-style noodles to warm for dinner.

TABLE OF CONTENTS

LIST OF TABLES

LIST OF FIGURES

Figure page

Abstract of Dissertation Presented to the Graduate School
of the University of Florida in Partial Fulfillment of the
Requirements for the Degree of Doctor of Philosophy

MEASUREMENT OF THE CHARGE RATIO OF ATMOSPHERIC MUONS AT THE COMPACT MUON SOLENOID IN EVENTS WITH MOMENTA BETWEEN 5 GEV/C AND 1 TEV/C

By

Michael Houston Schmitt

August 2010

Chair: Paul Avery
Major: Physics

The ratio of positive to negative charges in the secondary cosmic muon flux is measured at the Compact Muon Solenoid experiment. Muons with momenta between 5 GeV/c and 1 TeV/c are observed in data collected at ground level or 89 m underground; and found to be a constant $1.2766 \pm 0.0032(stat.) \pm 0.0032(syst.)$ for momenta below 100 GeV/c, and rising with higher momenta. The fraction of charged pions and kaons in the secondary cosmic flux resulting in positive muon production has been estimated, with $f_{\pi^+} = 0.553 \pm 0.005$ and $f_{K^+} = 0.66 \pm 0.06$, respectively. The results presented herein are in good agreement with cosmic ray shower models, consistent with previous measurements, and represent the most precise measurement to date for atmospheric muons up to 500 GeV/c. This is also the first physics measurement involving muons at the completed CMS detector.

CHAPTER 1
COSMIC RAYS

1.1 History

Indirect evidence for the presence of extrasolar radiation on earth was first discovered by Theodor Wulf; the Jesuit priest-turned-physicist of the early 20th century who, in 1910, climbed the Eiffel tower with his newly invented radiation-detecting "electrometer" and found a surprising abundance of radioactivity at the top [1]; more even than at its base. The result was certainly unexpected at the time, since ionizing radiation was believed to be caused entirely by radioactive elements in the ground, or by heavy gases such as Radon (discovered a decade earlier [2]) in the air; and it was therefore assumed radiation should decrease with altitude.

Wulf's result was confirmed and expanded upon by Vector Hess; who, in 1912, conducted a similar experiment at various altitudes using balloons; and found that, above 1 km, a clear inverse relationship existed between altitude and the intensity of ionizing radiation. Hess eliminated the sun as the source of this radiation (by performing his experiment during a solar eclipse), and deduced that 'a radiation of very great penetrating power (likely) enters our atmosphere from above' [3, 4]. Meanwhile, the first evidence for *showering* of this mysterious radiation was uncovered by Domenico Pacini, who observed that ionization intensity seemed to be correlated across spans of distance [5].

Despite mounting evidence that the radiation phenomenon was extrasolar in nature, doubts remained, and in fact the term "cosmic-ray" did not come into usage until 1931, when Robert Millikan first posited that high energy gamma-ray photon radiation may be incident upon the earth from deep space [6]. In 1935, Arthur Compton used correlations between cosmic ray intensity on earth and galactic rotation to provide compelling evidence that at least some of the observed cosmic rays originated beyond our own galaxy [7].

By the end of the decade, it was known that cosmic-rays were made up of *particles* rather than photons; however the "ray" nomenclature stuck [9, 10]. In 1948, examination of particle tracks from cosmic ray events captured in nuclear emulsion photographs taken in balloons at high altitude revealed that *primary* cosmic rays (those incident upon the atmosphere from space), were composed of protons, alpha particles, and a small fraction of heavier atomic nuclei (such as iron). By then, it had been established that the *secondary* cosmic rays (produced by collisions between the primary cosmic particles and gases within the earths atmosphere) consisted of pions (which were only just discovered [11]), muons, electrons, and photons [12].

Although it was widely conjectured as early as the 1960's that cosmic rays were produced in supernova [13, 14], it was difficult to account for the very highest energies observed in the cosmic ray spectrum; and the origin of such cosmic ray events remained a mystery for many years. Roughly four decades later, in 2007, a Japanese team led by Yasunobu Uchiyama studying a supernova using NASA's Chandra laboratory confirmed that a process of amplification of the magnetic field in young supernova remnants can occur, leading to significant cosmic ray energies [15]. Meanwhile, the Pierre Auger Collaboration released findings which showed that the very *highest* momenta cosmic rays arrive on earth from directions highly correlated with nearby active galactic nuclei – where super-massive black holes, with correspondingly enormous magnetic fields, are believed to exist – and are able to accelerate particles to ultra high (PeV-scale) energies [16, 17], though this link is still tentative [18].

1.2 Theory

Cosmic ray particles may be produced in many potential astrophysical processes. Solar flares, supernovae, and black holes emit and accelerate these particles out into the cosmos; where they are likely to continue accelerating under the action of the turbulent magnetic fields of the interstellar medium [19]. The spectrum is composed of

atomic nuclei, mostly hydrogen (bare protons) and helium; in an approximate ratio of 79-15-6 (hydrogen, helium, and all others) above 10 GeV/nucleon, with the relative fraction of heavy nuclei increasing somewhat with energy [20]. The flux of primary cosmic ray particles incident upon the earth follows a simple power law:

$$\Phi = \Phi_0 \cdot E^{-\gamma} \tag{1–1}$$

The spectrum [21] is plotted in Figure 1-1. The spectral index, γ, is found to be 2.7 above 10 GeV and below 1 PeV – multiplying the observed raw spectrum by $E^{2.7}$ yields a detailed look at the energy dependent shape of the spectrum [22], which may be seen in Figure 1-2. The effects of solar winds, and even the earth magnetic field, provide shielding from low energy cosmic rays; resulting in a suppression of the spectrum below 10 GeV. At the highest energies (above 1 PeV) the spectral index increases – from 2.7 to about 3.0. It is speculated that the effectiveness of cosmic ray production mechanisms to accelerate particles diminishes.

The primary cosmic rays bombards the upper atmosphere of earth; producing a shower of pion and kaon mesons as they collide with atmospheric gases. Muons are produced when the pions and kaons decay before they themselves collide in the atmosphere. The spectrum of these muons [20, 23] depends, of course, on the primary spectrum; but also on the two-body decay kinematics of pions and kaons ($\pi, K \rightarrow \mu + \nu$) and on their interactions – it is plotted against momentum in Figure 1-3; again, with the spectral index factor (p_μ^γ, again, with $\gamma = 2.7$) applied to help accentuate the shape.

A parameterization for the spectrum of muons has been derived [25] according to the interactions of primary cosmic ray particles in the earth atmosphere, and on the

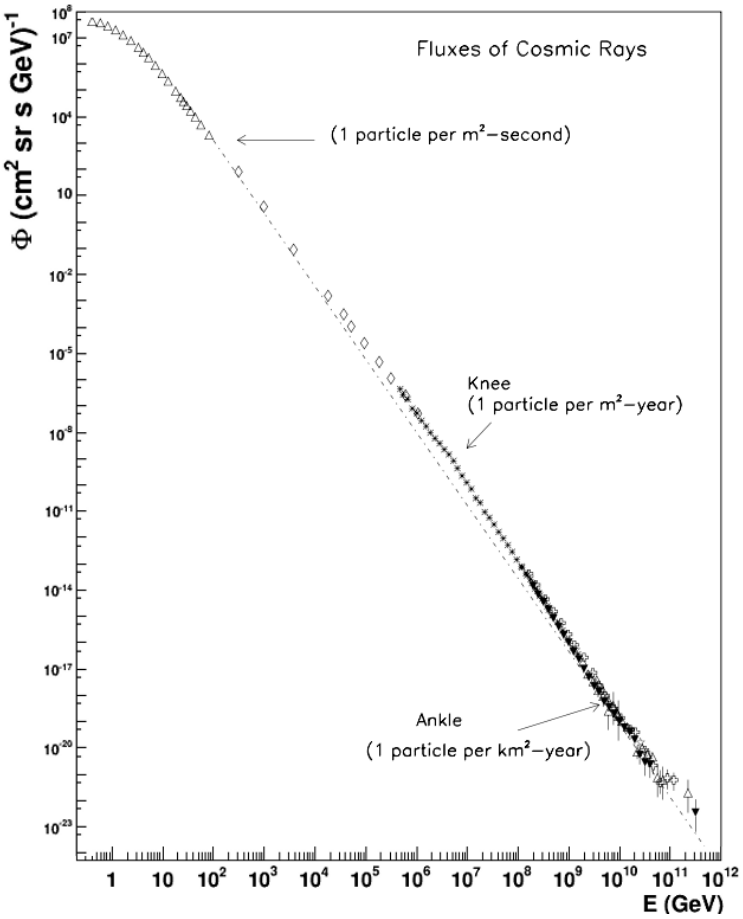

Figure 1-1. The total flux of the incident primary cosmic ray spectrum [21].

decays of the secondary mesons; of which, pions and kaons are the most important contributors. According to this parameterization, the flux may be written:

$$\frac{dN_\mu}{dp_\mu d\Omega} = 0.14 p_\mu^{-2.7} \left(\frac{1}{1 + \frac{1.1 \cdot p_\mu \cdot \cos\theta}{115 \text{ GeV/c}}} + \frac{0.054}{1 + \frac{1.1 \cdot p_\mu \cdot \cos\theta}{850 \text{ GeV/c}}} \right) \text{cm}^{-2} \cdot \text{s}^{-1} \cdot c \cdot \text{GeV}^{-1} \qquad (1\text{–}2)$$

Charge Ratio. Of primary interest to this work is the charge imbalance in the cosmic muon spectrum, expressed as the *charge ratio* of positive to negative muons, as a function of momentum. Because the primary cosmic rays are nearly entirely positively charged, the charge ratio of the incident primaries is very high, and positive meson production is favored; however, as additional pions and kaons are produced, the initial charge imbalance is spread out over larger and larger multiplicities, resulting in a more

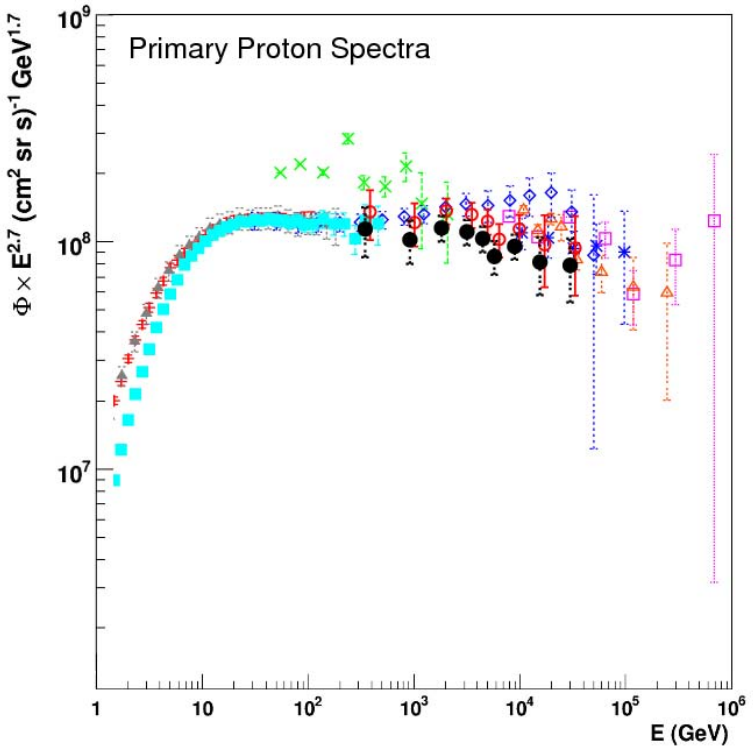

Figure 1-2. The total flux of the incident primary cosmic ray spectrum; scaled by the spectral index factor E^{γ} with γ = 2.7. Adapted from [22].

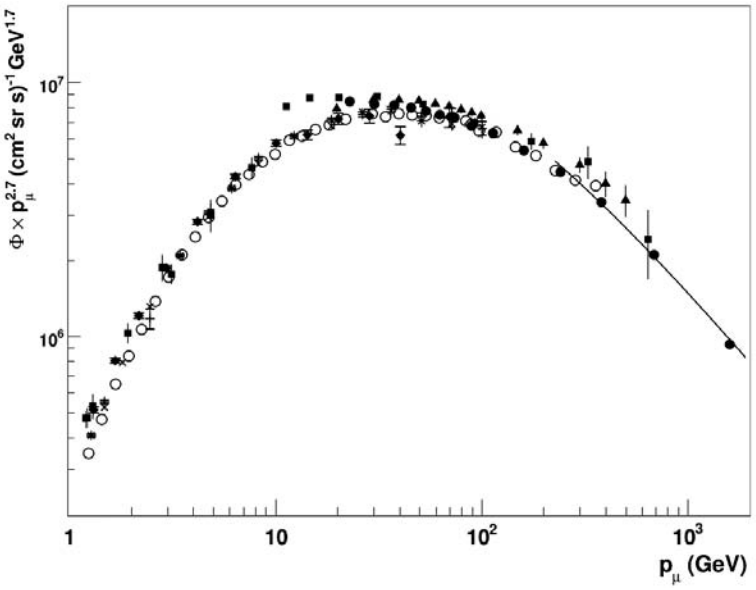

Figure 1-3. The total flux of vertically incident muons in the secondary cosmic ray spectrum at ground level; scaled by p_{μ}^{γ}, with γ = 2.7. Adapted from [20].

uniform charge distribution. Thus, the exact nature of the charge imbalance in muons is sensitive to the production and interaction cross-sections of pions and kaons in the gaseous earth atmosphere, as well as their decay lengths.

Models of cosmic ray showers predict a rise in the charge ratio at higher muon momenta; in part because such muons are likely produced when there are fewer generations between the parent meson and the incident primary cosmic ray; and also because kaon production, which produces relatively more positive muons than pions, becomes much more important at higher energies. There is also some disagreement amongst the models at momenta above several TeV/c; mostly due to the uncertainty associated with interactions of highly energetic pions and kaons with atmospheric protons and neutrons. Several of these models, along with recent experimental results [24], are displayed in Figure 1-4.

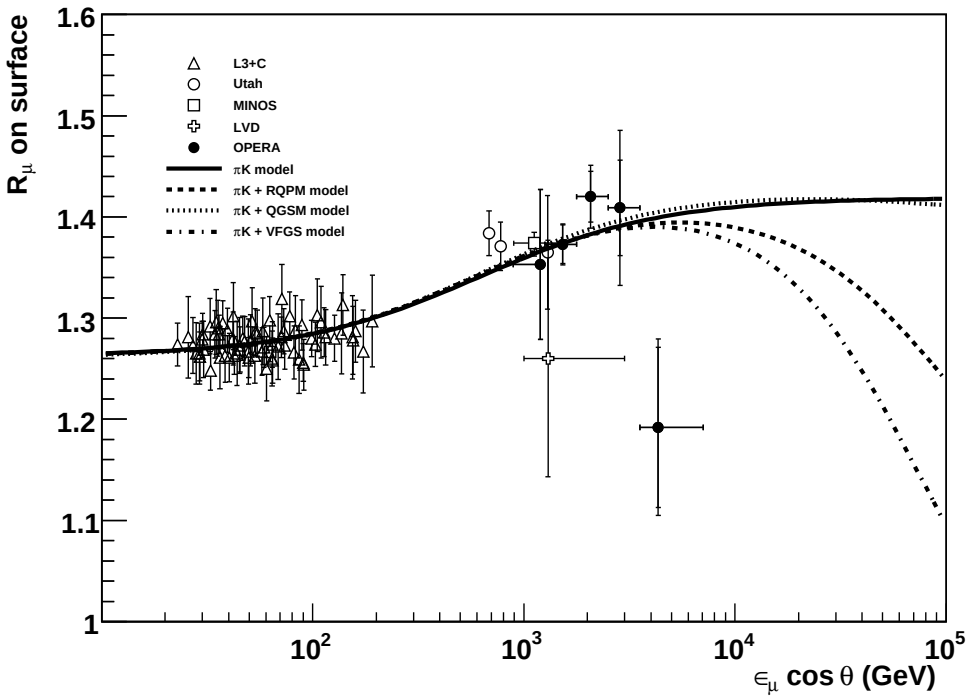

Figure 1-4. Results of the cosmic muon charge ratio from various recent experiments, along with shower model predictions [24].

From the parameterization written in Equation 1–2, the charge ratio may be written [26] as a function of the fractions – f_{π^+} and f_{K^+} – of the ensemble of all charged pion and kaon decays that yield positive muons:

$$\frac{N_{\mu^+}}{N_{\mu^-}} = \left[\frac{f_{\pi^+}}{1 + \frac{1.1 \cdot p_\mu \cdot \cos\theta}{115\ \mathrm{GeV/c}}} + \frac{0.054 \cdot f_{K^+}}{1 + \frac{1.1 \cdot p_\mu \cdot \cos\theta}{850\ \mathrm{GeV/c}}} \right] \Big/ \left[\frac{1 - f_{\pi^+}}{1 + \frac{1.1 \cdot p_\mu \cdot \cos\theta}{115\ \mathrm{GeV/c}}} + \frac{0.054 \cdot (1 - f_{K^+})}{1 + \frac{1.1 \cdot p_\mu \cdot \cos\theta}{850\ \mathrm{GeV/c}}} \right] \tag{1–3}$$

These fractions are not known *a priori*, and must be obtained by fitting the measured data. Obtaining these fractions is one of the chief motivations of measuring the charge ratio in the sub-TeV regime – in particular, because additional data is required in order to determine if these factors will have their own (higher order) momentum dependence. The charge ratio of pion contributions is predicted [27] to be around 1.27 ($f_{\pi^+} = 0.56$); and higher for kaons, due to roughly an order of magnitude smaller likelihood of interaction before decay[1] and because of associated production.

The term “associated production” refers to a particular sort of interaction involving the production of “strange” particles. Strange particles are produced only in pairs in strong nuclear interactions, such that a property – dubbed “strangeness” – is conserved, but decay only via the weak nuclear force. An example of an associated production event is illustrated in Figure 1-5, in which a cosmic proton interacts with an atmosperic proton or neutron, producing a neutral strange hadron (the Λ) and a positively charged kaon. The lambda most likely decays back into a proton plus a negative pion; thus, associated production events such as the one depicted will increase the charge ratio up in kaons.

[1] This is due to: a shorter lifetime (roughly half that of pions, about 12 ns compared with 26 ns); a smaller probability of interacting with protons (about 25%); and a higher mass (roughly three times that of pions), which causes kaons to experience less time dilation than pions for a given amount of kinetic energy, and therefore, a shorter effective lifetime.

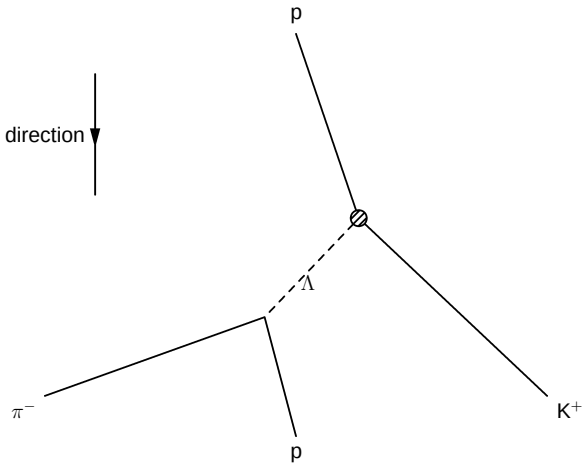

Figure 1-5. Example of an associated production event resulting from primary cosmic ray interactions in the atmosphere, which tends to favor positive kaon production.

1.3 Scope

This work is based on a measurement of the cosmic muon charge ratio, representative of the relative densities of positive and negative muon fluxes, at the Compact Muon Solenoid (CMS); a particle detector built for the Large Hadron Collider (LHC). The LHC, though not used for this measurement, is nonetheless important for this effort[2] from the stand-point of the constraints it puts on detector design and operation. A brief introduction to the LHC is provided in Chapter 2; while the CMS detector is described in Chapter 3.

A total of three analyses have been conducted as part of the cosmic muon charge ratio measurement: one, on data collected while the machine was pre-assembled on the earth surface, and two on data collected after the machine was installed underground. The final result of the charge ratio measurement is a product of all three analyses, and so each are briefly introduced in Chapter 4; however just one of them is the main

[2] As well as a matter of current interest; as it is now, at the time of this writing, operational; and successfully producing controlled collisions at heretofore unseen energies.

focus of this dissertation.[3] The methodology of this analysis is presented in Chapter 5; and estimations on the error are provided in Chapter 6. A detailing of the result from the main analysis is provided in Chapter 7, while the combined results of all three are presented in Chapter 8.

[3] As shall be detailed in the next chapter – this one being based on the underground data and using both the silicon tracker data and the muon spectrometer data, as opposed to solely muon spectrometer data.

CHAPTER 2
THE LARGE HADRON COLLIDER

The Large Hadron Collider [28, 29] is a proton-proton synchrotron built into the existing 27 km long Large Electron Positron Collider tunnel; situated approximately 100 m beneath the ground along the border between France and Switzerland near the city of Geneva. A map of the LHC ring and associated sites is given in Figure 2-1.

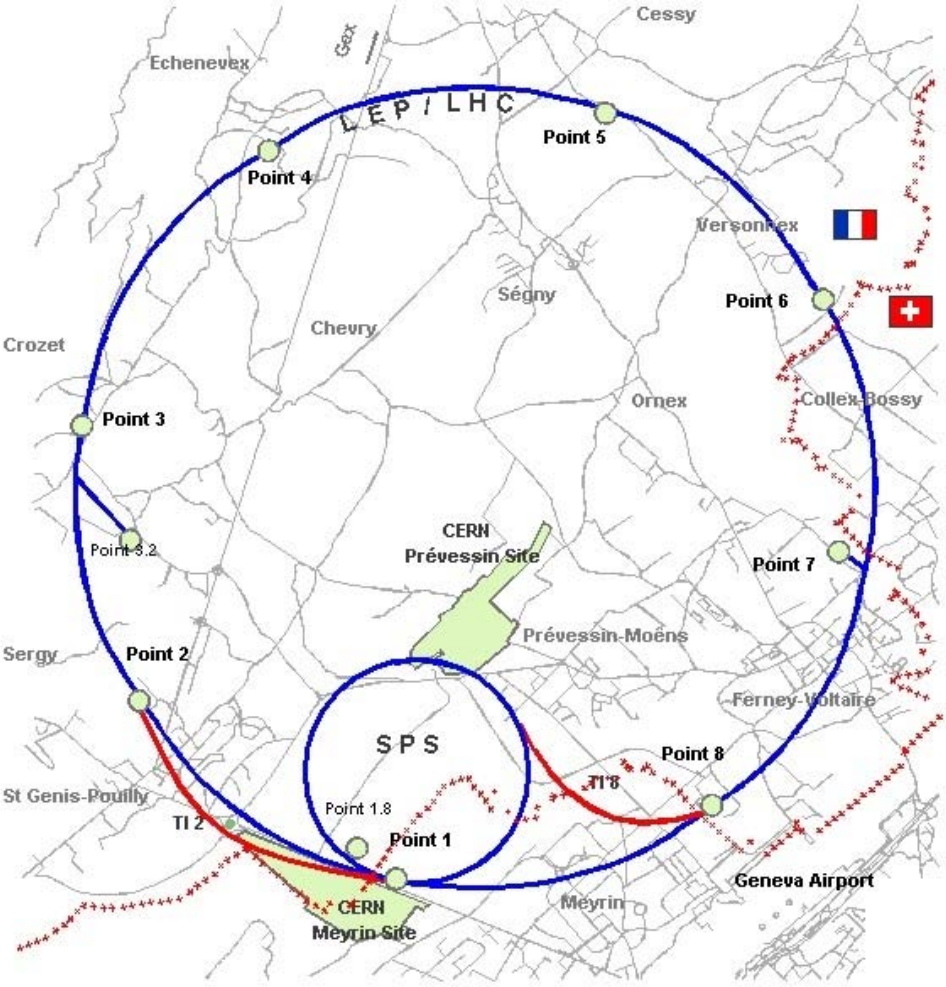

Figure 2-1. Map of the ring and associated CERN sites [30] (CMS, which will be discussed in Chapter 3, is located at Point 5 – near the villages of Cessy and Ségny, in France).

2.1 Member Experiments

The LHC is host to a total of six experiments with four beam crossings (where the collisions are produced); the layout of these experiments may be seen in Figure 2-2.

At Points 5 and 1, respectively, are the Compact Muon Solenoid (CMS)[31, 32] and ATLAS (A Toroidal LHC Apparatus) experiments [33] – which are large, general purpose detectors, with collaborations numbering in the thousands. TOTEM [34] (Total Cross Section, Elastic Scattering and Diffraction Dissociation) is a small, forward[1] physics experiment; which sits nestled partially within, and sharing the collisions produced for, CMS. The smallest of the experiments, LHCf [35] (Large Hadron Collider forward), is designed to study beam remnants[2] and straddles the ATLAS experiment, with detectors placed 140 m in either direction away from Point 1. ALICE [36] (A Large Ion Collider Experiment) is a dedicated heavy-ion experiment[3] located at Point 2. The LHCb [37] (Large Hadron Collider beauty) is a specialized b-physics detector located at Point 8.

2.2 Accelerator chain

Before the LHC can begin accelerating beams of protons to high energies, a complex sequence of must occur in order to deliver the beams to the collider ring. The beam begins as hydrogen gas; from which a duoplasmatron source ionizes and extracts protons. These protons are then accelerated in bunches to 50 MeV by Linac2, a linear accelerator, and fed into one of the four (overlapping) 50 m diameter Proton Synchrotron Booster (PS-Booster) rings, which accelerates the beams to 1.4 GeV. The boosters deliver the beams into the 200 m Proton Synchrotron (PS), which combines the proton bunches and accelerates the beams to 26 GeV. At this point, the bunches are structured such that they are separated by 25 ns in time (or about 8.3 m in distance), and injected into the Super Proton Synchrotron (SPS), the large 6.9 km accelerator ring

[1] Such as soft elastic scattering and diffractive processes.

[2] Which can be used, for example, to model the interactions of cosmic rays in the atmosphere.

[3] The LHC is actually a dual purpose machine, able to be configured for ion colliding as well as for protons.

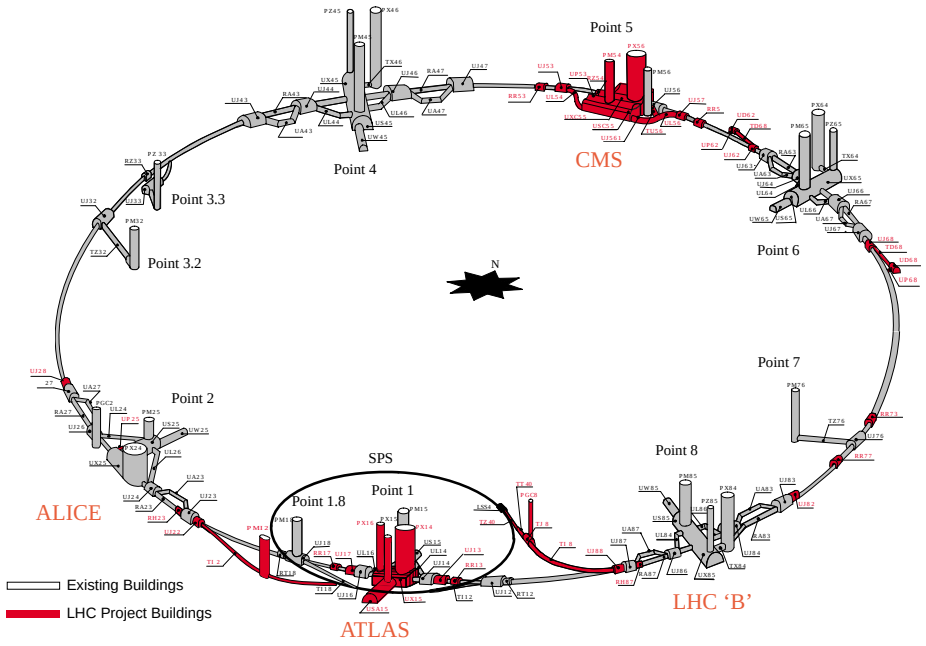

Figure 2-2. Locations of member experiments along the LHC ring.

(which was once a great collider in its own right; having delivered the collisions that led to the discovery of the W and Z bosons) which accelerates the beams from 26 GeV up to 450 GeV – ready for injection into LHC.

New stores of protons must be delivered to the LHC up to several times per day (roughly once every ten hours is expected); since the beam gradually loses particles due to beam-gas collisions, crossing deflections at the interaction points, and other largely unavoidable inefficiencies involved in keeping such a beam intact over several hundreds of millions of orbits. Once fully operational, it is anticipated that acceleration from injection energy (450 GeV) to 7 TeV may occur in as little as 20 minutes.

2.3 Current Operational Status

The Large Hadron Collider successfully circulated beams at its injection energy of 450 GeV for the first time on September 10th 2008, and produced its first collisions on November 23rd, 2009. Just a week later, on November 30th, 2009; the LHC began accelerating proton beams up to 1.18 TeV (for 2.36 TeV total center-of-mass energy

collisions): surpassing the Tevatron at Fermi National Laboratory (with proton and anti-proton beams of 0.98 TeV for a total of 1.96 TeV center-of-mass) to become the world's highest energy particle accelerator, and the most powerful particle collider ever built. On March 30th, 2010; the LHC successfully collided protons at 7 TeV center-of-mass, where it is expected to hold steady for 18 to 24 months. Eventually, the LHC will be able to produce proton-proton collisions at up to 14 TeV; and is expected to deliver an instantaneous luminosity of 10^{34} $cm^{-2}s^{-1}$ at that energy.

CHAPTER 3
THE COMPACT MUON SOLENOID

3.1 Introduction

The Compact Muon Solenoid (CMS) [31] is a general purpose discovery machine built to study collisions produced by the Large Hadron Collider (LHC), part of the European Organization for Nuclear Research (CERN).

The detector is cylindrically shaped; with a diameter of almost 16 m and a length of approximately 21.6 m. In total, it has a mass of approximately 12,500 metric tons.[1] The CMS detector is illustrated in Figure 3-1.

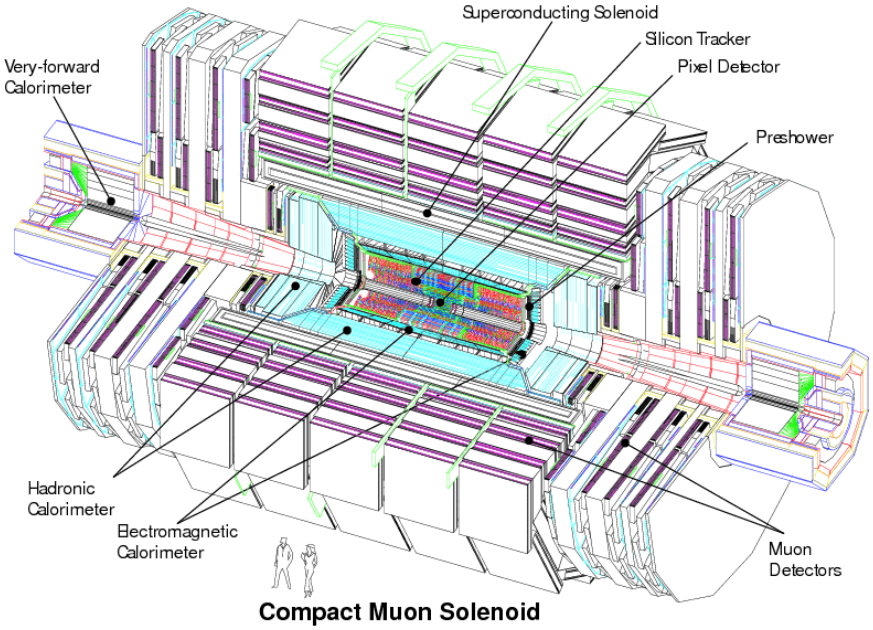

Figure 3-1. Cutaway view of the CMS detector.

It is impossible to directly observe many of the interactions governing subatomic physics, particularly when studying exotic new forms of matter and energy in a collider environment. Most of the observable particles produced in a high energy collision

[1] That is, nearly a quarter as much as the RMS Titanic, which displaced about 52,000 metric tons [38]. The 6000 passenger Oasis of the Seas – the largest cruise ship ever built at the time of this writing – displaces approximately 100,000 metric tons [39].

are not, in fact, direct participants in a collision; nevertheless, sufficiently precise measurements on the observables of those particles (energy, position, mass, etc.) allows for some infererences into the likely nature of the underlying physics. The goal of the CMS detector, then, is to reconstruct the physics of a collision step-by-step; with each layer of subdetectors optimized to perform a particular kind of measurement, while affecting other attributes of the participating particles as minimally as possible (so as not to bias any other measurements).

At the heart of the machine is a helium-cooled superconducting solenoid, which bends the path of charged particles; allowing the momenta of individual charged particles to be estimated precisely from their curvature through the inner tracker and muon spectrometer regions. The detection elements of CMS (working outward from the beam-line) are: an inner tracker consisting of pixels and silicon strips, a scintillating electromagnetic calorimeter, a sampling hadronic calorimeter, and (of particular importance to the flux measurement) muon spectrometers. Also indicated in the figure are the forward calorimeters – a combined electromagnetic and hadronic calorimeter for particles produced close to the beam line – and the preshower detector, which is considered part of the electromagnetic calorimeter system. These systems are illustrated in Figure 3-2.

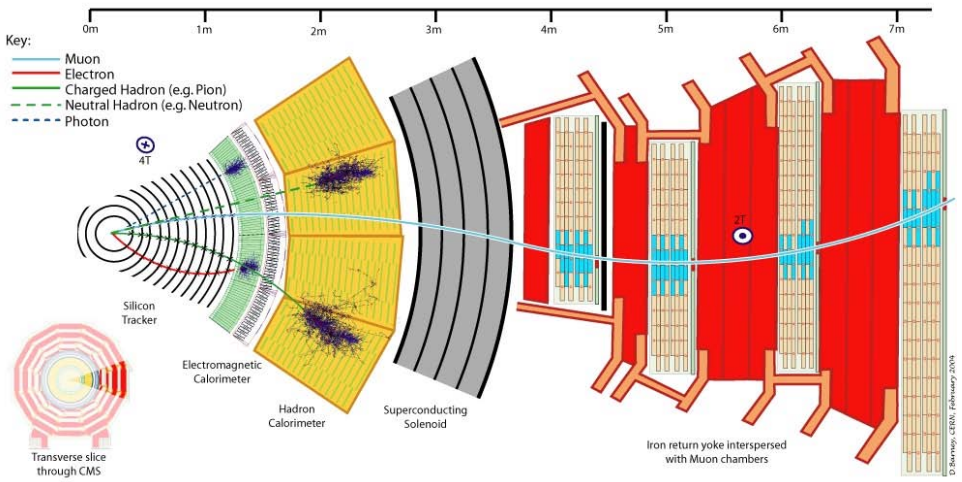

Figure 3-2. A small slice of the CMS detector. The legend indicates where various types of particles can be detected in CMS.

3.1.1 Coordinates and Geography

The detector is located at $46^\circ\,18.57'$ north latitude and $6^\circ\,4.62'$ east longitude. The coordinate system used within the detector environment are defined by the collider ring: the *x*-axis of CMS is defined to point towards the center of the LHC ring, the *y*-axis points upward (it is actually offset by about 0.8°), and the *z*-axis is defined to be parallel with the beam line such that a right-handed coordinate system is formed. Since the detector is located near the northern-most extent of the ring, the *x*-axis points roughly south and the *z*-axis points roughly west.

Common coordinate angles in CMS geometry are the azimuth (angle with respect to the *x*-axis in the *xy*-plane), denoted by ϕ, and the polar angle θ (away from the *z*-axis). Pseudorapidity, η, is frequently used as an approximation of the relativistic rapidity [40] with respect to the beam line (for massless particles originating at the geometric center of the detector); and as a convenient replacement for θ ($\eta = -\ln(\tan\theta/2)$, since particles produced in beam collisions tend to be distributed uniformly in η. Figure 3-3 shows a cross section of the machine in the *xy*-plane, and Figure 3-4 illustrates one quadrant of the *yz*-plane.

3.1.2 Cavern Geometry

Located approximately 100 m under the surface, the main CMS detector cavern measures 51 m long, 27 m across with a 24 m high arched ceiling. Separated by more than 7 m of concrete reinforcements (which also acts as radiation shielding), a second cavern was built to house the computing facilities and support personnel. The layout of the caverns and access shafts constructed for CMS is indicated in Figure 3-5.

CMS is unlike the other major experiments at the LHC in that it was constructed and tested above ground and then lowered by section into the cavern; rather than being assembled underground. While the ATLAS cavern was ready in 2003, the caverns for CMS were not completed until 2005 [41, 42]. Pre-assembling the detector above ground allowed CMS to remain on schedule given the (then anticipated) 2007 start date for

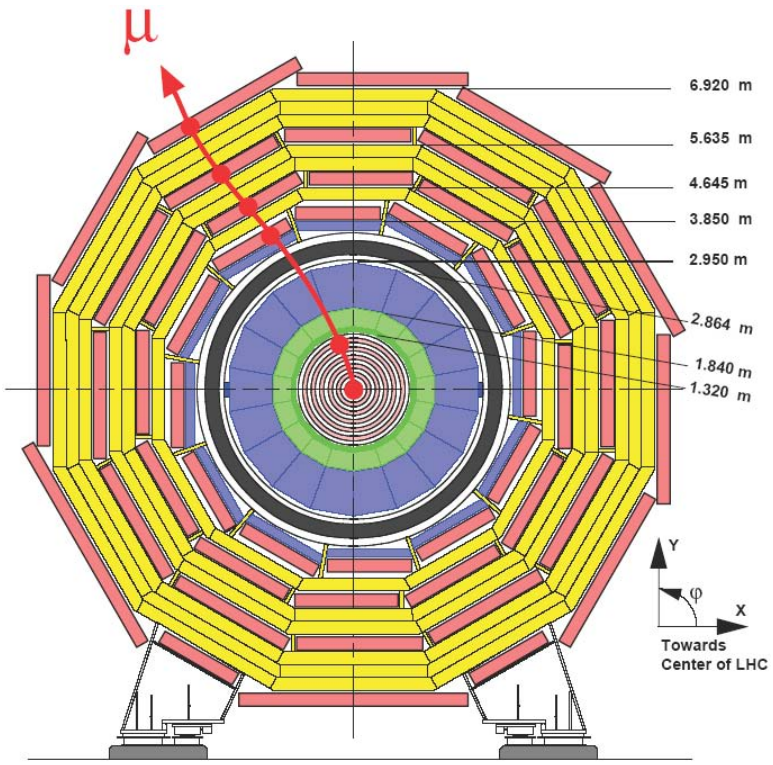

Figure 3-3. Barrel profile of CMS in the *xy*-plane, showing the ϕ coordinate. The changing curvature of the μ track indicates the radius-dependent magnetic field (which reverses direction in the return field outside of the solenoid).

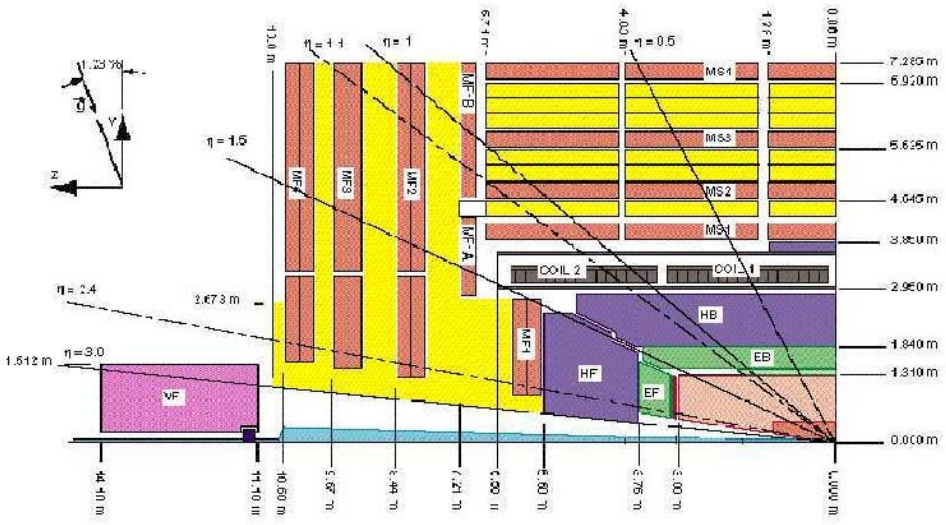

Figure 3-4. Quarter profile of CMS in the *y*-*z* plane, showing the η coordinate. η is a simple function of the polar angle: $\eta = -\ln(\tan\theta/2)$.

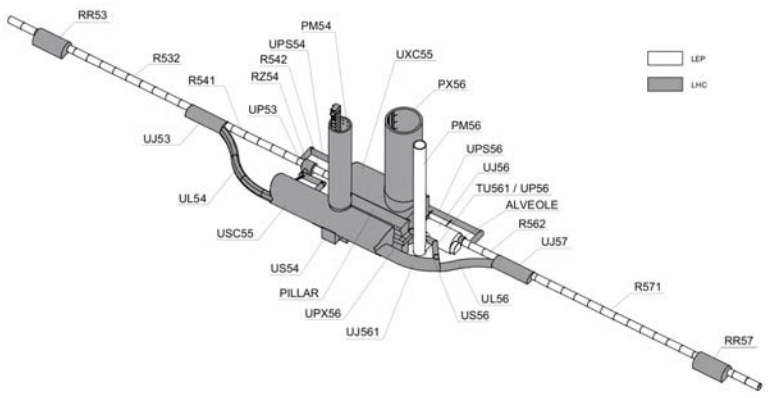

Figure 3-5. The layout of caverns and shafts built to house the CMS experiment [28].

LHC. Photographs of the bare cavern, and of a detector section being lowered, are given in Figure 3-6.

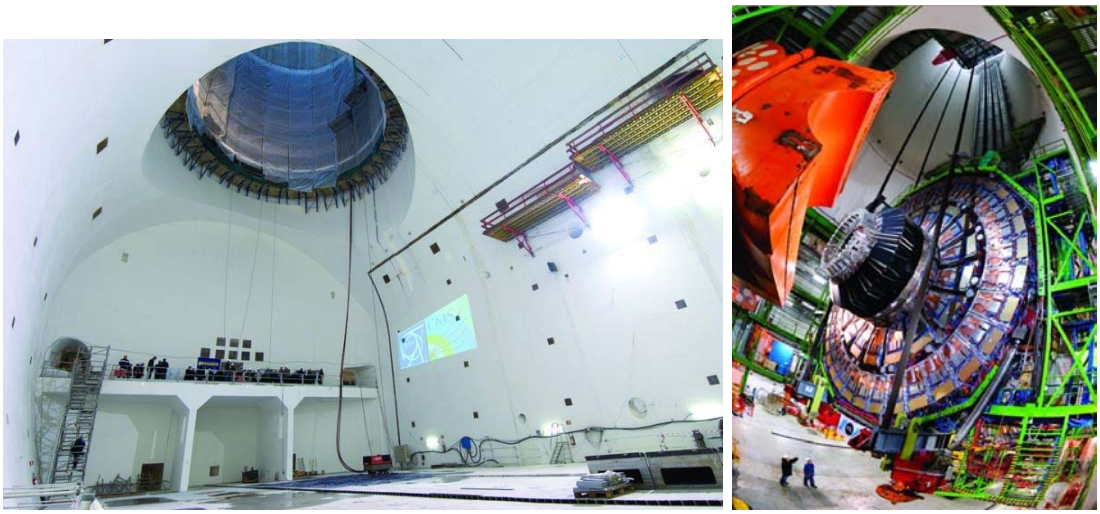

Figure 3-6. Left: the cavern and shaft, just completed. Right: The YE +1 endcap being lowered through the shaft; one of fifteen individually lowered sections of CMS (Copyright CERN [43]).

3.2 Solenoid Magnet

A strong magnetic field is a critical feature requirement of CMS; as it causes charged particles to curve proportionally to their momenta. The 3.8 Tesla magnetic

field[2] of CMS will cause measurable curvature of tracks up to particle momenta of several TeV.

The LN_2 cooled superconducting solenoid magnet is located between the hadronic calorimeter and the muon detectors – it is 12.9 m long, and has a diameter of 5.9 m. The windings of the magnet have a total inductance of 14 H and carry approximately 18,160 A of current. Approximately 2.3 Gigajoules of energy are stored in the magnetic field while it is running [44].

3.3 Inner Tracking System

The silicon tracker systems [45] provide high precision measurements of particle momentum and position close to the interaction point for collision events. The diameter of the tracker, including both subdetectors (pixels and strips), is approximately 2.5 m; and includes 76 million detector channels. In total, it is the largest silicon particle detector ever built; with approximately 205 m^2 of active detection area. The layout of the tracker systems is illustrated in Figure 3-7.

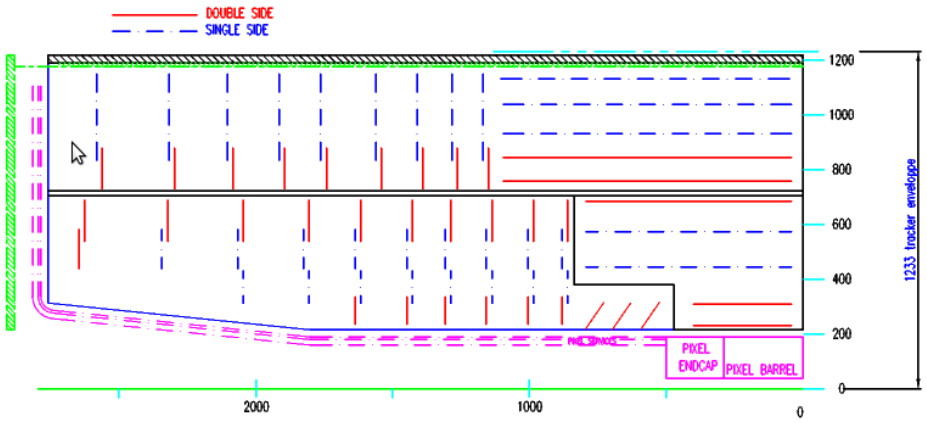

Figure 3-7. Quarter profile schematic of the CMS inner tracker.

[2] The field strength was designed for and is nominally referred to as 4 T, however has been reduced to 3.8 T in order to extend the lifetime of the magnet.

The smallest mass possible is preferable in this system, since added material increases the likelihood of particle showering (which confuses the system's ability to resolve individual tracks, and otherwise complicates possible interpretations of the event) and also absorbs energy that would have otherwise been measured in the calorimeters.

Certain heavy particles that are produced in collisions, such as Charm and Beauty mesons, have relatively long lifetimes; and particles produced in the decay of such particles may originate from a position that is displaced from the primary interaction point. The tracker should be able to make measurements precise enough to allow us to deduce the point of origin of an observed particle; so as to be able to distinguish the decay products of such long-lived particles from promptly decaying particles. This is of particular importance when considering isolated leptons. Isolated leptons are produced sparingly according to the known laws of physics, however are a feature of some theoretical models of new physics. Therefore, in addition to being able to determine whether the lepton originates at the interaction point, the tracker should also be sensitive enough to distinguish a single, isolated particle from two or more particles with highly correlated trajectories.

Finally, and most importantly, the tracker must be designed to operate properly with the requirements of LHC conditions. It needs to work properly within an intense magnetic field, and it absolutely *must* be radiation hard, since it is in such close proximity to the LHC collision point. When operating at design specifications, LHC collisions will produce approximately 1000 energetic particles traversing the tracker volume every 25 ns, coming from more than 20 proton-proton interactions in each beam bunch crossing. In total, an average of 40 billion individual highly energetic particles will traverse the tracker volume *every second*. In addition to sensor toughness, the LHC environment also places tough constraints on the minimum readout speed and sensor occupancy of

the tracker – there must be sufficient channels and rapid enough read-out to avoid track confusion and saturation.

The inner tracker sub-detector is the most crucial sub-detector for precision measurements of the charge ratio, particularly at higher momenta, since it provides extremely accurate tracking in a strong uniform magnetic field.

3.3.1 Pixel Detector

The CMS Pixel sub-detector is an extremely compact system; fitting entirely within a cylinder of about 40 cm diameter and 1 m long. Despite this small size, pixels account for about 65 million of the total 76 million channels of the entire inner tracker. Pixels provide high precision positional information in three dimensions; allowing extremely accurate tracking (resolutions of 10 μm in *r*-ϕ and 20 μm in *z* are possible) close to the beam line. Pixel data is extremely useful for measuring collision and decay vertices (necessary to identify long lived mesons) as well as for fast determinations of particle isolation.

The tracker pixel detectors are arranged into separate barrel (TPB) and end-cap (TPE) regions; with three sensor layers in the barrel (at radii of 4.4 cm, 7.3 cm, and 10.2 cm away from the beam line) and two layers in the end-cap (extending from 6 cm to 15 cm in diameter and located at $\pm$34.5 *cm* and $\pm$46.5 *cm* on the *z*-axis), as illustrated in Figure 3-8.

An individual pixel is 100 μm by 150 μm in size. A pixel module, depicted in Figure 3-9, consists of 52$\times$53 pixels in a sensor array mounted onto a buffered readout circuit. There are a total of 1440 pixel modules in the detector; 768 in TPB and 672 in TPE. In total, there are a total of roughly 40 million pixels, providing 0.92 m^2 of active detector coverage.

In the barrel region, the detector surfaces are parallel to the direction of the magnetic field. Because CMS has such a powerful magnetic field, accumulated charges spread out and are shared amongst pixel channels (the Lorentz Effect). This enhances

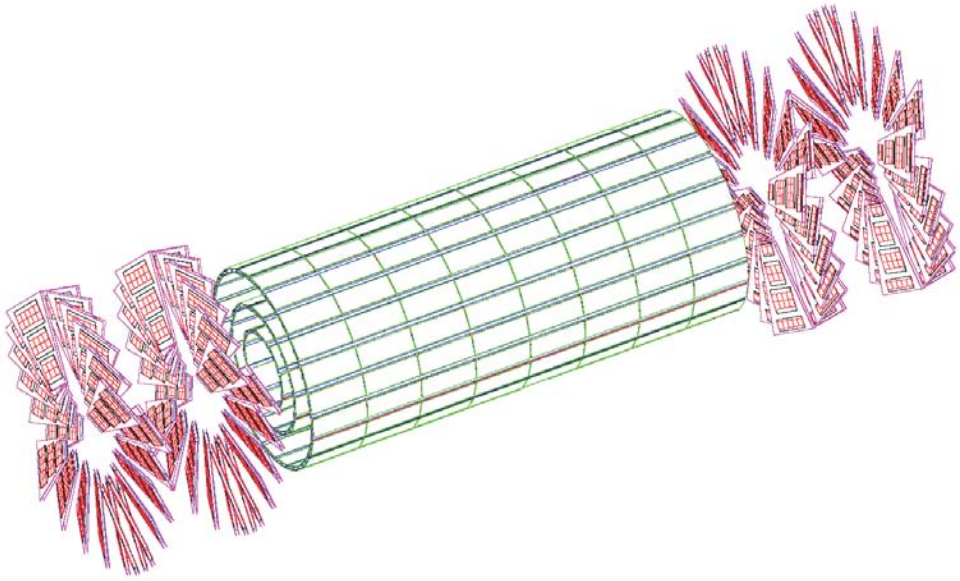

Figure 3-8. Schematic drawing of the Pixel sub-detector.

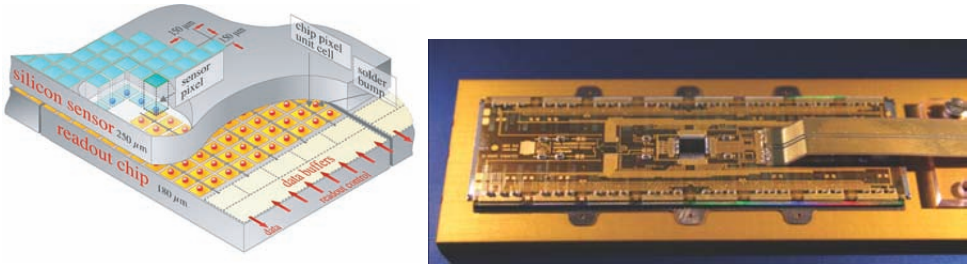

Figure 3-9. Left: diagram of a pixel module. Right: a photograph of a constructed module (Copyright CERN).

position resolution beyond the pixel size, because it allows a centroid to be fit from several neighboring pixels (rather than a binary yes or no for a single pixel). In the end-cap, the magnetic field is perpendicular to the detector layer; therefore, in order to take advantage of the Lorentz Effect, each of the endcap layers is composed of 24 wedges in a "turbine" geometry; with each wedge rotated into the direction of the field by 20°.

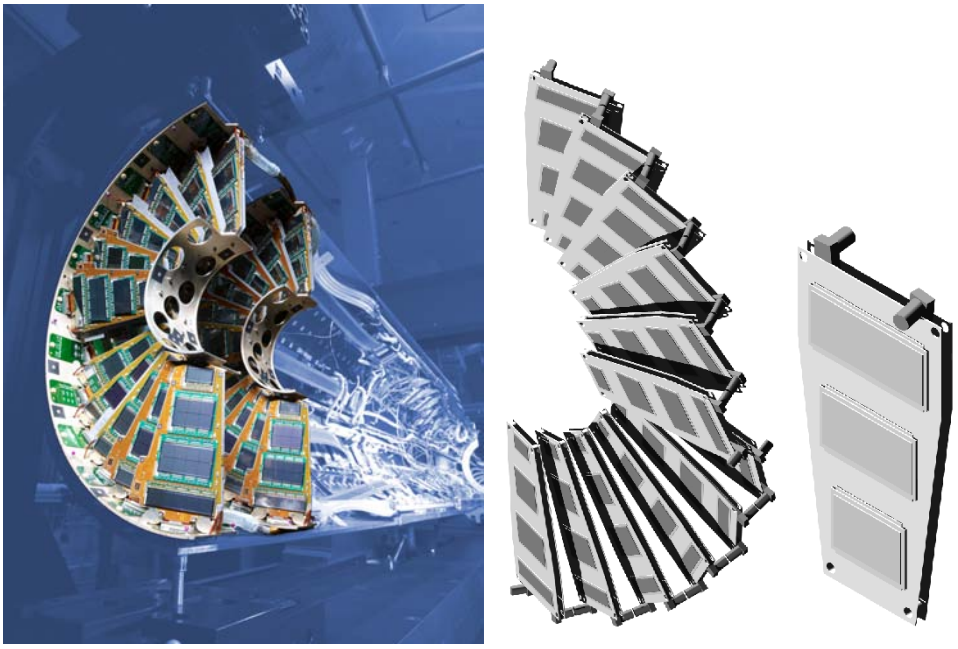

Figure 3-10. Left: photograph of half of one end of TPE before installation into CMS (Copyright Fermilab [46]). Right: illustration of half of an individual pixel endcap disk, along with one of the wedges. By rotating the wedges out of the x-z plane, the Lorentz Effect may be utilized to improve resolutions beyond the pixel size.

3.3.2 Silicon Strip Detector

Further away from the interaction point, where the flux of particles (during collisions) is lower, more coarse detection elements may be used. The strip detector is divided into inner and outer barrel (TIB and TOB, respectively) and end-cap (TEC) regions. The layout of the strips detector is given in Figure 3-11.

Tracker Inner Barrel. TIB ranges between a radius of 20 cm and 55 cm in four layers (the first two of which provide a 100 mrad stereo measurement); and extends to $z = \pm 65$ cm. The cell sizes vary, but are a relatively lengthy 7-12.5 cm by 80 μm.

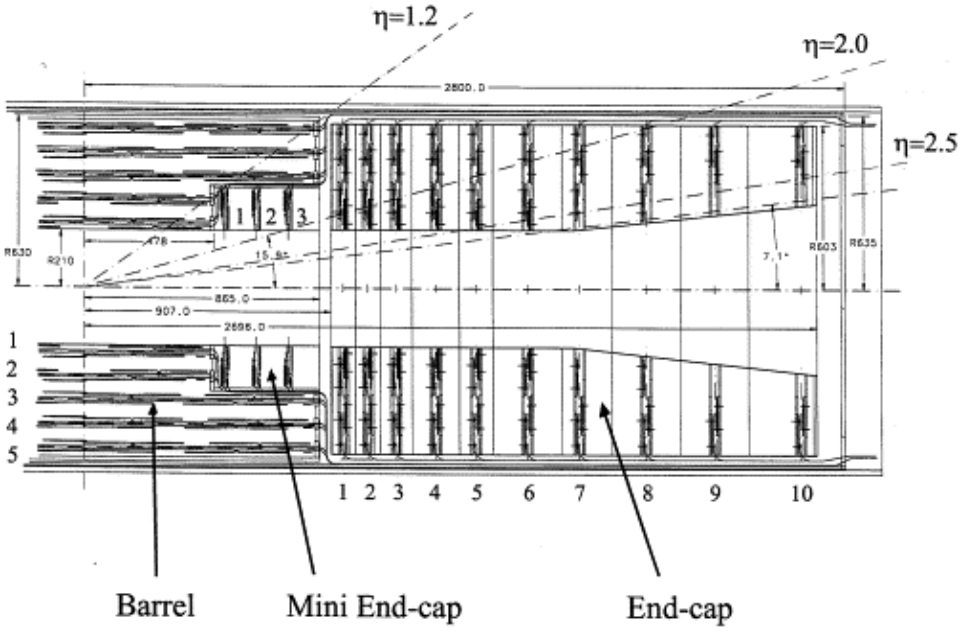

Figure 3-11. Cutaway view showing one half of the silicon strip subdetector.

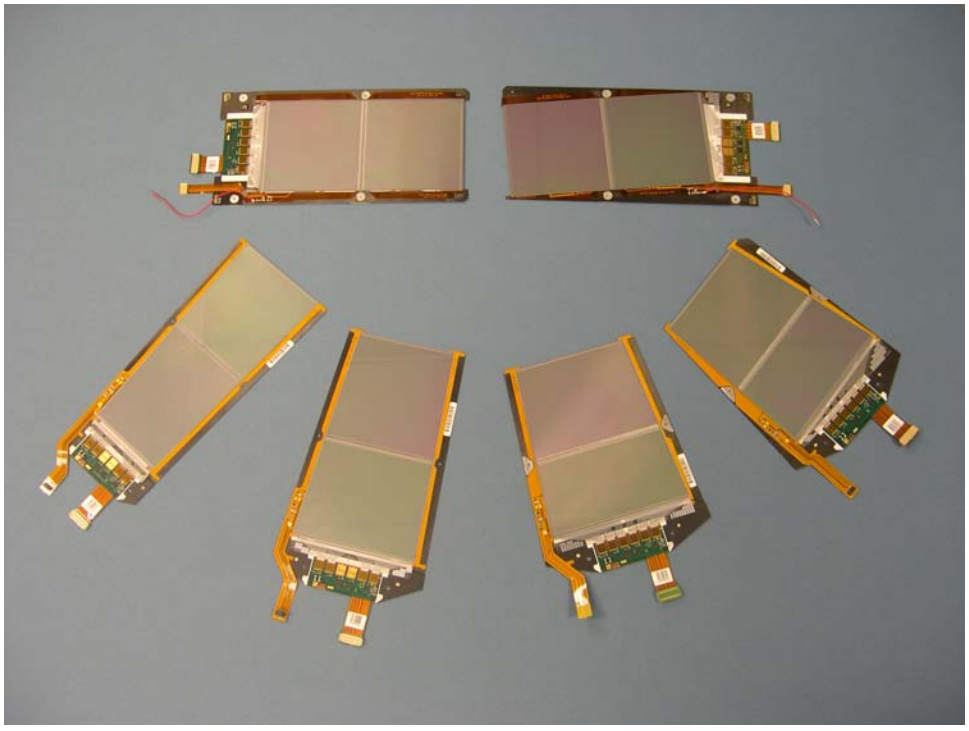

Figure 3-12. Examples of tracker strip modules from the outer barrel and end-caps (Copyright CERN [43]).

The inter-strip distance (strip pitch) of TIB varies from 80-120μm. Despite having sensors roughly 100 times as large as the pixels, due to its increased distance from the interaction region, TIB is able to maintain no more than about 3% occupancy per bunch crossing (at LHC design luminosity) and boasts a positional resolution only slightly worse than the pixels, at 23-34 μm in $r-\phi$ and 23 μm in z.

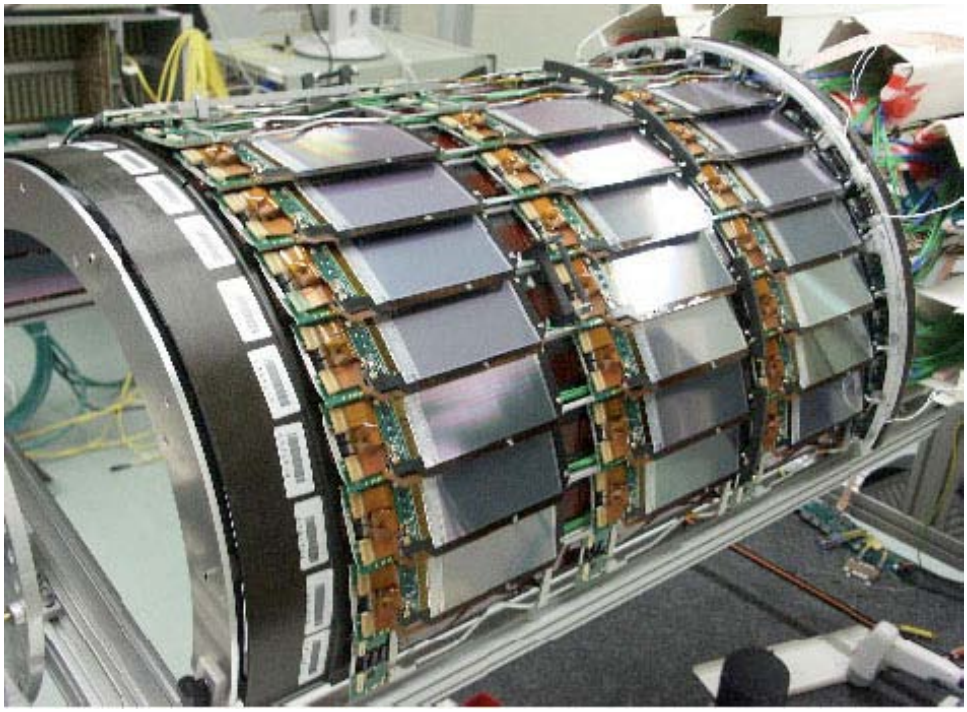

Figure 3-13. A photograph of a mock-up of a layer of the tracker inner barrel (Copyright CERN [43]).

Tracker Outer Barrel. The six layers of TOB sit between a radius of 55 cm and 120 cm, with their furthest extent to $z = \pm 110$ cm. As with the inner barrel, the first two layers of TOB provide a stereo measurement. The cell size of an individual detector element is 25 cm by 180 μm; however despite it's large size, at this distance from the interaction point, sensor occupancy is sub-percent. Positional resolution in the outer barrel is approximately 35-52 μm in r-ϕ and 52 μm in z.

Tracker End-Cap. TEC consists of nine disks, arranged along the z axis between 120 cm and 280 cm. Each cell in the end-cap is up to 20 cm in length with a strip pitch of up to 200 μm. Each TEC disk has sixteen petals of sensor elements (eight on each

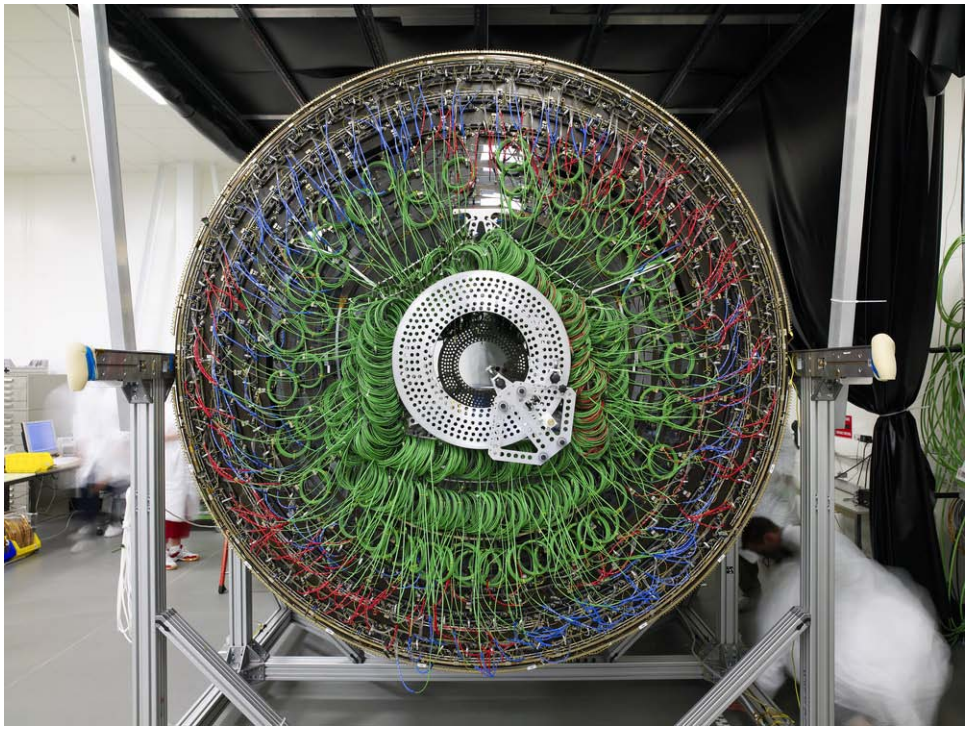

Figure 3-14. A photograph of the tracker outer barrel ready for insertion into CMS (Copyright CERN [43]).

side), as shown in Figure 3-15, which are distributed into seven distinct rings (defined by a range of radii).

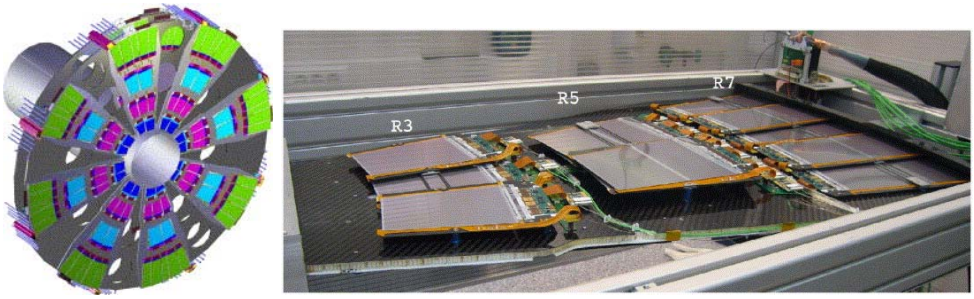

Figure 3-15. Left: illustration of two TEC disks (in series); each is equipped with eight "petals" per side. Right: photograph of a test bench assembly with three rings of petals (Copyright CERN).

3.4 Calorimetry

Beyond the silicon tracker, though still within the solenoid, are separate electromagnetic and hadronic calorimeter sub-detectors. Because these systems are completely

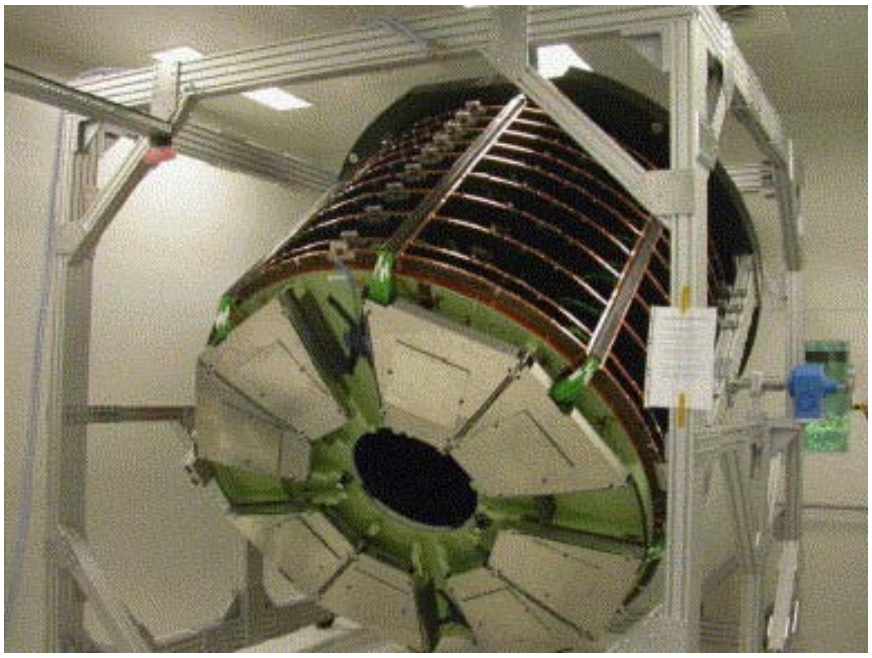

Figure 3-16. A photograph of one of the two tracker end-caps (TEC), installed in a rotating cradle (Copyright CERN).

contained within the solenoid, they must be extremely resistent to magnetic fields – a non-trivial requirement, particularly for electronics.

Unlike the tracker system which is designed to be light-weight, the calorimeters are as dense as possible in order to absorb the maximum amount of energy; this, of course, also implies that they must have a great deal of radiation hardness. Although there are far fewer channels in the calorimeters than in the inner tracker, calorimeter technology must have a very quick response in order to keep up with the LHC collision rate.

3.4.1 Electromagnetic Calorimeter

The electromagnetic calorimeter (ECAL) [47] consists of two technologies: crystal scintillators in the barrel region and both crystals and a complementary silicon strip preshower system in the end-cap. In total, the sub-detector contains nearly 90 tons of scintillating lead tungstate ($PbWO_4$) crystal (approximately 80,000 individual crystals).

ECAL provides excellent energy resolution for electrons and photons of $\sigma/E = 3\%/\sqrt{E} \oplus 0.3\%$ (typical), and granularities of around 2 cm. Each crystal used in

CMS is 23 cm long; crystals in the barrel region have a cross-sectional footprint of 2.05 cm$\times$2.05 cm, while those in the endcap range in size from about 1.8 cm$\times$2.0 cm to 2.7 cm$\times$2.9 cm. The layout of the detector is indicated in Figure 3-17.

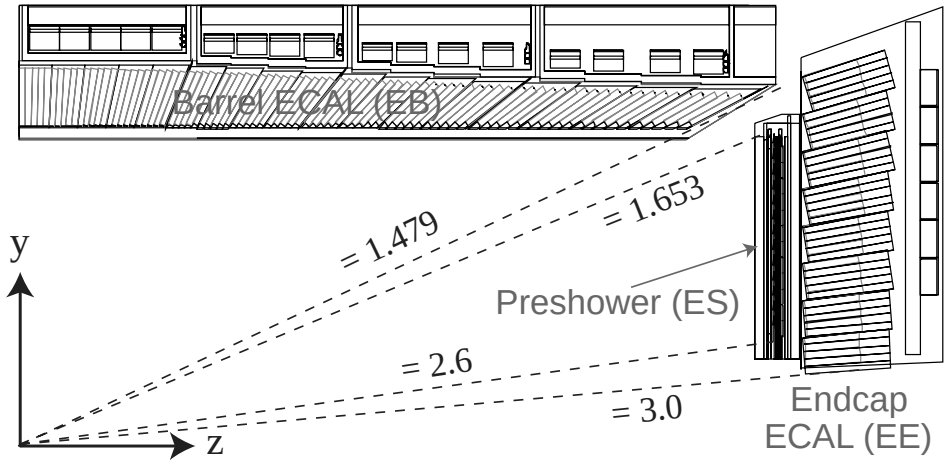

Figure 3-17. Quarter view of ECAL layout.

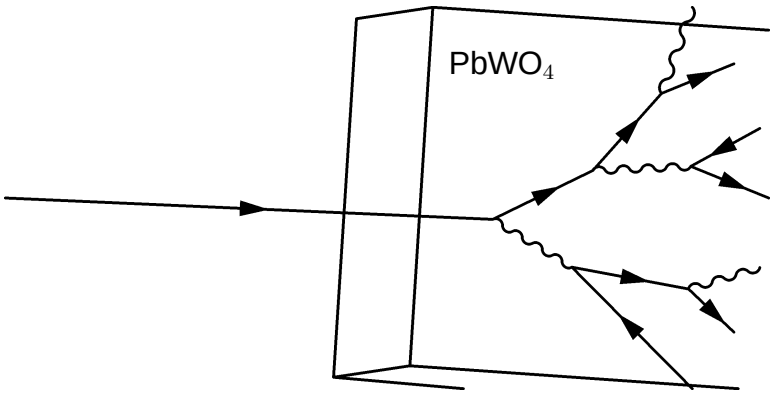

Figure 3-18. With sufficient energy and in the presence of a high-*Z* medium (such as lead tungstate), ionizing particles (such as electrons) will readily radiate photons; while photons will decay to e^+/e^- pairs. *Drawing not to scale*.

Detector technology. When photons or charged particles pass through high-Z materials, an electromagnetic shower may develop from Coloumb interactions, inducing the radiation of photons and e^+-e^- pairs (which in turn also shower). This process repeats until the energy of each produced particle falls below the threshold for new pair-production; at which point, the remaining soft electrons and photons are absorbed

by the crystal. As the crystal absorbs energy, it emits light which is then collected by photodetectors on the back of the crystal. The total amount of light measured in the photodetectors is then proportional to the energy of the incident particles.

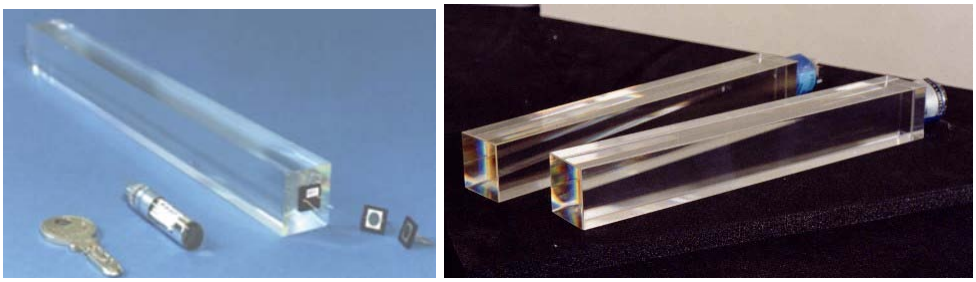

Figure 3-19. Left: photo of a single ECAL crystal with sensors (next to a house key for scale). Right: photo of ECAL crystals with sensors installed (Copyright CERN).

Lead tungstate crystals have a short radiation length, $X_0 = 0.89$ cm, so that even highly energetic showers will be stopped within their length; and a Moliere radius (indicating the characteristic *spread* of an electromagnetic shower in the material) of just 2.2 cm, which is helpful to localize the likely entry point of the particles.

The material is a fast scintillator; emitting approximately 85% of its light yield within the first 20 ns of a particle traversing it. Although the total light yield of the crystals will decrease as it is exposed to radiation from LHC collisions; the photodetectors are sensitive enough to allow recalibration, and resolutions are not expected to suffer because of it.

ECAL Barrel. Within EB, there are 61,200 individual ECAL crystals arranged by 5 $\times$ 5 arrays into 144 modules. Four modules make up a unit called a supermodule; there are a total of 36 supermodules in ECAL – each one providing 20° of coverage over one half of the barrel. A schematic of the EB sub-detector is given in Figure 3-20.

Photographs of a single EB module, a supermodule, and an entire half-barrel assembly are shown in Figures 3-21 and 3-22.

ECAL End-cap. Instead of modules and supermodules, the two ECAL end-caps are constructed from four “dee” (half-moon) structures; two per side. Each dee contains

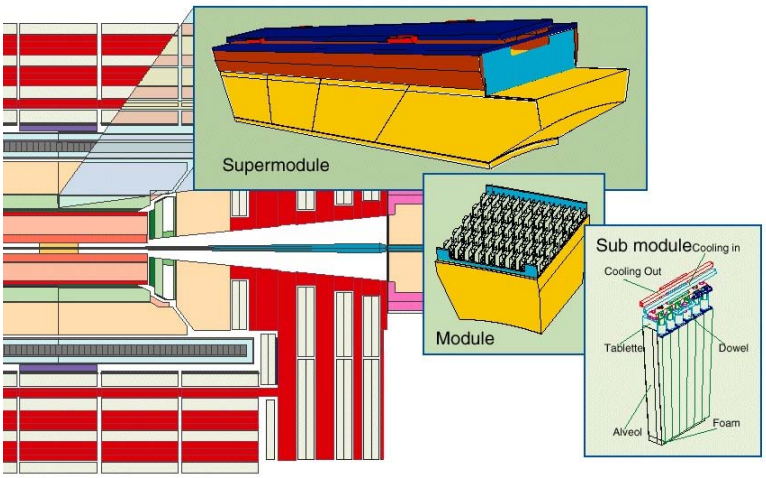

Figure 3-20. Design of ECAL Barrel (EB)

Figure 3-21. Photo of a partially completed EB module on a test bench (Copyright CERN).

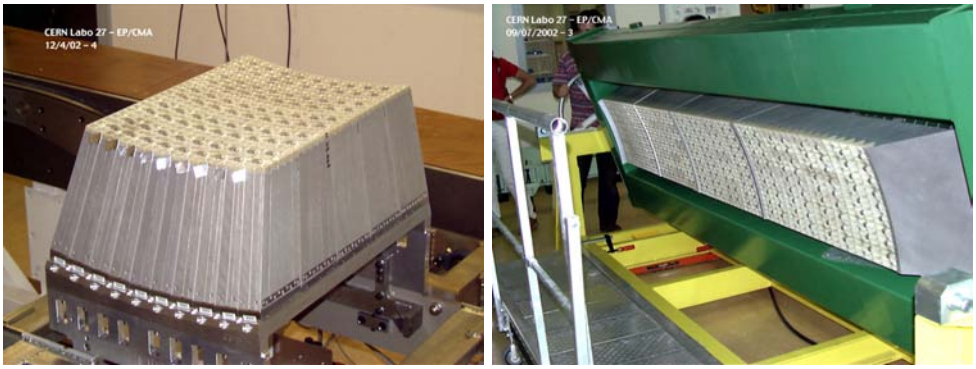

Figure 3-22. Left: photo of a single EB module on a test bench. Right: several modules combined to form a supermodule mounted onto a rotating cradle (Copyright CERN).

138 5×5 supercrystals, for a total of 3450 crystals per dee and 14,950 for all of EE. The layout of EE is indicated in Figure 3-23. A dee, with several EE supercrystals installed, is shown in Figure 3-24.

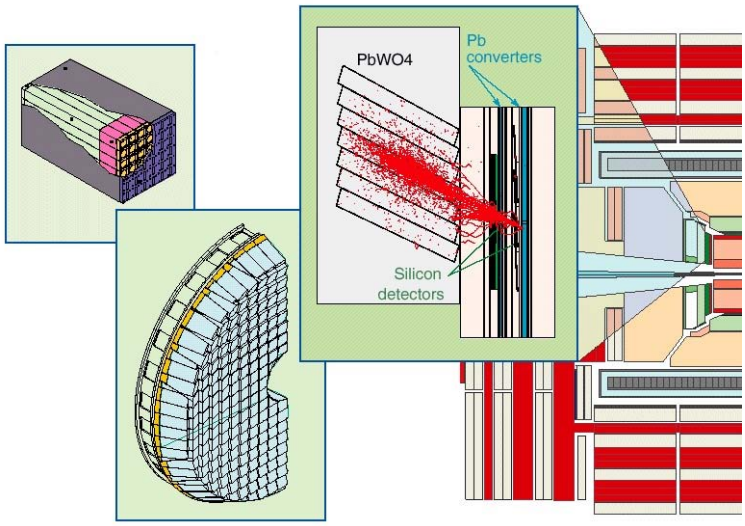

Figure 3-23. Design of ECAL End-cap (EE)

Pre-Shower Detector. In order to improve distinguishability between neutral pions from photons, a pre-shower detector is installed in front of the endcap crystals. The pre-shower detector contains two layers of lead converters and silicon strip detectors. Since π^0 mesons decay to di-γ, π^0's may be distinguished from prompt photons by broader charge distributions on the strips.

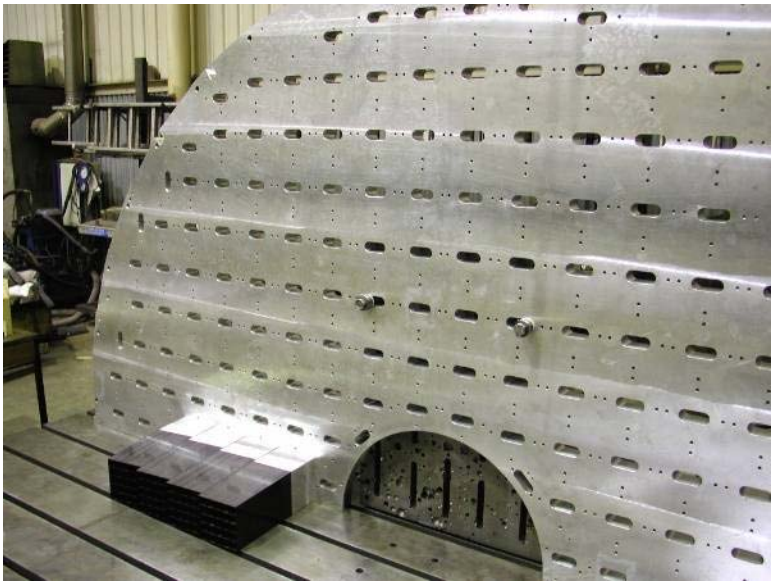

Figure 3-24. Four ECAL End-cap (EE) supercrystals mounted on a “dee.” Each dee has 138 such supercrystals (Copyright CERN).

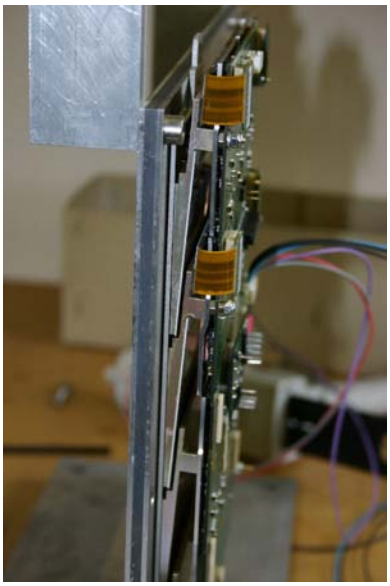

Figure 3-25. Photograph of an ECAL preshower module on a test bench (Copyright CERN).

3.4.2 Hadronic Calorimeter

The hadronic calorimeter (HCAL) [48] consists of a a conventional sampling-type calorimeter throughout the barrel (HB) and forward end-cap (HE) regions, and a quartz fiber sub-detector unit in the *very* forward region (HF). It is designed to be as *hermetic* as possible – that is, having the largest possible coverage. Having a hermetic calorimeter allows for the indirect observation of undetectable particles such as neutrinos (by balancing the total amount of transverse energy measured in the products of a collision).

The calorimeter uses thick steel and brass absorbers interleaved with plastic scintillator tiles. Particles passing through the absorption layers may interact with the heavy nuclei of the dense materials and will shower; the resulting spray of particles passing through the scintillator layers cause them to emit ultra-violet light. This light produced in the scintillators is converted to visible light by 1 mm diameter wavelength-shifting fibers and carried to hybrid photodiodes to provide read-out. A "hybrid" photodiode is a photocathode held at high voltage (-8 kV) a short distance (3.3 mm) away from a silicon photodiode; the high voltage accelerates photoelectrons produced by the scintillator light and results in a total signal gain of approximately 2000.

Brass[3] was chosen as the main absorber material for HCAL because it provides sufficient density (8.53 g/cm^3, yielding an interaction length of 16.42 cm) while having excellent machinability.

HCAL Barrel. HB consists of brass absorber (either 5.05 cm or 5.65 cm thick), and front and back plates of steel, 4.0 cm and 7.5 cm thick respectively, which provide additional rigidity and strength. Fourteen of the scintillator layers are 3.7 mm thick, however the inner and outer layers are 9 mm (16 layers total). It is constructed from

[3] Specifically, 70%Cu, 30%Zn C26000/cartridge brass – much of it melted down from artillery shells contributed by the Russian Navy.

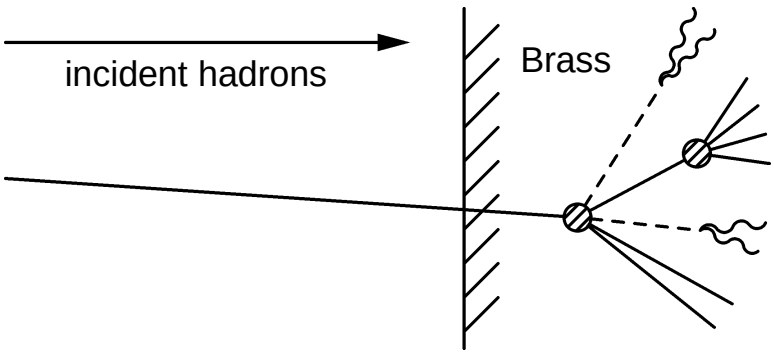

Figure 3-26. When highly energetic hadrons scatter off of nuclei in matter, the collision produces a spray of particles – including more hadrons – such as neutral pions (dashed lines); charged pions or kaons (solid lines), which may collide with more nuclei, creating a cascade effect. As it develops, the resulting shower will produce light within the scintillator tiles proportional to the number of particles in the cascade, which is in turn proportional to the energy of the original hadron.

36 wedges forming two half-barrels; each wedge is bolted together, leaving a gap of at most 2 mm between adjacent wedges. The scintillators are read out in 16 η regions. The granularity of HCAL is square in the barrel region in η and ϕ, with $\Delta\eta \times \Delta\phi$ = 0.087 $\times$ 0.087. It provides coverage up to $|\eta|$ = 1.3.

Figure 3-27. Left: a series of HB wedges awaiting assembly. Right: merged together to form the HB sub-detector (Copyright CERN).

HCAL Endcap. The HE sub-detector contains 7.9 cm thick brass absorber and 9 mm scintillator tiles. The layers are affixed to a 10 cm thick support plate, which is mounted to the iron return yoke. Granularity in HE varies from $\Delta\eta$ = 0.087 to 0.35 and

$\Delta\phi$ from 0.087 to 0.175 radians, and the sub-detector provides coverage from $|\eta|$ = 1.3 to $|\eta|$ = 3.

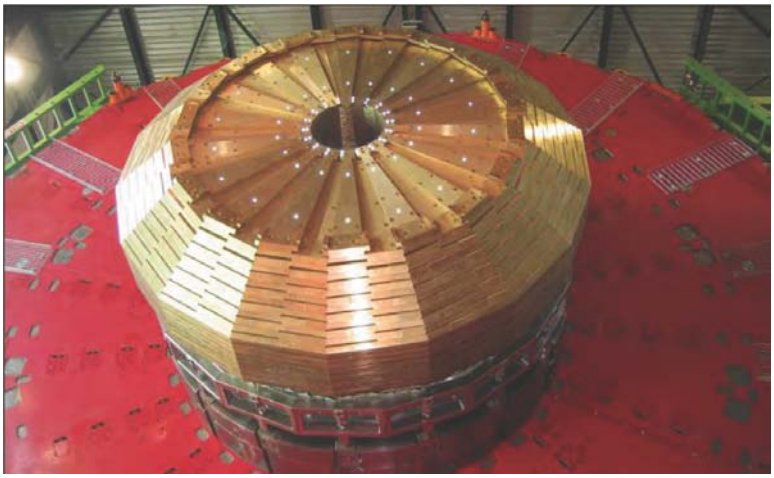

Figure 3-28. Photograph of the HCAL End-Cap (Copyright CERN).

Outer Hadronic Calorimeter. The outer hadronic calorimeter (HO) is a sampling calorimeter placed outside of the solenoid which acts as a "tail-catcher" for extremely high energy jets; that is, for particles which could not be completely absorbed within the bulk of the inner system. Rather than a half-barrel design like the inner calorimeters, HO is mounted to the rings of the iron return yoke; it is therefore separated into five sections (one for each of the five wheels of CMS). It consists of a single scintillator layer at r = 4.07 m mounted on top of a 19.5 cm iron absorber for the full η range, and an additional scintillator layer mounted on the underside of the iron in the very central region. Because it is meant as a complementary detector to HB, its granularity and η and ϕ parameters are matched to those of HB.

Forward Calorimeter. HF provides coverage up to an η = 5.0, with a granularity of $\Delta\eta \times \Delta\phi$ = 0.175 $\times$ 0.175. Because of the extreme radiation levels near the beam line and in the forward region, traditional shower sampling calorimeters are not suitable; a Cherenkov light counting calorimeter is used instead. In this sub-detector, iron is used as an absorber material; when charged particles interact with the iron, they will begin showering (either electromagnetically or hadronically). The resulting shower will

radiate photons as they pass through the quartz fibers (since quartz has a high index of refraction, charged particles will emit Cherenkov light as they pass through the fibers if they are traveling faster than the local speed of light) which are arranged parallel to the z-axis. The threshold for Cherenkov emission in quartz is only 190 keV for electrons.

Because electromagnetic showers develop much more quickly than hadronic showers, it is possible to distinguish incident electromagnetic particles from hadronic particles by having fibers of different lengths in HF. Two fiber lengths were chosen for HF, called “long” and “short”, which are 1.65 m and 1.43 m in length, respectively; with the shorter fiber being displaced away from the interaction region. The ratio of measured energy in the two lengths of fibers (long to short) gives a good indication of whether the shower is hadronic or electromagnetic; as an electromagnetic shower will leave much more energy in the long fiber than in the short fiber.

Figure 3-29. Photograph of wedges of the Forward Calorimeter (HF) awaiting installation (Copyright CERN [43]).

3.5 Muon Spectrometers

Good muon resolution is a key design goal of the CMS detector; as muons are a feature of many theoretical models which will be studied at CMS (such as Supersymmetry, Universal Extra Dimensions, etc.). For this analysis, the muon spectrometer

systems [49] of CMS are used to provide triggering capabilities, as well as tracking, to supplement the inner silicon detectors. The muon systems are divided up into a series of five wheels in the barrel region and two end-caps, as may be seen in Figure 3-30.

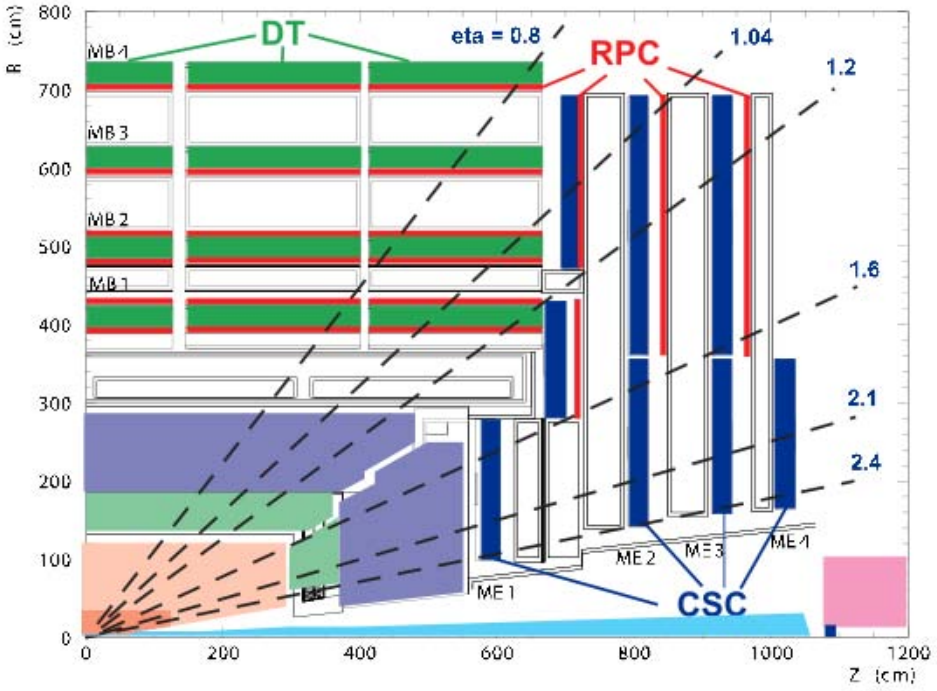

Figure 3-30. Quarter view showing the muon system.

The muon sub-detector consists of three separate technologies: Resistive Plates (RPC), Drift Tube (DT), and Cathode Strips (CSC). Drift tubes provide an inexpensive solution which works well with low occupancies and in uniform magnetic fields; so they are used in the barrel region. The cathode strip chambers function well even in rapidly changing magnetic fields and with higher particle fluxes; hence they are installed in the end-caps. Resistive plate chambers are a simpler technology used in both the forward (RPCf) and barrel (RPCb) regions, and provides a complementary system for timing and triggering purposes. The chambers are installed in four separate stations, or layers of chambers; one station on each of the five wheels of CMS in the barrel region and four stations deep in the end-caps. Each of the stations is mounted to the iron yokes. The

combined resolution for muons, including both the muon spectrometers and the inner tracker, is indicated in Figure 3-31.

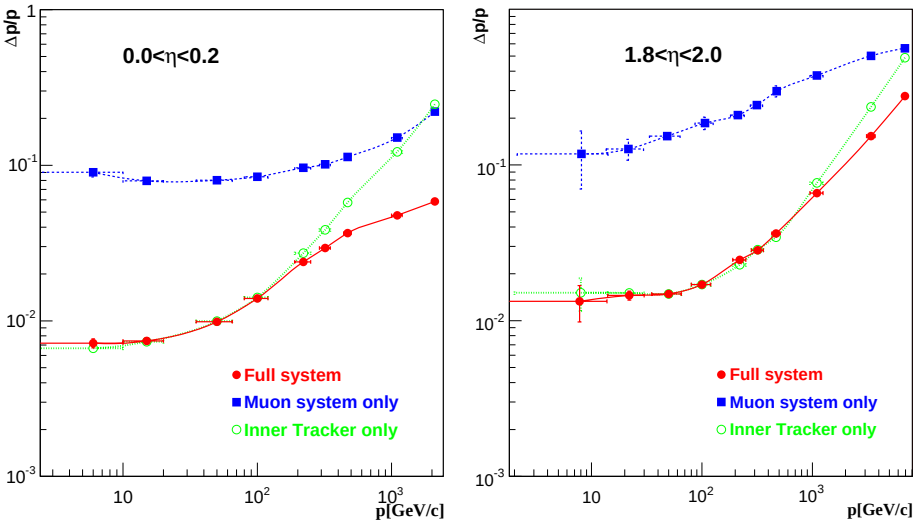

Figure 3-31. Muon momentum resolution, including both the inner tracker and the muon spectrometers. Left: the barrel region. Right: the end-cap regions [61]. This result is for design usage of the CMS detector (that is, muons produced in collisions). The situation isn't as simple for cosmic muons, where the resolution has complex dependencies on the location and angles of particle incidence.

3.5.1 Drift Tube Chambers

The drift tube chambers are constructed from aluminum cathode tube (1.3 cm$\times$4.2 cm) with a central gold-plated, 50 μm stainless steel anode wire, and filled with Ar/CO_2 gas in a 85-15 mixture. There are either two or three "super-layers" (SL) in a DT chamber; two provide $r-\phi$ measurements and a third one, present only for the inner three stations, provides a measure of particle z. A single SL is made up of four layers (consisting of a wire and a tube). In total, there are therefore either 8 or 12 detection layers in a single DT chamber. Because the DT adopted an essentially frameless design, rigidity and structure is provided by an aluminum honeycomb layer in the center of the chamber. There are a total of 250 DT chambers installed at CMS, divided up into the 5 wheels and 12 ϕ sectors.

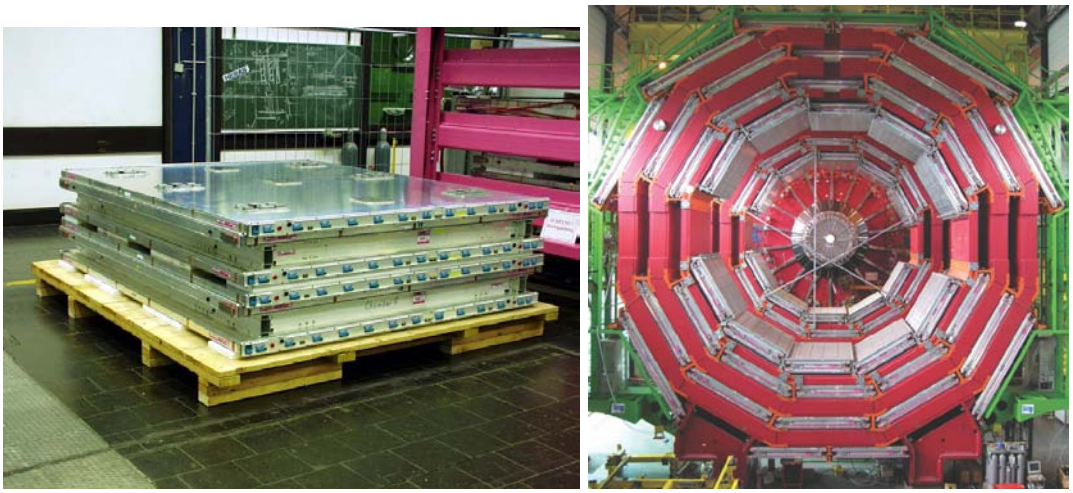

Figure 3-32. Left: photo of Drift Tube (DT) chambers awaiting shipment to CERN. Right: as installed in the barrel region (Copyright CERN).

When charged particles (typically muons, since most other particles will be trapped within the calorimeters) pass through the gas, they will knock electrons free from the gas. A high voltage between the wire and the tube will cause an electron avalanche; as the electron will free additional electrons on its path towards the anode wire. The resulting charge build-up on the wire can be read-out to provide a signal for the chamber. Typical spatial resolution for the DT system is 250 μm (as low as 100 μm in $r - \phi$), with a timing resolution of 5 ns – which is well measurable because the drift velocity for electrons in Ar/CO_2 is known precisely (5.4 cm/μs at 1.8 kV; for a maximum drift time of 380 ns).

3.5.2 Resistive Plate Chambers

The RPC chamber are a “double-gap” resistive plate technology which provides ultra-fast (1 ns, much less than the 25 ns collision frequency) timing information. Anode strips (running parallel to the beam) separate the two gaps and provide a common readout. There are a total of 480 RPC chambers; divided up into six layers in the barrel region (which are distributed amongst the four muon stations) and three layers in the end-cap region. The RPC chambers, though less accurate than the DT chambers,

provide an invaluable source of information regarding the overall muon triggering performance of CMS.

3.5.3 Cathode Strip Chambers

The CSC's are multi-wire proportional chambers consisting of seven cathode layers, milled to have a constant $\Delta\phi$ along the length of the trapezoidal chamber, interleaved with six gold-plated tungsten anode wire layers. The chambers are filled with $Ar/CO_2/CF_4$ gas in a 40-50-10 mixture. There are a total of 468 chambers distributed between the two end-caps, with an additional 72 chambers planned for a future upgrade. Each station provides either 10° or 20° of coverage in ϕ and the entire system covers $0.9 < |\eta| < 1.2$. Spatial resolutions of 100-200 μm are possible in the CSC's. As in the DT chambers, charged particles traversing the CSC's will ionize the gas and free electrons, which avalanche in the presence of a high electric field towards the anode wires. The charges collected on the anode wires induce a reflected image charge on the strips, which can be integrated in order to find the centroid (most likely position of the particle position) for an accurate measure of the ϕ position of the particle; while the differential signal obtained from the anode wires yield a fast response for timing purposes as well as a measure of the muon η.

Commissioning with Cosmics. Although the CSC detectors are not suitable for use in this measurement (incident cosmic muons are primarily vertical, and therefore parallel to their active detection surfaces – leading to unpredictable behavior and poor efficiencies), they have been partially commissioned on cosmic muons before. In 2004, several CSC chambers were used in a cosmic muon test at the University of Florida. A test stand was constructed, and CMS-like triggering logic was simulated.[4] With the

[4] The author contributed to both efforts; machining the necessary steel extender arms for the stand, helping to install and cable the scintillator panels used to provide the triggering signal, and also designing and assembling the NIM crate used to provide triggering logic.

absence of beam, cosmic muons provided a useful source of tracks for testing and calibrating the chambers. The test stand is illustrated in Figure 3-34.

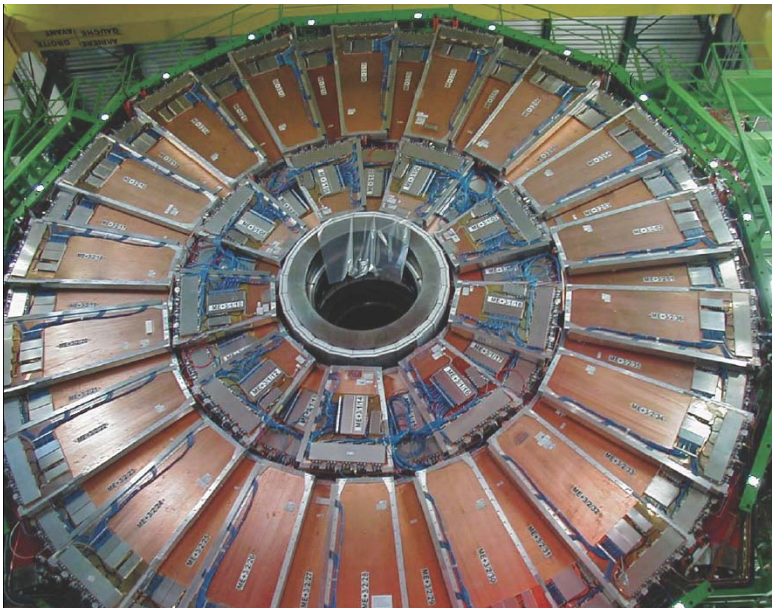

Figure 3-33. Photograph of a disk in the end-cap muon system (Copyright CERN).

Figure 3-34. This cosmic test stand was constructed at the University of Florida in support of CSC commissioning.

CHAPTER 4
CHARGE RATIO ANALYSES

The cosmic muon charge ratio is a measure of the relative number of positive and negative muons present within the cosmic muon spectrum. Because few machines exist that can provide precision measurements of the momenta of individual charged muons in the GeV to TeV energy range,[1] the measure of this quantity remains an area of some interest in the ranges of energies to which CMS, with its large size and powerful magnetic field, has the capability to access. Three separate analyses were performed to measure the charge ratio at CMS – though just one is described in detail in this dissertation (the one introduced in Section 4.2.2). In this chapter, all three analyses are briefly introduced.

4.1 The MTCC Analysis

The first analysis [50, 51] was performed on data collected from the "Magnet Test and Cosmic Challenge" (MTCC) exercise [52–54], conducted as part of commissioning on the pre-assembled detector at the end of 2006, while it still sat on the surface of the earth. Around 15 M events were recorded during MTCC in runs with a stable magnetic field of at least 3.67 T.

During pre-assembly, only a small fraction of the detector was instrumented; as such, only the bottom sectors of two out of the five wheels of DT chambers were available for track reconstruction, as illustrated in Figure 4-1 (bottom). Even with the limited detector area, the probability of charge misassignment is small for low-momentum muons. At higher momenta, resolution effects increase the chance of random charge misassignment; resulting in an artificially low value for the charge

[1] The two commonly studied regimes are for muons with a low enough energy to be curved in small or weak magnetic fields; and extremely energetic muons, which can be measured using calorimetry.

ratio.[2] To demonstrate this effect, the parameterized charge ratio (Equation 1–3) has been plotted along with various assumptions on the rate of charge mis-assignment at 200 GeV/c in Figure 4-2, assuming a simple, linearly increasing probability for mis-assignment.

Up to 200 GeV/c, the rate of charge mis-assignment is low enough to be safely estimated and corrected for using Monte Carlo simulations. Only muons reconstructed within a symmetrical fiducial volume were accepted for analysis. Approximately 330 k out of the original 15 M cosmic muon events remain after all selection requirements have been applied.

4.2 The CRAFT Analyses

Two analyses were conducted on data from "Cosmic Run at Four Tesla" (CRAFT) exercise [55], collected between October 17th and November 11th, 2008. During CRAFT, the entire machine was instrumented and installed underground. One of the analyses used only muon system hits for tracking, while the other analysis used both muon system and tracker hits. The kinds of tracks used in both analyses are illustrated in Figure 4-1.

Cosmic muon events were collected on an open[3] muon trigger [56] path, with triggers originating in either of the barrel sub-detectors (DT or the barrel RPC). Approximately 270 M cosmic muon events were recorded on these triggers. For both analyses, a symmetric selection is applied with respect to the *yz*-plane; removing muons from consideration if they have a trajectory through the two asymmetric auxiliary access shafts at

[2] Since the charge ratio is greater than one, there are more positively charged muons that can be mis-reconstructed with a negative charge than there are negatively charged muons that can be mis-reconstructed as having a positive charge.

[3] That is, no momentum requirement.

Point-5, or through the mirror image of those shafts. No selection is applied to the main access shaft (which is symmetric in the *yz*-plane).

4.2.1 Analysis with Stand-Alone Muons

In this analysis [57], muon trajectories are reconstructed using only hits from the DT and RPC barrel sub-detectors. Tracks with any hits in the endcap CSC chambers are rejected, and hits in the silicon tracker are used only to estimate momentum resolution and systematic uncertainties. Single leg reconstruction is used, such that hits in both the upper and lower halves of CMS are merged into a single track object; allowing for a longer lever arm in the magnetic field, and therefore improved momentum resolution. In order to suppress the background from multi-muon events, exactly one single-leg track is required in each event.

A minimum transverse momentum of 10 GeV/*c* is required; and a minimum of 45 hits in the Drift Tubes are required, with no less than 20 hits each in either the top or the bottom of the detector. Further selections are applied on the track χ^2, the impact parameter in the *xy*-plane (less than 100 cm, such that the silicon tracker may be used to estimate muon system detector performance), the maximum distance (at the point of closest approach) from the center of the detector along the *z*-axis (less than 600 cm) and the angular trajectories (vertical within 42° in θ and 60° in ϕ). Approximately 1.6 M cosmic muons out of the original 270 M CRAFT events are selected.

4.2.2 Analysis with Global Muons

This analysis [58–60], based on "global" muons, is the primary focus of this dissertation. The trajectory for a global muon is reconstructed using both DT and TOB hits. In particular, for this analysis, each cosmic muon is required to be reconstructed as two separate track segments – one above and one below the point of closest approach – each having unshared hits in both DT and TOB. Each of the two track segments must have at least five hits in TOB and at least 20 hits in the DT system; of which, at least three must provide a measurement of the *z* coordinate (so as to obtain an accurate

measurement of the zenith angle). The analysis is restricted to the barrel region of CMS; therefore, the muon track may contain no hits in either the muon or tracker endcaps. A loose requirement is applied to the normalized χ^2 of each of the two global-muon fits. In order to eliminate the small background due to multi-muon shower events; exactly two track halves must be in the event, and the zenith angle between them is required to match within $|\Delta \cot \theta| < 0.2$. Finally, the average transverse momentum of the two track halves is required to be greater than 10 GeV/*c*. Out of 270 M, approximately 245 k muons pass the selection requirements.

4.3 Summary

For the final measurement of the cosmic muon charge ratio, the results of all three analyses are combined. The MTCC data (since it was collected on the surface) provides a good result for the lowest energies; which are difficult to obtain in the later data due to shielding by the earth. For higher momenta, the two CRAFT analyses provide complementary results. The results of all three analyses are combined in Chapter 7.

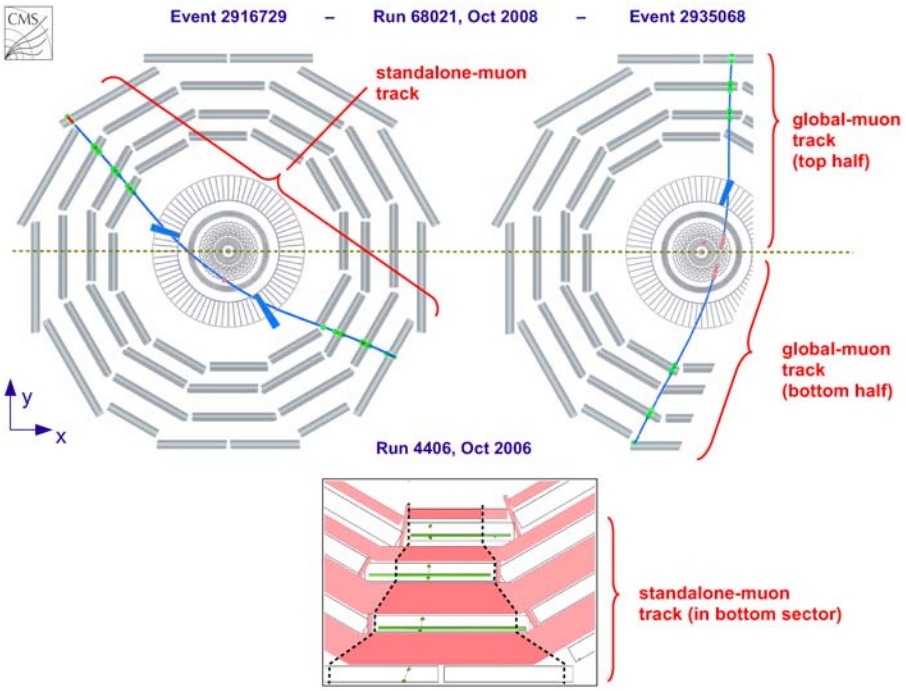

Figure 4-1. Types of tracks used in each of the three analyses. Upper left: the stand-alone muon analysis utilizes hits from both halves of the muon system. Upper right: the global muon analysis requires hits in both the silicon tracker and the muon system. Bottom: the MTCC had only a single sector of two wheels in the bottom of the detector to use for tracking.

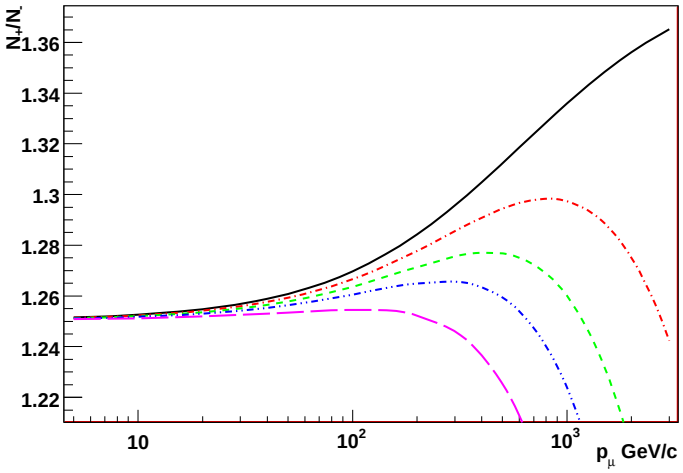

Figure 4-2. The effect of mis-assignment on the charge ratio. A mis-assignment rate of 1%, 2%, 3%, and 5% at muon momenta of 200 GeV/c is shown, increasing linearly with momentum. The detector performance in Monte Carlo is used to estimate the actual form and magnitude of charge mis-assignment.

CHAPTER 5
THE GLOBAL MUON ANALYSIS

This chapter provides a description of the analysis performed using global muon tracks collected during CRAFT. The final results of all three analyses are ultimately combined to form the official CMS measurement of the cosmic muon charge ratio.

5.1 Analysis Overview

The analysis is performed by first applying selection requirements on the muons observed within the detector to ensure good track objects. The collection of objects – split at the point of closest approach (PCA) to the z-axis – are individually propagated to the surface of the earth in order to estimate the energy losses through the earth and detector material. An unfolding procedure is used, which consists of approximating the migration matrix – which acts to convert a true count of muons at the earth surface to a measured count within CMS – and inverting it, in order to derive a final count of positive and negative muons in each bin after accounting for all resolution effects. Unfolding is handled separately for two cases: muon counts binned by their momentum (p) and the vertical component of their momentum ($p\cos\theta_z$), always as estimated at the surface of the earth.

5.2 Selection Requirements

5.2.1 Event Selection

Approximately 270 million cosmic muon events were collected over the duration of CRAFT. This analysis is based on a subset of that data; in particular, events were skimmed for "tracker pointing" muon tracks: tracks reconstructed in the outer muon chamber which propagate into a 260 cm long, 90 cm diameter cylinder at the heart of CMS. This propagation cylinder sits well within the volume of the silicon tracker. Events were required to have been collected during runs with a stable 3.8 T magnetic field.

Trigger. An "open" trigger path was used at hardware level, which promotes any valid muon trigger candidates (because the trigger estimates momentum using

look-up tables designed for the LHC, momentum-based triggering is not possible with cosmics). Because this analysis is based on barrel muon events, the triggered sample was further required to have at least one trigger candidate from either the DT or RPCb sub-detectors.

The muon trigger system at CMS reports an η and ϕ coordinate as measured at a particular trigger surface, nominally located at the center of a chamber in station two [61]. For LHC conditions, this data is intended to represent the η and ϕ of the momentum vector as it passes through the chambers; however for cosmic muons (since they are coming from above, and not constrained to pass through the geometric center of the detector), this coordinate represents a point in space which is the intersection of the η and ϕ vector (in CMS detector coordinates) and the surface representing the center of station two, which is approximated as a cylinder with a radius of 5 m.

To determine whether a muon trigger candidate can be matched to a track for analysis, the stand-alone muon track (the portion of the global muon track consisting only of Muon Spectrometer data) is propagated to the center of station two of the DT system. Matching requires that $\mid \Delta\phi \mid < 0.2$ between the recorded position of the trigger and the position of the propagated stand-alone muon at station two. The shape of the $\Delta\phi$ distribution at a radius of 5 m is displayed in Figure 5-1 for different halves (top and bottom) of the detector, and also for positive and negative muons.

5.2.2 Physics Object Selection

As described in Section 5.2.1, the presence of a reconstructed track in the muon spectrometer entering the tracker volume is assumed. Global muons are reconstructed [62, 63] from the combined hits in the silicon tracker and muon spectrometers; and only tracks consisting of both kinds of hits are utilized in the analysis. In particular, split tracks are used; meaning that the hit data is divided up into separate top and bottom track halves (each of which are also global muon tracks).

Only muons in the barrel region of CMS are considered; therefore, any tracks containing hits in the Tracker Endcaps or Cathode Strip Chambers are removed. Muons must have a transverse momentum of at least 10 GeV, and be traveling downward along the detector-y (approximately pointing down, into the earth); such that the ϕ of their momentum vector is negative at the PCA.[1]

Splitting. In Section 5.4, the methodology for obtaining a data-driven estimate for detector resolution is described. As part of this methodology, the track must be fully splittable within the silicon tracker; in other words, there must be at least one hit in the silicon both above *and* below the PCA, in order to construct separate upper and lower tracks with *unshared* tracker hits.[2] The split requirement is most efficient for tracks passing close to the geometric center of CMS (and thereby passing through a maximum amount of tracker material), with efficiency rapidly dropping for distances larger than about 50 cm, as may be inferred from Figure 5-2. The components of the PCA are the cosmic muon analogs of the *impact parameters* traditionally used in collider physics. Thus, in Figure 5-2 the traditional notation for impact parameters is used; d_0 refers to the shortest distance between the trajectory of the particle and the z-axis/beam-line, and z_0 refers to the displacement of that point from the center of the detector along the z-axis.

5.2.3 Quality Selection

Each of the selection quality requirements are applied individually to the top and bottom legs of the reconstructed tracks. A minimum of 20 hits in the DT chambers were required. At least three of the DT hits must be in Superlayer-2, which measures the

[1] Although cosmic muon reconstruction is seeded assuming downward momentum, occassionally non-downward trajectories result, most typically because the muon has low momentum and is actually turned around by the magnetic field of CMS, or has been "back-scattered" off of material below. More exotic explanations are also possible, but exceedingly unlikely [64].

[2] Standard split tracks in CMS cosmic muon reconstruction do not require the legs to have unshared silicon hits, thus this is a more strict selection requirement.

z-component of the local trajectory; which is necessary in order to obtain a satisfactory measurement of the track θ. While two TOB hits are implied by the split track requirement, additional hits are effective at reducing charge confusion. Sufficient suppression of charge confusion is observed with five or more hits in the TOB (with diminishing returns – coupled with a rapid loss of efficiency – if more than five hits are required). An extremely loose requirement on the χ^2 (1500) is applied to track fits, in order to reject poorly reconstructed tracks. This requirement was found to efficiently remove events in which the global muon fit would incorrectly flip the charge of the muon.[3] Figure 5-7 shows the efficiency of the χ^2 requirement as a function of p_T; it is nearly 99% for all momenta considered in this analysis.

With split tracks, it is necessary to verify that the two track halves are indeed consistent with the same muon. This necessitates, first of all, that multi-muon events (with their unavoidable ambiguities) are suppressed, by requiring exactly two split tracks in the event; one in the top and one in the bottom of the detector. Even after the removal of obvious multi-muons, it is occassionally the case that two unrelated tracks may be incorrectly be associated with one another; so additional matching is required. A logical variable is the difference in the ϕ of their trajectories at the PCA; however this is highly sensitive to the estimates of the particle charge, and would hence bias the estimation of detector resolution. In fact, the only way to avoid biasing this measurement is to restrict the matching to trajectory along the *z*-axis; because the magnetic field in the barrel region is highly uniform and parallel to *z*, and thus the detector does not use this information to estimate the momentum or charge of the incident muon track. In particular, a selection requirement on the cotangent of the track θ (angle of trajectory in the *rz*-plane) is used.

[3] This was originally necessary due to a bug in the reconstruction algorithm, since corrected.

The correlation between the estimator of the curvature resolution (d_C, described in Section 5.4) is shown for two potential matching requirements, $\Delta\phi$ and $\Delta\cot(\theta)$, in Figure 5-8. While a strong correlation with $\Delta\phi$ is observed (as expected), the correlation with $\Delta\cot(\theta)$ is found to be a negligible 0.7%. Therefore, no requirement on $\Delta\phi$ is used and only a loose requirement of less than 0.2 is applied on $\Delta\cot(\theta)$ in order to suppress mismatches between the top and bottom legs. The performance distributions for transverse curvature and charge confusion against this variable are shown in Figure 5-3.

5.2.4 Symmetrical Acceptance Selection

Because cosmic muons travel through CMS from top to bottom, the magnetic field of CMS always splits the trajectory of tracks according to their charges; positive muons will always curve to one side, and negative muons to the other. Thus, any asymmetries arising from the detector or cavern geometry can bias the final measurement of charge ratio.

While the main access shaft is centered along the axis of CMS, and thus does not contribute to a bias, there are two other access shafts which are *not* centered; giving rise to an unbalanced geometric acceptance. In order to eliminate the bias, a set of parabolic selections have been applied which veto muons projected to have passed near or through these shafts *as well as* muons which arrive from the precise opposite direction. The result, separated according to the estimated mean energy loss the muons experience as they passed through the earth is indicated in Figure 5-9. The two cases are for muons which lose little energy (because they pass at least partially through a shaft) and those which do not; the selection requirement itself does not depend on energy or the mean energy loss.

5.2.5 Selection Efficiency Summary

The total selection efficiency, beginning from all muons passing the pre-selection requirements (recorded in a run with a stable magnetic field, has a Muon Spectrometer track in the vicinity of the Silicon Tracker), is indicated in Table 5-1.

The geometry of the Silicon Tracker is, by far, the most stringent selection criteria for this analysis. With respect to all of the 270 M or so cosmic muon events collected during CRAFT, the fraction of muons which propagate into the tracker is less than a percent; and only about 25% of *those* are splittable. All other selection requirements, if taken together, are more than 40% efficient on the remaining sample.

5.3 Monte Carlo Simulation

The CMS Collaboration has adapted a cosmic muon generator called CMSCGEN (The Compact Muon Solenoid Cosmic Generator [65]) from software developed for the L3+C experiment; which generates single random cosmic ray muons (above an energy threshold of 10 GeV) at the surface of the earth based on distributions of muon energy and angles of incidence based on the CORSIKA [66] air shower program.

A map describing the various materials between the Earth's surface and the CMS detector is used to obtain the expected energy loss of simulated muons as a function of their energy, impact point, and incidence direction at the surface [67–69]. Only mean energy loss through the earth is considered for the extrapolated particles, and no multiple scattering has been modeled; since the spread of angles is considered a minor effect on the incident spectrum of cosmic muons. The residual magnetic field surrounding CMS (though it may reach hundreds of gauss) is considered a small effect on the arrival location of muons incident upon the detector, and is not included. The CMS detector response is simulated using the GEANT4 program [70], which takes into account the effects of energy loss, multiple scattering, and showering in the detector.

5.4 Curvature Measurement

Curvature, denoted $C = q/p$, is the main observable used in this analysis to measure charge ratio. Within CMS, however, curvature occurs only in the transverse plane; therefore, it is more appropriate to work with the transverse component of the

momentum[4] instead. The actual transverse curvature of the muon is estimated from the seperate measures of curvature from the top and bottom legs of the split tracks, as in Equation 5–1:

$$C_T = \frac{q}{p_T} = \frac{1}{2}\left(\frac{q_1}{p_{T,1}} + \frac{q_2}{p_{T,2}}\right) \tag{5–1}$$

. . . where q_1 and q_2 are the reconstructed charges and $p_{T,1}$ and $p_{T,2}$ are the reconstructed transverse momenta of the top and bottom legs, respectively, at the PCA. Because the magnetic field is uniform in the region of the tracker volume, the curvature of the two track halves should be identical; providing two (nominally independent) measurements of the same quantity, and therefore a perfect handle for deriving the resolution of the measurement from the data itself. The resolution distribution for the curvature in Equation 5–1 may be estimated by the half-difference of the two quantities, as written in Equation 5–2.

$$d_C = \frac{1}{2}\left(\frac{q_1}{p_{T,1}} - \frac{q_2}{p_{T,2}}\right) \tag{5–2}$$

That this estimator is an accurate representation of the curvature resolution may be tested using a toy Monte Carlo of independent variables, centered on zero. This test has been conducted for various resolution cases in the Appendix, Section A.1 (however, note that these tests apply to only totally uncorrelated measures). So as to check that no significant correlations have been introduced from track fitting and reconstruction; the estimator has also been tested with a realistic Monte Carlo, where the resolution of the curvature may be compared directly with the result from the estimator. The result is indicated in Figure 5-10.

[4] The curvature differs from the transverse curvature by a factor of $\left[1 + \cot^2(\theta)\right]^{-\frac{1}{2}}$ – where θ is the trajectory in the *rz*-plane.

Neglecting simulation jitter, $d_{C,sim}$ – which arises from a charge disagreement owing to a mismatch of simulated hits – the true resolution, δC, is found to be fairly well modeled by the estimator, d_C, for the aggregate total Monte Carlo sample presented in Figure 5-10. Dividing these distributions up into bins of true transverse momentum, however, illustrates some discrepancies; as may be seen in Figure 5-12. The distributions are fit with Gaussian resolution functions – and the ratio of widths, $\sigma(d_C)$ to $\sigma(\delta C)$, are obtained. These ratios, depicted in Figure 5-11, are used as a correction,[5] δd_C, to the resolution estimator:

$$\delta d_C = \frac{\sigma(d_C)}{\sigma(\delta C)}\,,\; d_C \rightarrow \frac{d_C}{\delta d_C} \tag{5–3}$$

The measured curvatures, C_1 and C_2, are then predicted to lie within the (now corrected) resolution estimator, d_C, of the true curvature. Therefore, the expressions may be asserted as in Equation 5–4.

$$\begin{aligned} C^{\text{true}} &\approx \frac{1}{2}\left(C_1 + C_2\right) \\ C_{1,2} &= C^{\text{true}} \pm d_C \end{aligned} \tag{5–4}$$

Note that the true curvature of the muon within CMS need not be estimated at all for the final measurement of charge ratio, since it is reported on the earth surface. In Section 5.5, the methodology for extrapolating the measured curvatures within CMS up to the earth surface will be described; and it is from these propagated measurements that the true curvature, on the surface of the earth, is estimated.

[5] In fact, these corrections can even be predicted analytically (to some extent) based on the strength of the correlations, as shown in the Appendix, Section A.2.

5.5 Unfolding

Various methods of unfolding the spectrum incident upon CMS in order to arrive at measures at the surface of the earth were considered for this analysis [71], including Singular Value Decomposition (SVD) [72], Bayes iteration [73], and several other methods; though a simple matrix inversion was the method chosen for this analysis.

The momentum-binned counts of measured muons, N^{measured}, may be expressed as the result of the action of a migration matrix, M, applied to the binned true number of muons, N^{true}. The true – but unknown – migration matrix element, M_{ij}, gives the probability that a muon with a true curvature C^{true}, which belongs in momentum bin j, will be measured with a curvature (C_1 or C_2) located in bin i. An estimate of the migration matrix, denoted $\widetilde{M}$, is constructed (as detailed in Section 5.5.2) from the measured curvatures. Given an approximation for the migration matrix, it is possible to obtain an estimate for the true number of muons, $\widetilde{N}^{\text{true}}$, given the measured numbers by a process of matrix inversion:

$$\begin{aligned} N_i^{\text{measured}} &= \sum_j M_{ij} N_j^{\text{true}} \\ \widetilde{M} &\approx M \\ \widetilde{N}_i^{\text{true}} &= \sum_j \widetilde{M}_{ij}^{-1} N_j^{\text{measured}} \end{aligned} \tag{5–5}$$

The momentum bins are represented on the surface of the earth. These bins are chosen empirically, with the main requirement being that the spill-over (transfer of muons between bins due to off-diagonal elements in the matrix) is minimized:

$$p = (30, 50, 70, 100, 200, 400, \infty) \ \text{GeV/c} \tag{5–6}$$

One obvious difference between M and $\widetilde{M}$ is the normalization, since the true migration matrix involves the loss of muons as they travel through the earth ($N^{true} \geq$

$N^{measured}$), and the approximation of the migration matrix is built entirely from the measured tracks. The uncertainty in the result due to this effect is estimated in Section 6.2.5.

5.5.1 Propagation to the Earth's Surface

In order to obtain an approximation for the migration matrix, it is necessary to transfer the measured curvatures within CMS to a measure at the surface of the earth. The transverse curvatures measured at the PCA, $C_{T,1}^{PCA}$ and $C_{T,2}^{PCA}$, are first converted to regular curvatures, C_1^{PCA} and C_2^{PCA}, as in Equation 5–7. The numeric subscript indicates that the two terms are nominally independent measures – one from the reconstructed track segment in the top half of the detector and one from the track segment in the bottom half of the detector.

$$\begin{aligned} C_1^{\mathrm{PCA}} &= \frac{q_1}{p_{T,1}} \frac{1}{\sqrt{1+\cot^2\theta_1}} \\ C_2^{\mathrm{PCA}} &= \frac{q_2}{p_{T,2}} \frac{1}{\sqrt{1+\cot^2\theta_2}} \end{aligned} \tag{5–7}$$

The measured curvatures obtained at the PCA are individually propagated to the earth surface. The propagation occurs in two steps. First, a standard helical propagator is used to transfer the tracks out of the CMS volume (to a radius of 8 m), using GEANT to simulate the detector material, and accounting for the magnetic field. Once the track is propagated out of CMS, an analytic extrapolation takes the track through the shaft and cavern geometry, up to the surface of the earth. This extrapolation is linear (a straight line to the surface); which is a reasonable approximation, since the fringing magnetic field outside of CMS is fairly weak (at most a few hundred Gauss), and other effects (such as multiple scattering) produce only negligible errors on the angles of trajectory, which may be accounted for in the systematic uncertainty. Propagation transforms the

curvatures measured within the detector, C^{PCA}, to measures of curvature on the earth surface, C:

$$C_{1,2}^{\mathrm{PCA}} \xrightarrow[propagation]{} C_{1,2} \tag{5–8}$$

To complete the determination of the measured curvatures on the earth surface, an additional resolution effect due to non-uniform energy loss in the earth must be accounted for. Only mean energy losses are estimated in the extrapolation to the earth surface; though in reality there is a wide spread of energies (referred to as "straggling") that may be lost as the particles pass through the earth. In order to estimate the width of this spread of energy losses, the Monte Carlo simulation was used, as it was already available. Muons were propagated through the CMS volume in two ways: once using the standard GEANT simulation, and once using an analytical extrapolator (similar to the one used to transport muons from CMS up to the surface of the earth). While both methods agreed on the mean energy loss, GEANT also produces a realistic spread of energy losses. The relative energy spread within the CMS detector was computed as the difference between the two computed energy losses, divided by the mean energy loss from GEANT. Figure 5-13 illustrates the result: the relative smearing is found to vary from 10% up to more than 20%. Since the actual molasse is fairly homogeneous and uniformly dense – that is, compared with the CMS detector; which has large pockets of gas, particularly in the drift tubes – this is likely an overestimation of the true effect of straggling. Thus, a spread of 10% is assumed to apply to the mean energy loss through the earth, which is applied as a correction to the detector resolution.

5.5.2 Construction of Migration Matrix

For each muon, the two measured values for the curvature, C_1 and C_2, are propagated individually from the detector, as described in Section 5.5.1. Each of the measurements produces an entry for the migration matrix – two per muon – with the corresponding true curvature estimated from the half-sum of the two measurements. The resulting

histograms, binned in p and $p\cos\theta_z$ at the surface of the earth, are presented in Figures 5-14 and 5-15, respectively. The column-wise normalization of these histograms (called the "response matrices") form an approximation, $\widetilde{M}$, of the true migration matrix, which takes the true count of muons and converts it to measured counts. The response matrices are presented in Tables 5-2 and 5-3.

Table 5-1. The total number of muons in the barrel region of CMS surviving, along with both the cumulative and relative selection efficiencies.

requirement	N	ϵ (%)	rel. ϵ (%)
good runs	2372101	–	–
matched trigger	2343585	98.80	98.80
two tracker tracks	579183	24.42	24.71
$N_{DT} \geq 20$	463342	19.53	80.00
N_{DT} z-hits≥ 3	442713	18.66	95.55
$N_{TOB} \geq 5$	428458	18.06	96.78
$\Delta\cot\theta < 0.2$	428204	18.05	99.94
max $\chi^2 < 1500$	415173	17.50	96.96
$p_T > 10$ GeV/c	308390	13.00	74.28
symmetrical acceptance	245218	10.34	79.52

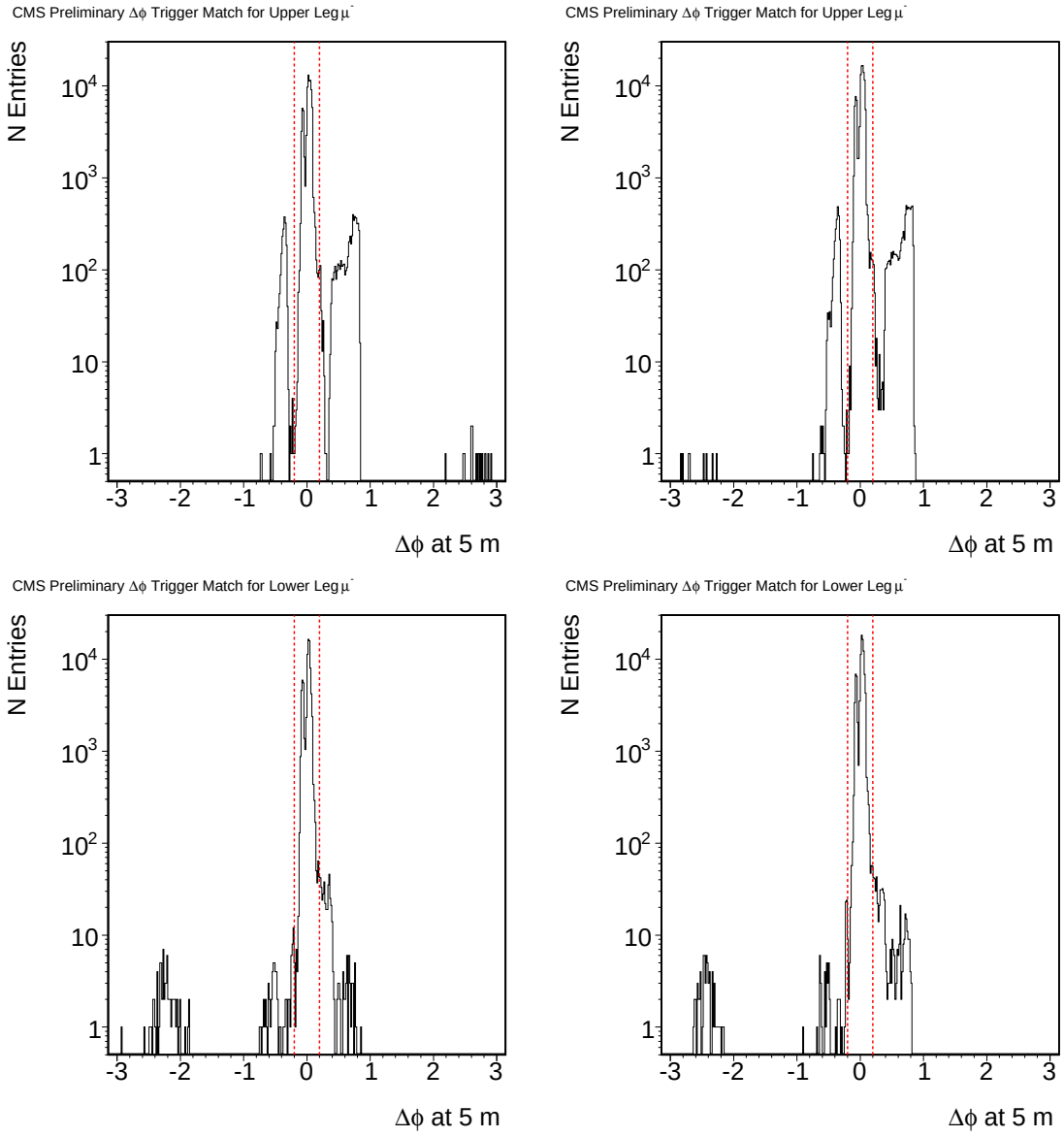

Figure 5-1. DT trigger matching $\Delta\phi$ distributions between the stand-alone muon track propagated to 5 m, and all simultaneous muon triggers. The dashed line at ± 0.2 marks the position of the cut. Top Left: Upper leg distribution for μ^- events. Top Right: Upper leg distribution for μ^+ events. Bottom Left: Lower leg distribution for μ^- events. Bottom Right: lower leg distribution for μ^+ events.

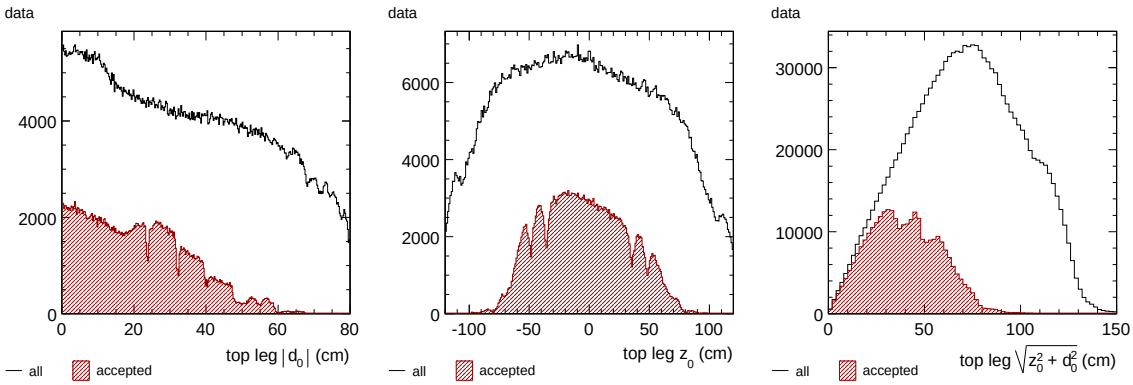

Figure 5-2. PCA parameter distributions before (black line) and after (red histogram) the removal of muons without a splittable tracker track. Left: $|d_0|$. Center: z_0. Right: total displacement of PCA from geometric center of CMS, $\sqrt{z_0^2 + d_0^2}$. The PCA from the top and bottom tracks are nearly identical; therefore, only the measurement from the top leg is displayed.

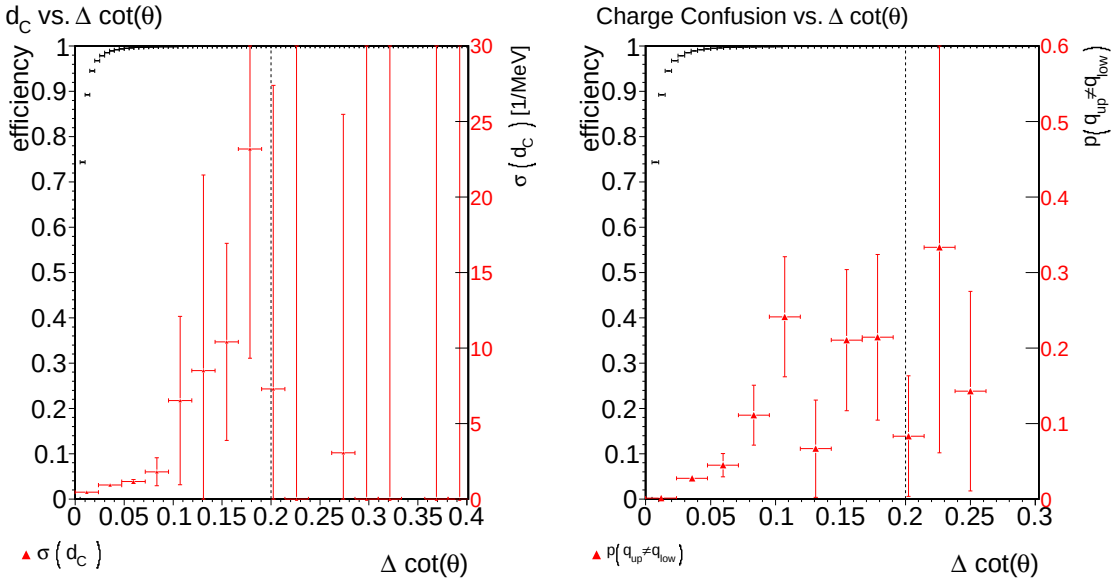

Figure 5-3. Left: curvature resolution metric d_C vs. $\Delta\cot(\theta)$ between track legs. Right: charge confusion vs. $\Delta\cot(\theta)$ between track legs. A selection requirement of $\Delta\cot(\theta) \leq 0.2$ is applied.

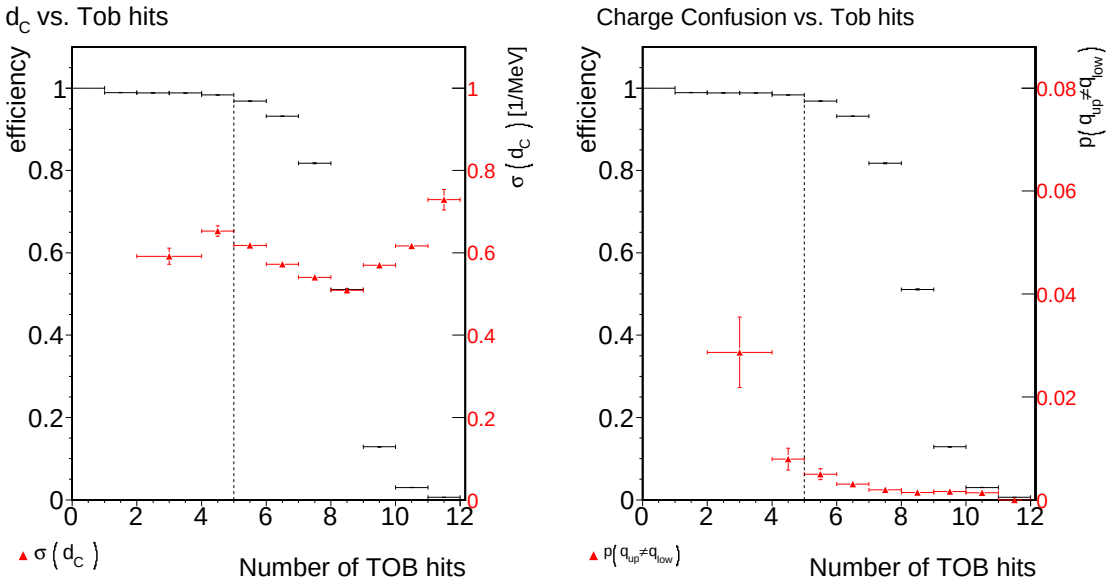

Figure 5-4. Left: curvature resolution metric d_C vs. minimum number of TOB hits. Right: charge confusion vs. minimum number of TOB hits. A selection cut of at least 5 TOB hits is applied.

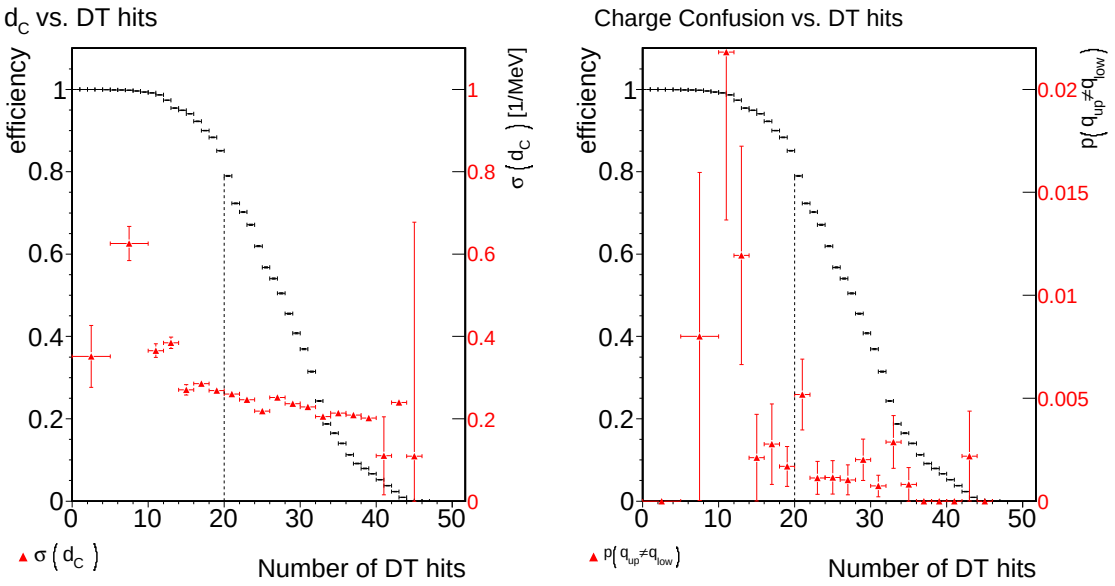

Figure 5-5. Left: curvature resolution metric d_C vs. number of DT hits. Right: charge confusion vs. number of DT hits. A selection cut of 20 or more DT hits is applied.

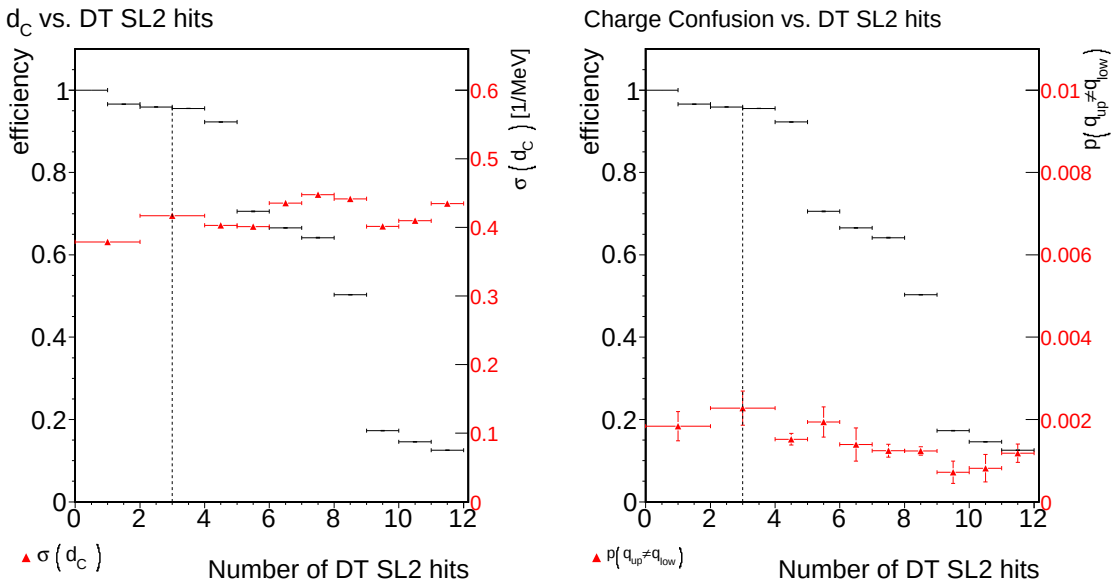

Figure 5-6. Left: curvature resolution metric d_C vs. number of DT hits in SL2. Right: charge confusion vs. number of DT hits in SL2. SL2 is the superlayer responsible for providing measurements of the *z*-position. A selection cut of three or more such hits is applied.

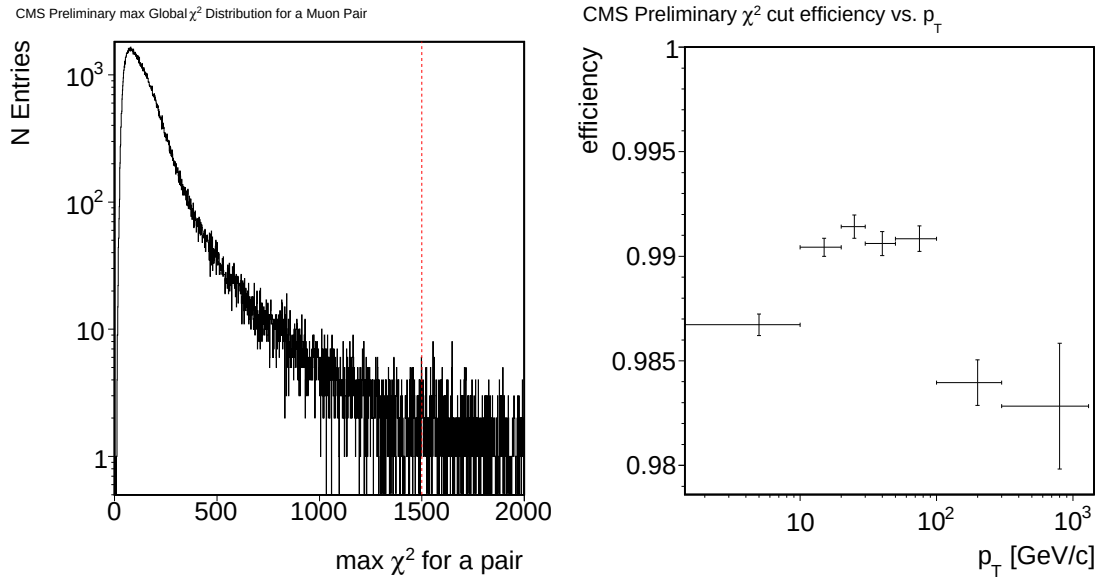

Figure 5-7. Global fit χ^2 requirement. Left: χ^2 of the pair. A selection requirement of 1500 or less is applied. Right: selection efficiency vs p_T.

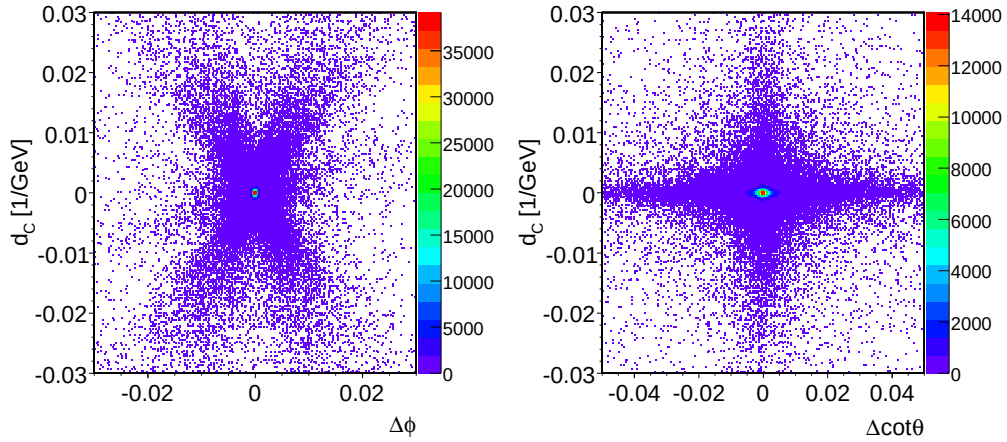

Figure 5-8. Behavior of $\Delta\phi$ vs. d_C (left) and $\Delta\cot\theta_z$ vs. d_C (right). A selection requirement of $\Delta\cot\theta_z \leq 0.2$ is applied.

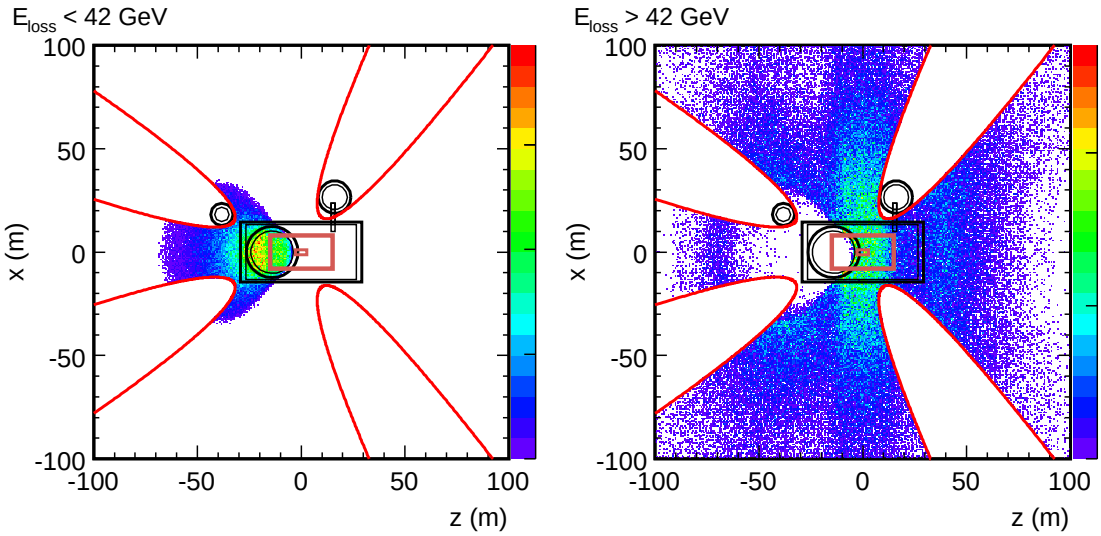

Figure 5-9. Position of incidence of muon tracks (as propagated) to the earth surface; with the outline of the detector cavern, shafts, CMS, and the inner tracker indicated (orthographic view); along with the four applied parabolic selection requirements. Left: effect of selection for muons with $E_{loss} < 42$ GeV; right: effect of selection for muons with $E_{loss} > 42$ GeV.

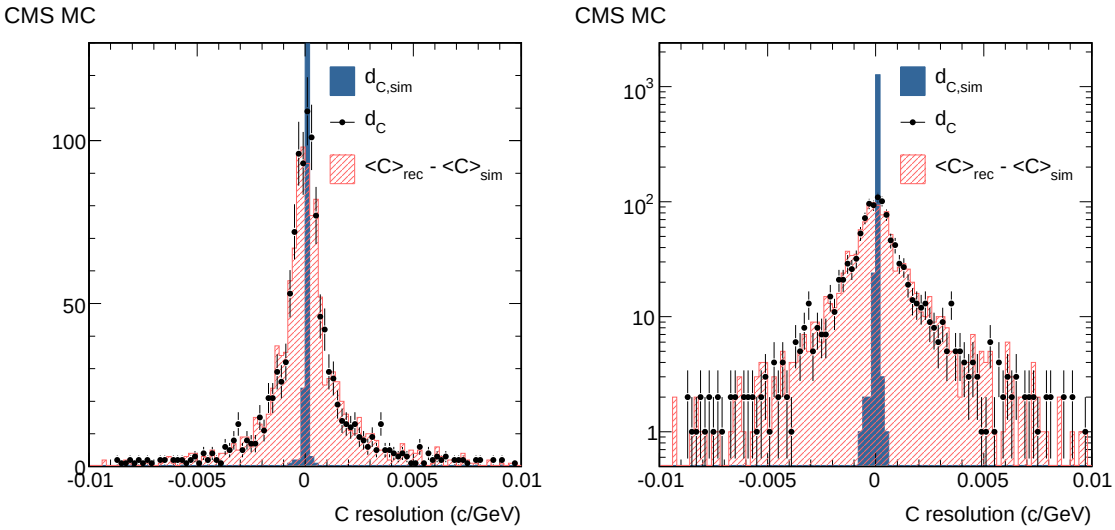

Figure 5-10. Comparison of the resolution proxy d_C (black points) with the simulation jitter $d_{C,sim}$ (solid blue histogram) and the true resolution δC (hashed red histogram). Left: linear scale. Right: logarithmic scale.

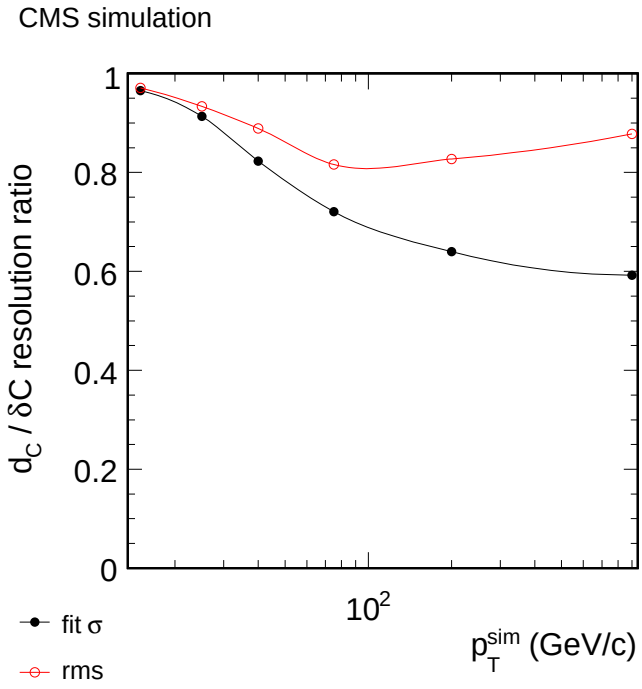

Figure 5-11. $d_C/\delta C$ ratios of widths from the Gaussian fits of the core distributions, and ratios of rms, in bins of true transverse momentum at the PCA.

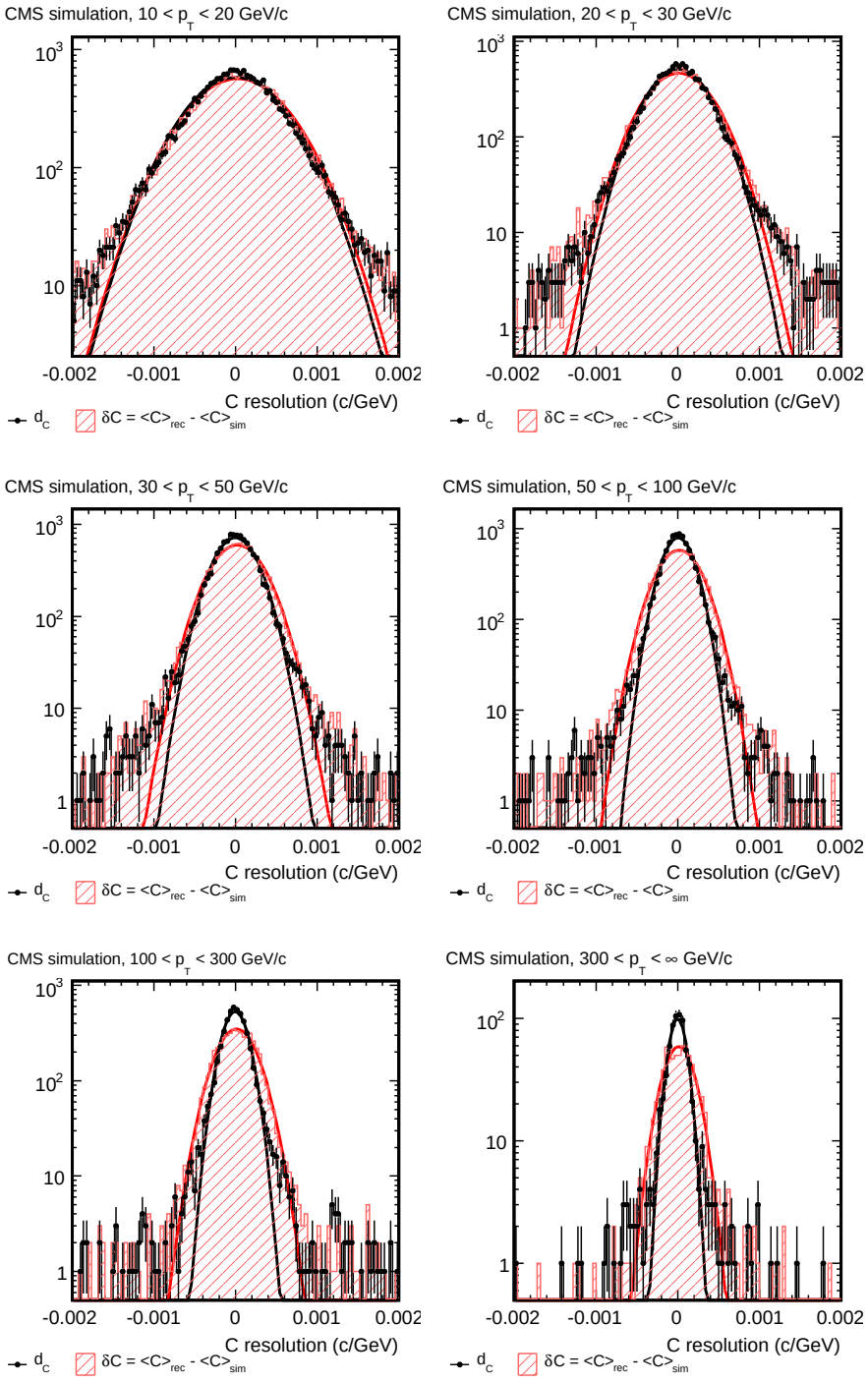

Figure 5-12. Comparison of the (q/p_T) resolution estimator d_C (black solid circles) with the true curvature resolution δC (hashed red histogram), in bins of true transverse momentum at the PCA. The cores of both d_C and δC distributions are fitted with simple Gaussians.

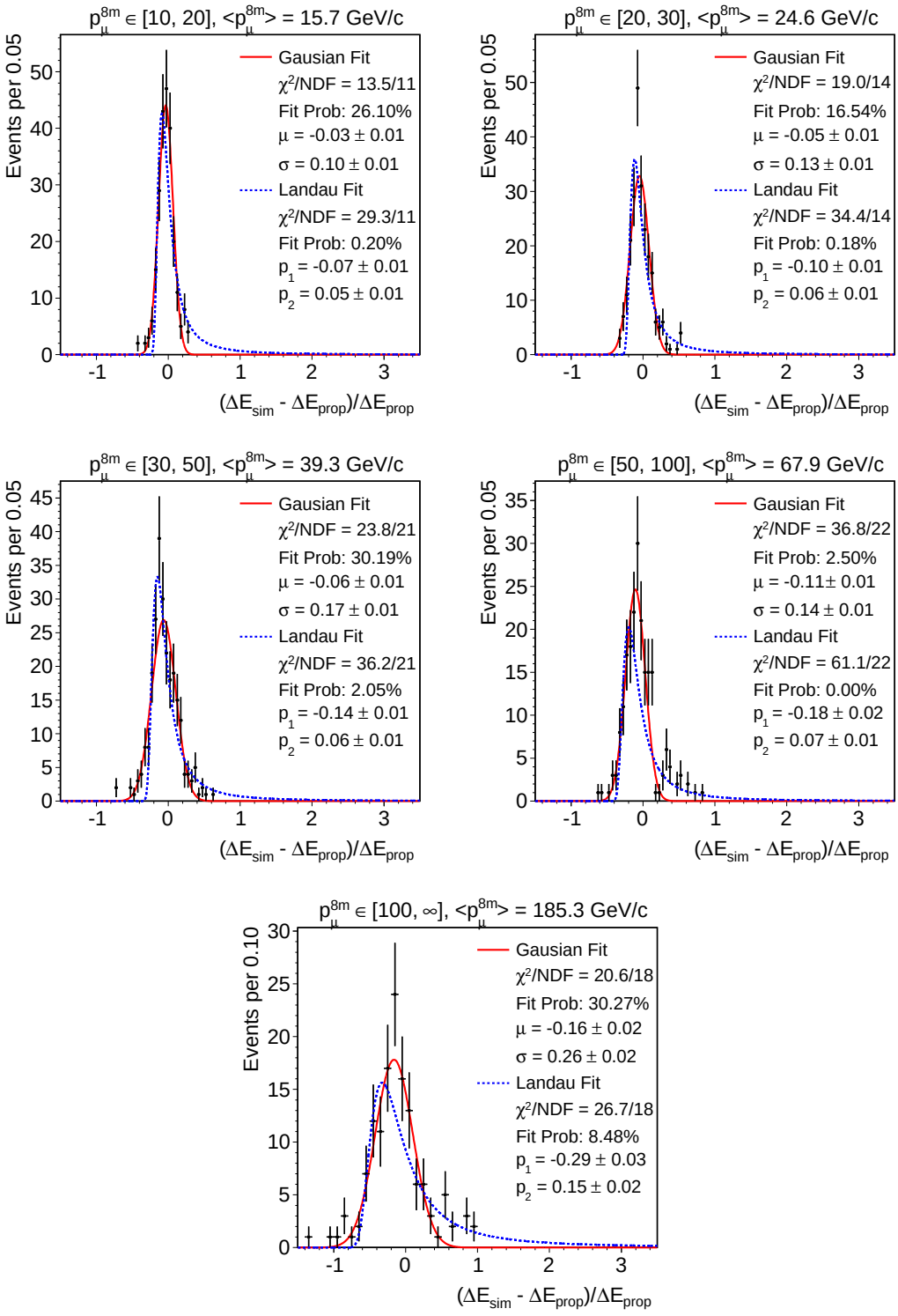

Figure 5-13. Normalized energy loss distributions for muons propagated through the CMS detector, from GEANT Monte Carlo simulation. The distributions are fitted with a Gausian (red dashed) and Landau (blue) and the corresponding fit qualities and parameters are reported

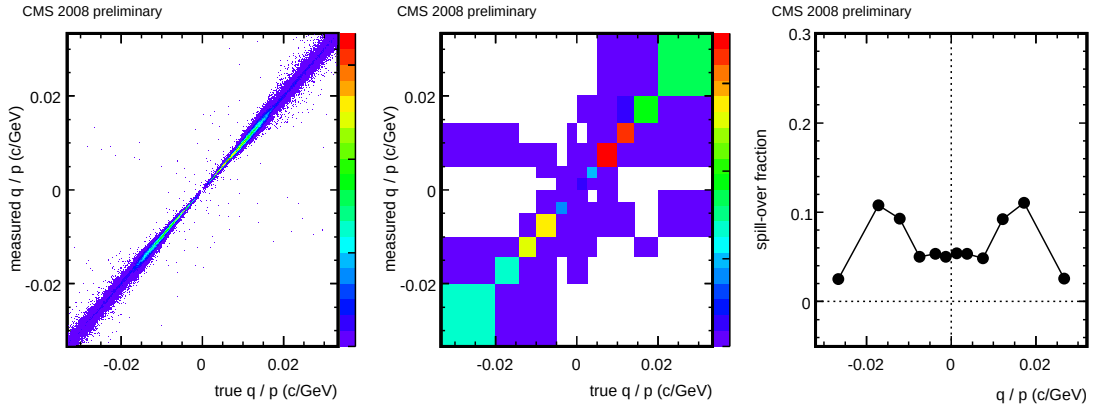

Figure 5-14. Migration histogram which connects measured curvatures with the estimations of true curvature on the surface of the earth in q/p bins. (Left) Fine binning for illustration. (Center) Actual binning. (Right) Off-diagonal spill-over by column.

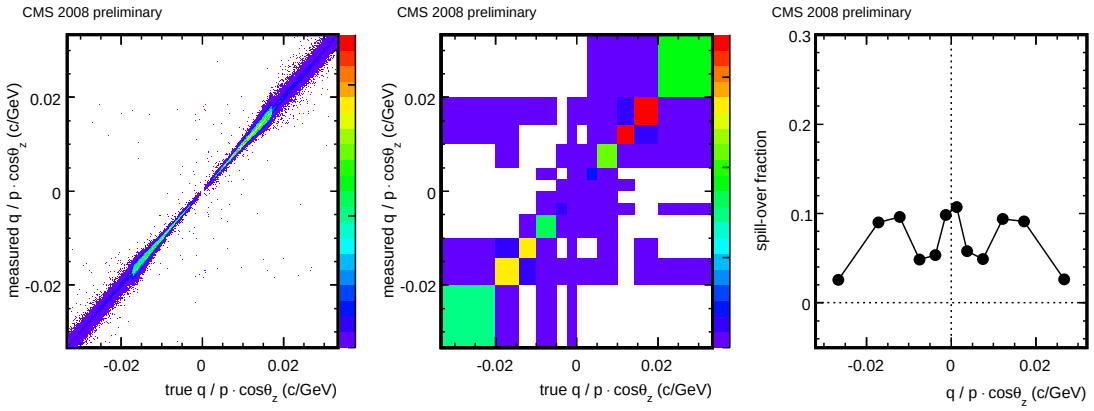

Figure 5-15. Migration histogram which connects measured curvatures with the estimations of true curvature on the surface of the earth in $q/p\cos\theta_z$ bins. (Left) Fine binning for illustration. (Center) Actual binning. (Right) Off-diagonal spill-over by column.

Table 5-2. Response matrix which transforms event counts in bins of true p (x-axis) to event counts in bins of measured p (y-axis). Matrix elements that remain smaller than 10^{-20} are not represented here.

-30	0.9748	0.0231	$< 10^{-4}$	$< 10^{-4}$	–	–	–	–	–	–	–	–
-50	0.0248	0.8925	0.0516	$< 10^{-4}$	–	0.0003	0.0002	–	–	–	–	–
-70	0.0002	0.0843	0.9071	0.0377	0.0001	0.0003	0.0002	$< 10^{-4}$	–	–	$< 10^{-4}$	–
-100	–	–	0.0413	0.9500	0.0404	0.0003	0.0002	$< 10^{-4}$	$< 10^{-4}$	$< 10^{-4}$	–	0.0001
-200	–	–	–	0.0121	0.9468	0.0469	0.0005	$< 10^{-4}$	$< 10^{-4}$	$< 10^{-4}$	–	$< 10^{-4}$
-400	–	–	–	$< 10^{-4}$	0.0125	0.9497	0.0016	–	$< 10^{-4}$	–	–	$< 10^{-4}$
400	–	–	–	–	$< 10^{-4}$	0.0016	0.9463	0.0113	$< 10^{-4}$	–	–	–
200	–	–	–	$< 10^{-4}$	0.0001	0.0003	0.0495	0.9463	0.0112	–	–	–
100	0.0001	$< 10^{-4}$	$< 10^{-4}$	$< 10^{-4}$	–	0.0003	0.0009	0.0420	0.9517	0.0404	$< 10^{-4}$	$< 10^{-4}$
70	$< 10^{-4}$	$< 10^{-4}$	–	–	–	0.0003	–	0.0001	0.0369	0.9079	0.0875	$< 10^{-4}$
50	–	–	–	–	–	–	0.0005	$< 10^{-4}$	$< 10^{-4}$	0.0517	0.8892	0.0253
30	–	–	–	–	–	–	–	–	$< 10^{-4}$	$< 10^{-4}$	0.0233	0.9744
	-30	-50	-70	-100	-200	-400	400	200	100	70	50	30

Table 5-3. Response matrix which transforms event counts in bins of true $p\cos\theta_z$ (x-axis) to event counts in bins of measured $p\cos\theta_z$ (y axis). Matrix elements that remain smaller than 10^{-20} are not represented here.

-30	0.9743	0.0138	–	$< 10^{-4}$	–	0.0010	–	–	–	–	–	–
-50	0.0254	0.9101	0.0692	$< 10^{-4}$	0.0002	0.0020	0.0028	0.0001	$< 10^{-4}$	–	$< 10^{-4}$	0.0001
-70	0.0001	0.0761	0.9036	0.0395	–	0.0010	–	–	$< 10^{-4}$	–	$< 10^{-4}$	–
-100	–	–	0.0272	0.9517	0.0409	0.0030	0.0014	0.0002	$< 10^{-4}$	–	–	–
-200	–	–	–	0.0087	0.9466	0.0813	0.0021	0.0001	$< 10^{-4}$	$< 10^{-4}$	–	$< 10^{-4}$
-400	–	–	–	$< 10^{-4}$	0.0120	0.9018	0.0028	0.0001	$< 10^{-4}$	–	–	–
400	–	–	–	–	0.0002	0.0030	0.8927	0.0154	$< 10^{-4}$	$< 10^{-4}$	–	–
200	–	–	–	$< 10^{-4}$	–	0.0020	0.0922	0.9420	0.0086	–	–	–
100	–	$< 10^{-4}$	–	–	0.0002	0.0010	0.0034	0.0415	0.9509	0.0266	$< 10^{-4}$	$< 10^{-4}$
70	$< 10^{-4}$	$< 10^{-4}$	–	–	–	0.0010	–	0.0002	0.0402	0.9063	0.0771	$< 10^{-4}$
50	$< 10^{-4}$	$< 10^{-4}$	$< 10^{-4}$	$< 10^{-4}$	–	0.0030	0.0028	0.0001	$< 10^{-4}$	0.0670	0.9086	0.0263
30	–	–	–	–	–	–	–	0.0001	$< 10^{-4}$	$< 10^{-4}$	0.0142	0.9735
	-30	-50	-70	-100	-200	-400	400	200	100	70	50	30

CHAPTER 6
SYSTEMATIC UNCERTAINTIES IN THE GLOBAL MUON ANALYSIS

In this Chapter, the systematic uncertainties for the analysis described in Chapter 5 are evaluated. The uncertainties are computed separately for each momentum bin (both p and $p \cdot cos(\theta)$) at the surface of the earth, both raw and after unfolding, and are divided up into contributions from the hardware trigger, quality selection, misalignment, magnetic field, muon rates, molasse model, and detector resolution. Each of them is designed according to Equation 6–1:

$$\sigma^2_{syst} = \xi^2 + \sigma^2_{\xi} \tag{6–1}$$

. . . where ξ is the estimated charge bias induced from each source (equal to zero for the case of no biasing error), and σ_{ξ} is the statistical uncertainty on the estimation of that bias. Note that (in this analysis) finite Monte Carlo statistics sometimes prevents a precision estimation of the systematic error. In such cases, the obtained charge bias, ξ, is itself actually consistent with zero (and therefore the term itself is likely an overestimation of the actual error). As a result, the final systematic error, on a case by case basis, is sometimes assumed to be given by $\sigma^2_{syst} = \xi^2$.

6.1 Error Propagation and Unfolding

In order to incorporate the various systematic uncertainties into the unfolding procedure for error propagation, they must first be divided between the individual positive and negative muon counts for each momentum bin:

$$\frac{\sigma_R}{R} = \sqrt{\left(\frac{\sigma_+}{N_+}\right)^2 + \left(\frac{\sigma_-}{N_-}\right)^2} \tag{6–2}$$

. . . where the $N_{\pm}$ are the count of positive and negative muons, $R = N_{+}/N_{-}$, and the $\sigma_{\pm}$ terms are the total uncertainties on the counts. If the systematic uncertainties on R are presumed to be equally distributed between N_{+} and N_{-}:

$$\frac{\sigma_{syst,+}}{N_{+}} = \frac{\sigma_{syst,-}}{N_{-}} = \frac{\sigma_{syst,R}}{\sqrt{2} \cdot R} \tag{6–3}$$

. . . then, the total uncertainty on the separate counts of positive and negative muons (per momentum bin) may be written:

$$\begin{aligned} \sigma^2_{tot,N} &= \sigma^2_{stat,N} + \sigma^2_{syst,N} \\ &= N + N^2 \cdot \frac{\sigma^2_{syst,R}}{2 \cdot R^2} \end{aligned} \tag{6–4}$$

The true count of positive or negative muons in the ith momentum bin is computed by multiplying the raw counts from the various j momentum bins by the normalized and inverted migration matrix. The uncertainties on the unfolded ratios are then computed as in Equation 6–5.

$$\sigma^2_{i,\text{unfolded}} = \sum_{j} \left(\widetilde{M}^{-1}_{ij} \right)^2 \sigma^2_{j} \tag{6–5}$$

The relative systematic uncertainties on R are reported both raw and after accounting for the unfolding procedure – in either case using the split form defined in Equation 6–2. For the raw uncertainty, the $\sigma_{\pm}$ terms are computed from Equation 6–4; while for the unfolded one, they are computed from Equation 6–5.

6.2 Sources of Systematic Uncertainty

6.2.1 Trigger

Relative differences in the efficiency of the hardware trigger system for muons of one charge vs. the other can cause an overall charge bias. This bias, ξ_{trig}, may be expressed:

$$\xi_{trig} = \frac{\eta_+}{\eta_-} - 1 \tag{6–6}$$

The $\eta_\pm$ terms in Equation 6–6 refer to the trigger efficiency for *any* barrel trigger to fire in response to a muon event of the given charge. In order to estimate the charge bias, the sample of recorded events is first divided into a set of positive and a set of negative muons. Within either sample, the probability of a trigger may be expressed:

$$\eta = p(\uparrow \textit{ or } \downarrow) = p(\uparrow) + p(\downarrow) - p(\uparrow \textit{ and } \downarrow) \tag{6–7}$$

. . . where the arrows refer to whether a trigger originated in one of the sub-detectors of the top or bottom of CMS, and the $\pm$ subscript denoting whether the efficiency is for positive or negative muons has been dropped for brevity. The efficiencies are estimated using tag-and-probe tests, which are performed by tagging a trigger on one side of CMS and probing for the existence of a trigger on the opposite side (using the reconstructed track to determine whether any matches exist). For example, the estimator $\tilde{p}(\uparrow)$ of the *true* upper trigger probability, $p(\uparrow)$, is constructed from the ratio of the number of probes to the number of tags:

$$\widetilde{p}(\uparrow) \equiv \frac{n(\uparrow \textit{ and } \downarrow)}{n(\downarrow)} \approx \frac{p(\uparrow \textit{ and } \downarrow)}{p(\downarrow)} = \frac{p(\uparrow) \cdot p(\downarrow)}{p(\downarrow)} = p(\uparrow)$$

$$\therefore p(\uparrow) \approx \widetilde{p}(\uparrow) \tag{6–8}$$

. . . and, likewise, $p(\downarrow) \approx \widetilde{p}(\downarrow)$. These tests give an accurate estimate of the trigger efficiency if the spectrum of muons selected by the tag is well representative of the entire considered spectrum for which the trigger efficiency is desired.[1] The probability of both kinds of triggers accepting the event, $p(\uparrow \textit{ and } \downarrow)$, may also be estimated in a similar fashion, with the count of triggers on both sides of CMS firing compared with the count of events in which either trigger fired:

$$\begin{aligned} \widetilde{p}(\uparrow \textit{ and } \downarrow) \equiv \frac{n(\uparrow \textit{ and } \downarrow)}{n(\uparrow \textit{ or } \downarrow)} &\approx \frac{p(\uparrow \textit{ and } \downarrow)}{p(\uparrow \textit{ or } \downarrow)} \\ \therefore p(\uparrow \textit{ and } \downarrow) &\approx \widetilde{p}(\uparrow \textit{ and } \downarrow) \cdot p(\uparrow \textit{ or } \downarrow) \end{aligned} \tag{6–9}$$

Combining the results from Equations 6–8 and 6–9; Equation 6–7 may be rewritten in terms of the appropriate estimators:

$$\begin{aligned} p(\uparrow \textit{ or } \downarrow) &= p(\uparrow) + p(\downarrow) - p(\uparrow \textit{ and } \downarrow) \\ &\approx \widetilde{p}(\uparrow) + \widetilde{p}(\downarrow) - \widetilde{p}(\uparrow \textit{ and } \downarrow) \cdot p(\uparrow \textit{ or } \downarrow) \\ &\approx \frac{\widetilde{p}(\uparrow) + \widetilde{p}(\downarrow)}{1 + \widetilde{p}(\uparrow \textit{ and } \downarrow)} \end{aligned} \tag{6–10}$$

From these estimations on the trigger probability, the respective trigger efficiencies for positive and negative muons are computed. The resulting charge bias, previously defined in Equation 6–6, is illustrated in Figure 6-2.

[1] Such is the case for muons in this analysis, since the split muon requirement guarantees that the considered tracks traverse the entire detector; and, further, because they are constrained to the center of the machine, and therefore have similar ranges of incident angles as they cross through the Muon Spectrometer.

6.2.2 Selection

The selection requirements applied in this analysis were chosen to be as charge blind to the measurement of charge ratio as possible; however *any* selection may potentially have a different efficiency for positive and negative muons. To estimate the amount of systematic bias introduced by the muon selection, a so-called $N-1$ test is applied for each of the considered requirements. That is, all of the requirements *except* for the one under study are applied, and the ratio of efficiencies ($\eta_{\pm}$) of the final selection on the remaining sample is used as an estimate for the charge bias:

$$\xi_{sel} = \frac{\eta_{+}}{\eta_{-}} - 1 \tag{6–11}$$

The four selection requirements were: the minimum number of DT hits, the minimum number of z-measuring hits in the DT (hits in Superlayer-2), the minimum number of hits in the Silicon Tracker outer barrel, and the maximum global-fit track χ^2. The sample was divided up into positive and negative muons, and the relative efficiencies of the Nth requirements were compared. The resulting estimate of the charge bias for each of these requirements are illustrated in Figures 6-3 through 6-6.

An implicit form of selection arises from the split-track requirement. Recall that, in Figure 5-2, it was shown that requiring split-tracks has the indirect effect of selecting on small impact parameters; and in particular, the total distance between the PCA and the center of the detector. Figure 6-12 gives the relative effect on charge against the three principle impact parameters. Since the split-track efficiencies are sensitive only to the magnitude of the impact parameter (independent of which side of the detector the track is on), no charge bias is expected to result from this selection.

Overall, selection is found to be a major source of systematic uncertainty in the analysis (the results for each selection requirement are given in Tables 6-1 and 6-2). The two major contributors to this source of uncertainty are the requirements on the number of hits in the DT and TOB. In order to show that these selection requirements

are not picked at a local (charge-bias inducing) maxima, the relative effect on the charge ratio is plotted against the choice of requirement in Figure 6-13.

6.2.3 Mis-Alignment

The precise alignment [74] of all the tracking-detector components is crucial for accurate reconstruction of high-p_T muons, which experience only slight curvatures within the detector. In particular, because this analysis involves hit information from both the muon spectrometers and the silicon tracker, the reconstructed charge and momenta of the cosmic tracks are highly sensitive to the relative alignment between the tracker and muon systems. In order to estimate the effect of such alignments, a comparison is performed using two alignment scenarios with the Monte Carlo: one in which the detector has been arranged in an "ideal" alignment, and one in which it has been randomly misaligned by realistic amounts equal to the uncertainties of the realistic "startup" alignment of the detector (as they are currently understood).

A study was conducted in both scenarios; with the charge ratio measured separately in both sets of detector conditions. The difference in the resulting measurement is assessed as the charge bias due to misalignment, as in Equation 6–12. The result of this study is given in Figure 6-7.

$$\xi_{align} = \frac{R_{ideal} - R_{startup}}{R_{ideal}} \tag{6–12}$$

A global deformation of the detector could be missed during the alignment procedures (a so-called "χ^2-invariant" or "weak" mode [75]), and potentially affect the charge ratio. The most problematic deformation would be a mode which caused a constant offset in $q/p_{\mathrm{T}}^{\mathrm{PCA}}$, different from zero, affecting the momentum scale for cosmic muons of opposite charge in opposite directions. A two-parameter fit of the simulated $q/p_{\mathrm{T}}^{\mathrm{PCA}}$ distribution to the data is performed using muons in the range $p_{\mathrm{T}}^{\mathrm{PCA}} > 200 GeV/c$, leaving the unknown charge ratio and the $q/p_{\mathrm{T}}^{\mathrm{PCA}}$ offset in the simulation to vary freely in the fit. An offset of 0.043 ± 0.022 c/TeV is found. The measured muon momenta are corrected

for this offset and its uncertainty is included as an additional systematic uncertainty on R, fully correlated between the two underground measurements. The effect on the ratio is approximately 1% and 4%, respectively, in the two highest momentum bins; and neglible below.

6.2.4 Magnetic field

The magnetic field at CMS [76], though generally a uniform 4 T within the tracker volume, is quite complex throughout the solenoid and out into the return yolk and Muon Spectrometers. The TOSCA field mapper is used in CMS to estimate the magnetic field. In order to estimate the effect of uncertainty in the field maps, two separate conditions were studied; one using an older map of the magnetic field, and one which uses the map as it is currently understood. It is assumed that the relative difference between the two maps is roughly equal to the difference between the current field mapping and the true magnetic field conditions.

The charge ratio was measured for a sample of events in data with both field conditions, and the relative difference in the result was compared. The expression for the bias in the resulting charge ratio is written in Equation 6–13, and the resulting uncertainty is indicated in Figure 6-8.

$$\xi_{bfield} = \frac{R_{current} - R_{old}}{R_{current}} \tag{6–13}$$

6.2.5 Muon Rates

Some muons, particularly for the lowest considered momenta, are absorbed in the earth before they can reach CMS. *A priori*, this is expected to be a charge blind process; however there are several factors which can induce a charge bias in this process. For instance, positive muons lose slightly more energy (about 0.15%) than do negative muons as they travel through matter [26]; causing a slight charge bias, as indicated in Figure 6-9.

Although the asymmetric access shafts were removed as a source of bias by application of the parabolic selections on both sides of the detector, other (unaccounted for) features of the cavern or detector may induce a charge bias. In order to check, two samples of Monte Carlo, each divided up according to muon charge, are examined. The first sample is a representation of the ideal muon flux at the earth surface (without any influence due to the local geometry of CMS or the shafts and caverns of Point-5). The second sample is representative of the portion of the spectrum expected to reach the tracker volume; and is thus subject to all of the aforementioned complications. The ratio of the two fluxes, representative of the relative acceptance of CMS, is:

$$\eta = \frac{N_{accepted}}{N_{earth}} \tag{6–14}$$

. . . where $N_{accepted}$ and N_{earth} are the counts (for either positive or negative muons) from the sub-sample reaching the silicon tracker of CMS, and the sub-sample representing the total spectrum at the surface of the earth, respectively. The charge bias is then expressed as in Equation 6–15.

$$\xi_{rates} = \frac{\eta_{+}}{\eta_{-}} - 1 \tag{6–15}$$

The result of this exercise is represented in Figure 6-10. The statistical uncertainty, due to the practical limitation of finite Monte Carlo statistics (very few muons at the surface of the earth actually *reach* the detector), is found to be significantly larger than the bias estimated to come from this source.

6.2.6 Molasse Model

An accounting of the geology of the detector site – in order to understand the material overburden – is one of the first considerations which must be made in order to convert any measurements of cosmic muons incident upon the detector into measurements at the surface of the earth. While no comprehensive geological survey was performed after the excavation of the shafts and caverns for CMS; extensive surveying

was done both prior to the construction of the ring in the early 1980's for the construction of LHC's predecessor (LEP), and in the mid 1990's for the two main excavations needed for the LHC (that is, the CMS and ATLAS caverns at Point 5 and Point 1, respectively).

The molasse above CMS is known to be composed of more than 70 m of moraines and rock left behind during glacial advances and retreats during the Alpine Riss and Würm eras [77]. The moraine itself is a complex array of strata with thin layers (nominally 50 cm) of silt, sand, gravel; along with layers of sandstone up to 5 m thick. Within the moraine, there are also two aquifer levels – each estimated to vary from 10 m to 22 m thick over the region [78, 79].

In order to estimate the molasse model systematic, two *additional* propagations of the muons were performed; one through an extra amount of material overburden (equal to the molasse uncertainty), and one through correspondingly less material. Divided by material type, there are roughly 50 m of moraines and 22 m of sandstone, with a relative uncertainty on the density of each component of $\sim$5%. This uncertainty corresponds to a total of 3 m of rock (or, equivalently, about 5 m moraines). The resulting charge bias is expressed in Equation 6–16, with the corresponding uncertainty indicated in Figure 6-11.

$$\xi_{rock} = \frac{R_{+3m\ rock} - R_{-3m\ rock}}{R} \tag{6–16}$$

6.2.7 Resolution Estimates

In Section 5.4, it was shown that the two legs of the split muon track were found to have a persistent correlation within the realistic Monte Carlo sample, due to some aspect of the underlying track reconstruction. Such a correlation would cause the prescribed detector resolution estimator, d_C, to underestimate the actual resolution by a predictable amount; however the correlation itself cannot be derived from the data. A correction, given in Equation 5–3, was constructed by comparing the resolution estimator with the true resolution. In order to account for the fact that the correction itself

is not data-driven, an additional systematic uncertainty equal to half of the correction is assumed.

A possible explanation for the observed correlations is related to the alignment, since relative offsets within the detector may result in shifting the two (nearby) measurements similarly. While the Monte Carlo approximates mis-alignments by randomly shifting groups of detector elements around according to the estimated positional uncertainties, the data is aligned differently (using individual tracks). Note that – despite this obvious difference – a similar correlative effect is likely to appear, since some of the *same* tracks used to measure the charge ratio are also used to perform the alignments of the silicon tracker and muon systems [80, 81], and furthermore, from which the Monte Carlo alignment uncertainty has been approximated.

6.3 Other Sources of Error

6.3.1 Atmospheric Conditions

The local elevation where CMS is installed is approximately 500 m above sea-level. In order to explore the effects of atmospheric conditions on measurements involving cosmic muons; public weather, solar, and geomagnetic data from the run period was used to estimate and simulate the atmospheric density, from ground level to high altitudes. No extreme atmospheric conditions were observed during the course of the experiment, and the relative variation of atmospheric density with respect to the mean sea-level, as well as the offset between mean sea-level and the actual elevation of the earth surface near CMS, are extremely small and have been neglected. Details of this study are presented in Appendix B.

6.3.2 Unfolding Procedure

In order to check whether the unfolding procedure itself induces a charge bias in the final result, an estimator is constructed using an ensemble of toy Monte Carlo experiments. For each experiment, a number of positive and negative muons at the surface

of the earth is constructed from a Poisson distribution, using the migration matrix estimated from data to determine the relative numbers. The curvature of each toy muon is randomly assigned according to the q/p distribution in data, and smeared according to the energy loss resolution. Two measurements of the resulting curvature are randomly extracted from the actual migration matrix (to simulate the split track measurements) and are used to construct a new migration matrix for the experiment. Finally, the toy sample is unfolded using the new migration matrix to generate a measured curvature distribution, which is then compared with the input curvatures. The toy experiment was repeated 500 times; the resulting pulls distributions are summarized in Figure 6-15. The resulting bias is negligible, as the mean values for all bins are almost zero and the widths are very close to one.

6.4 Summary

The statistical uncertainty is approximately 1% for all bins except the highest momenta; where it has a maximum of over 3% and 6% for the total momentum and vertical momentum formulations, respectively. The systematic uncertainty is under 1% in most bins, except for the lowest momentum bin (due to increased uncertainty in the detector acceptance) and the highest two momentum bins (due to the increased sensitivity to magnetic field and alignment effects). The maximum systematic uncertainty in any bin is under 5%. It is found that selection is an important source of systematic uncertatiny for all momentum bins. The systematic uncertainty due to selection requirements are given in Tables 6-1 and 6-2, for the total and vertical momenta, respectively. The final systematic uncertainties, including all effects, are summarized in Table 6-3.

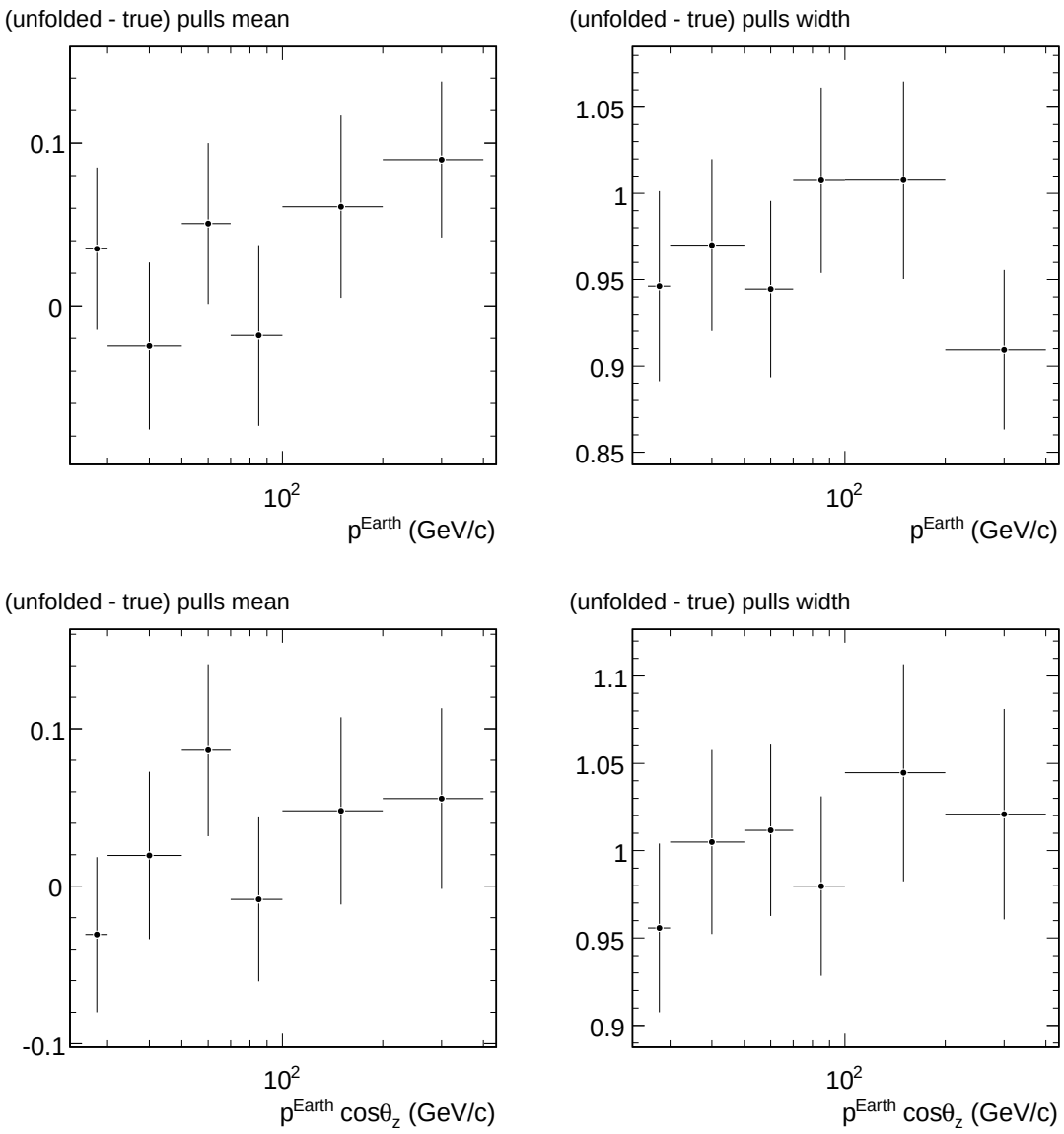

Figure 6-1. Charge ratio pulls distributions for 500 experiments. (Left) Pulls means. (Right) Pulls widths. (Top) In p bins. (Bottom) In $p\cos\theta_z$ bins.

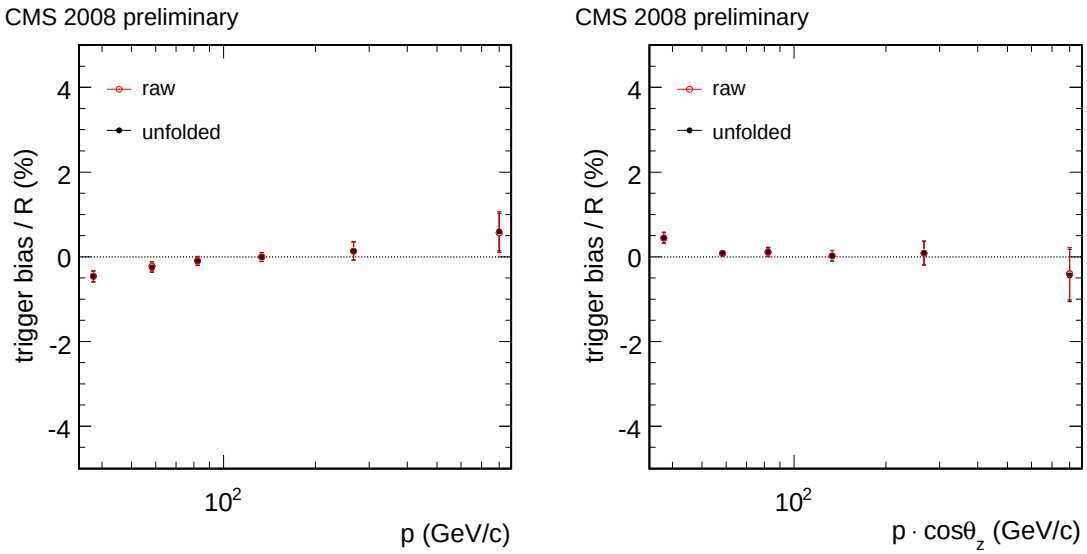

Figure 6-2. Charge bias due to the hardware trigger $(\xi \pm \sigma_\xi)/R$.

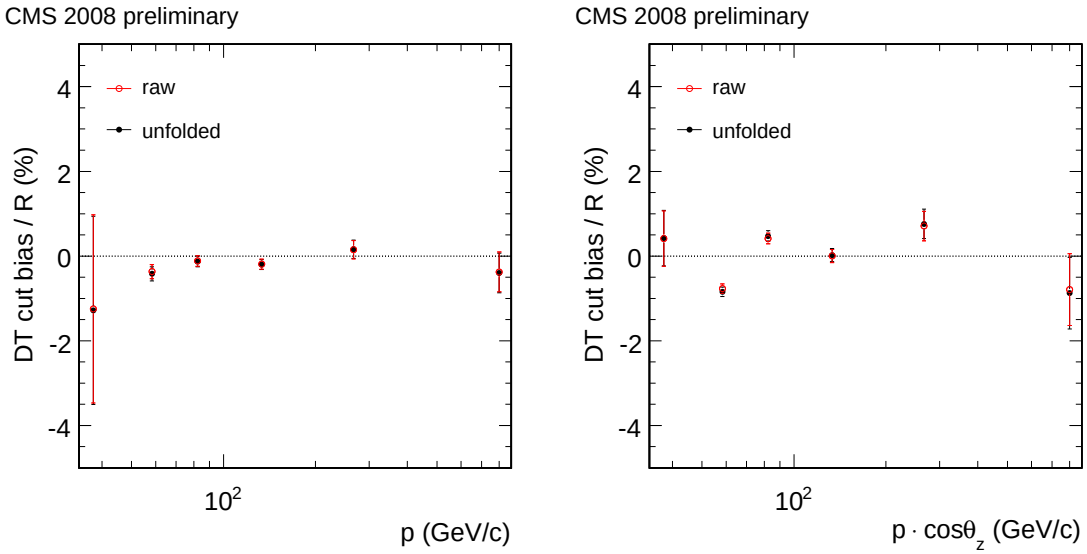

Figure 6-3. Charge bias $(\xi \pm \sigma_\xi)/R$ from selection on 20 or more Drift Tube hits.

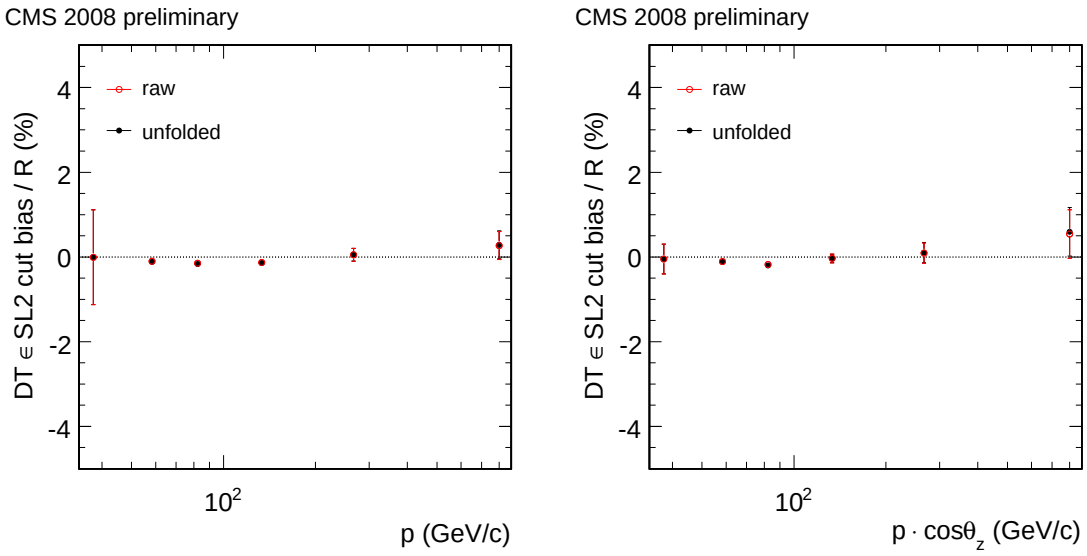

Figure 6-4. Charge bias $(\xi \pm \sigma_\xi)/R$ from selection on three or more z measurings hits (Drift Tube Superlayer-2).

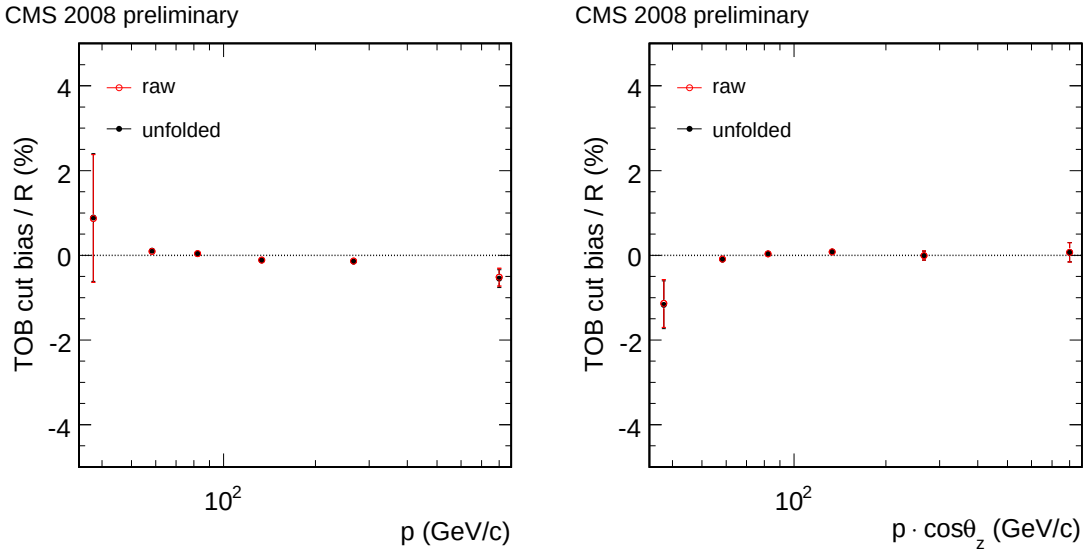

Figure 6-5. Charge bias $(\xi \pm \sigma_\xi)/R$ from selection on five or more outer tracker barrel hits.

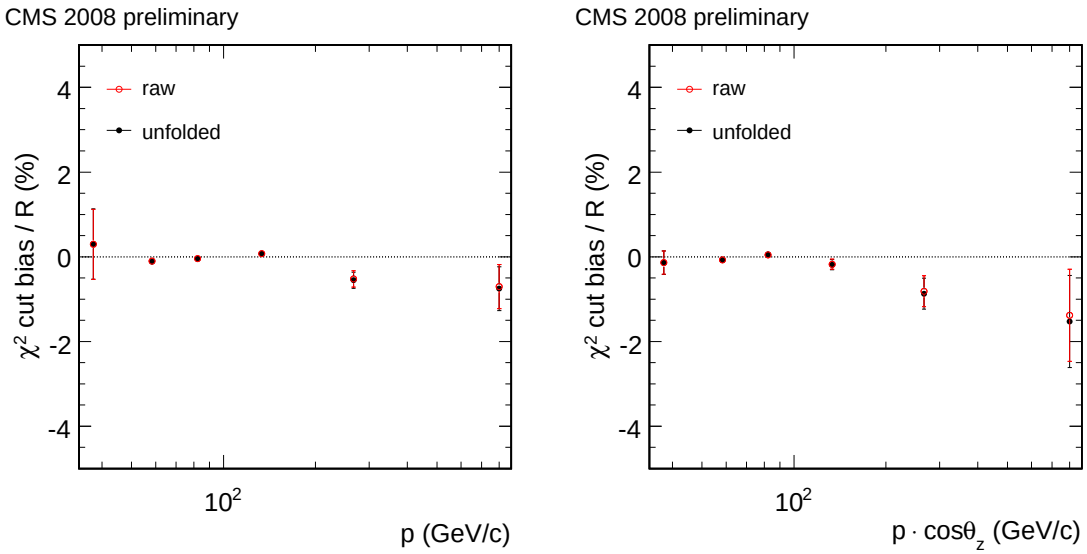

Figure 6-6. Charge bias $(\xi \pm \sigma_\xi)/R$ from selection on the maximum χ^2.

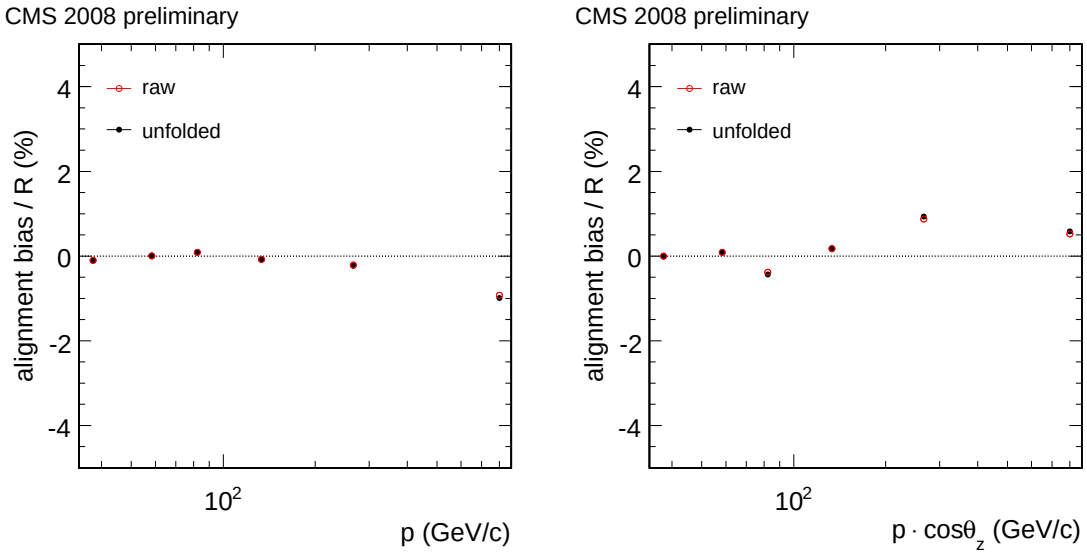

Figure 6-7. Charge bias $(\xi \pm \sigma_\xi)/R$ from alignment uncertainty.

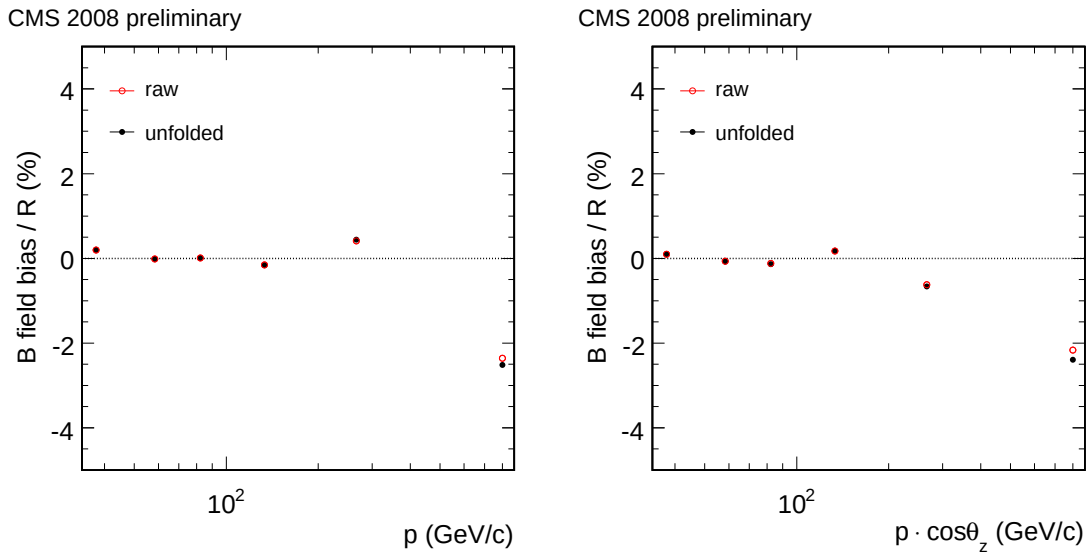

Figure 6-8. Charge bias $(\xi \pm \sigma_\xi)/R$ from magnetic field uncertainty.

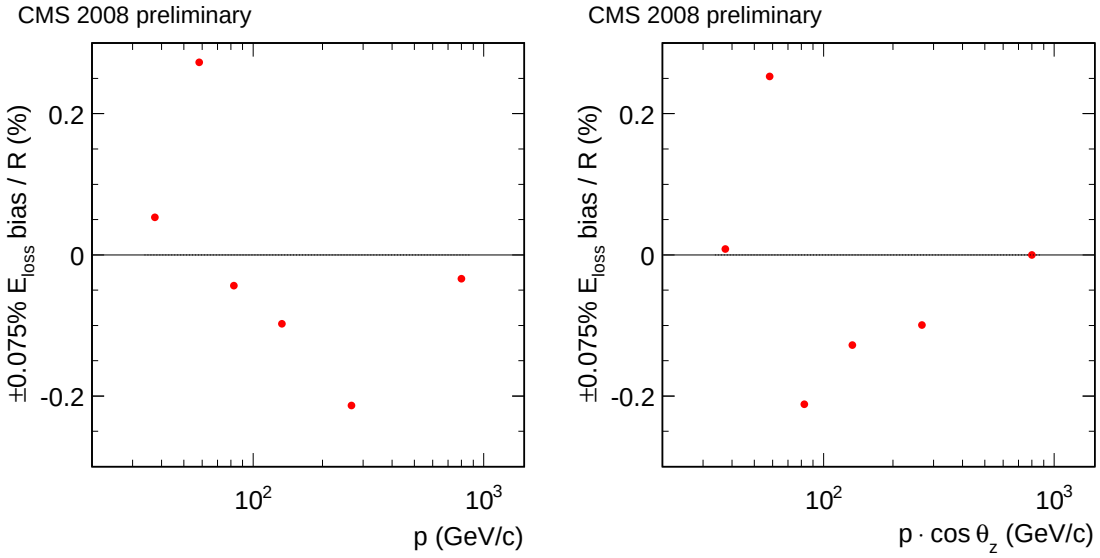

Figure 6-9. Charge bias $(\xi \pm \sigma_\xi)/R$ from asymmetric energy loss between positive and negative muons as they travel through matter.

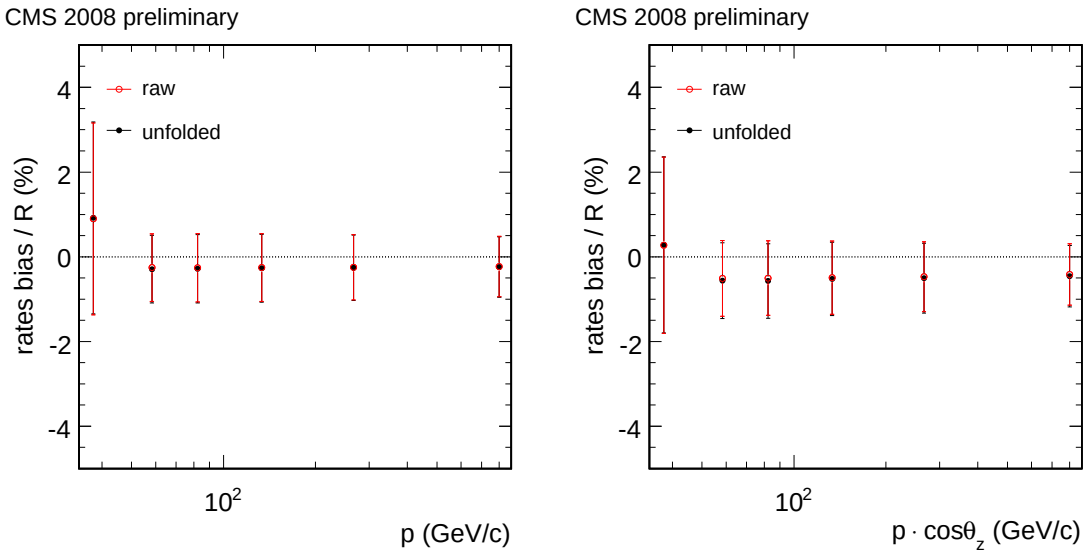

Figure 6-10. Charge bias $(\xi \pm \sigma_\xi)/R$ from muon rate uncertainty.

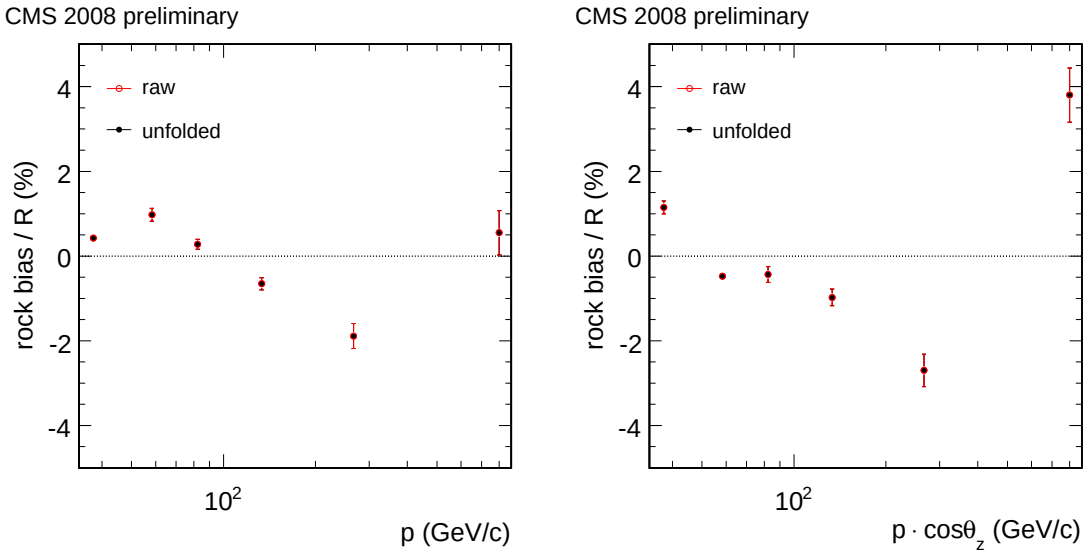

Figure 6-11. Charge bias $(\xi \pm \sigma_\xi)/R$ due to molasse uncertainty.

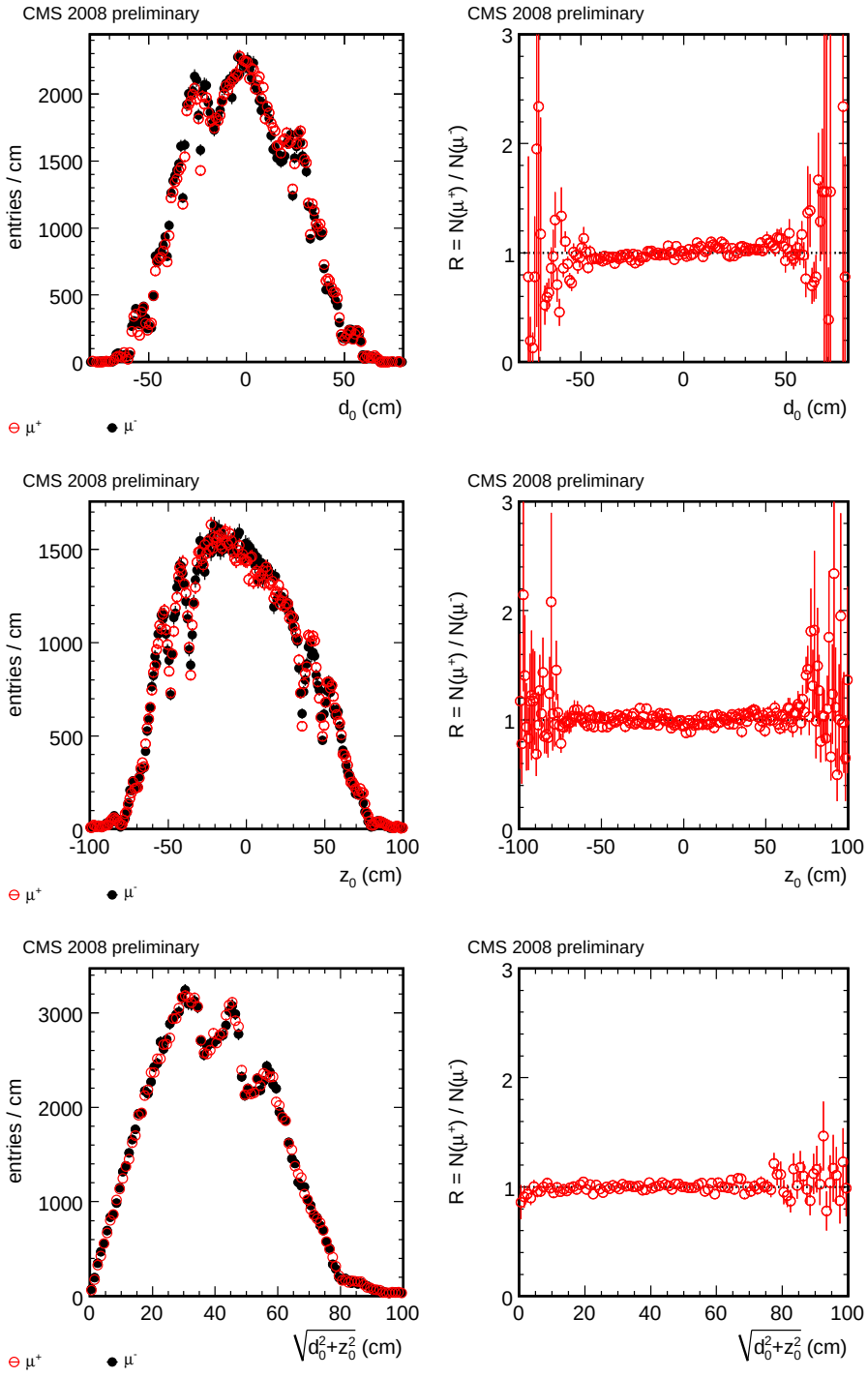

Figure 6-12. Left: distributions of μ^+ and μ^-, with the second normalized to the first (for a better shape comparison) vs. various impact parameter quantities. Right: ratio of the normalized distributions.

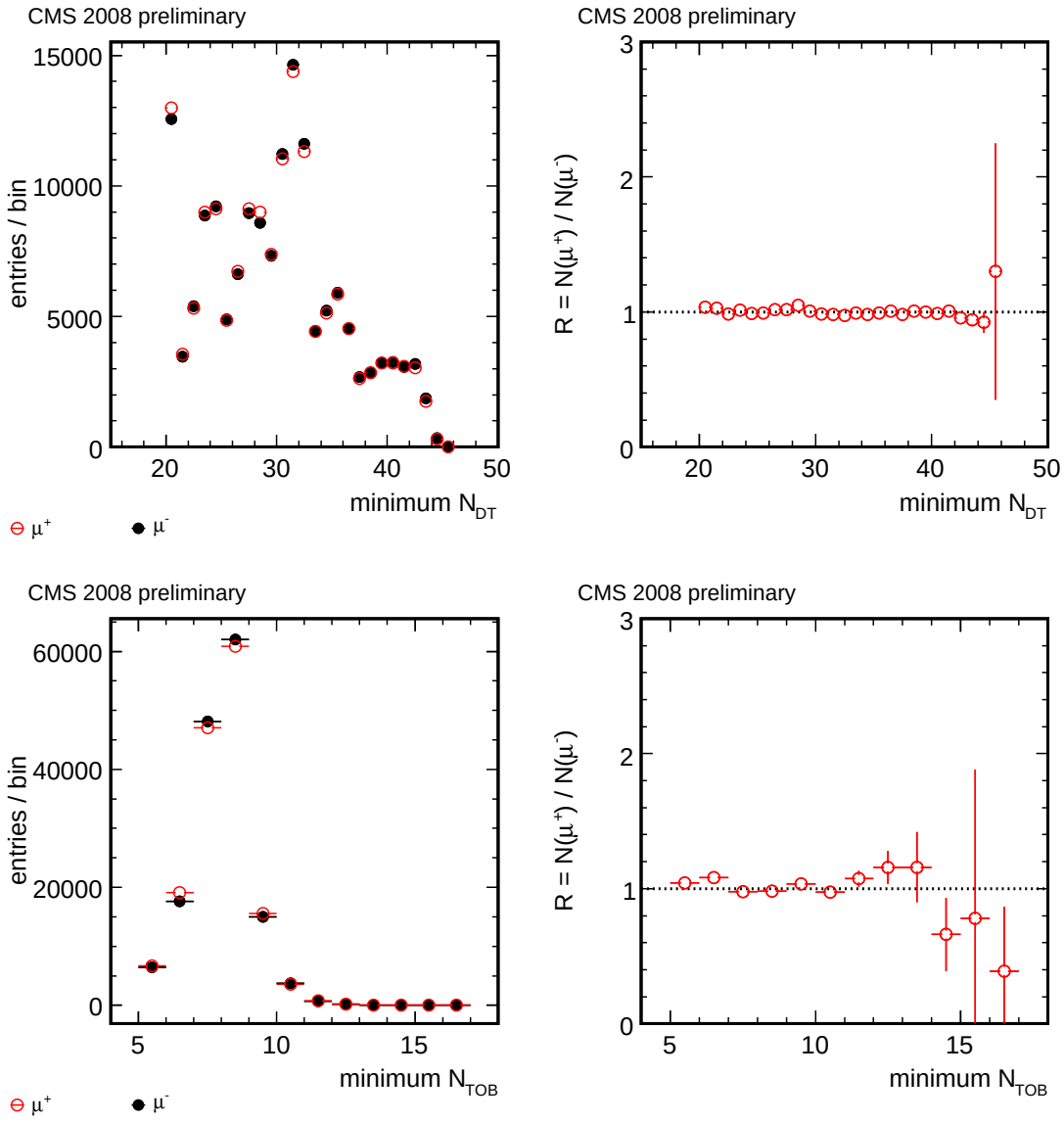

Figure 6-13. Left: distributions of μ^+ and μ^-, with the second normalized to the first (for a better shape comparison) vs. different choices for selection requirements. Right: ratio of the normalized distributions.

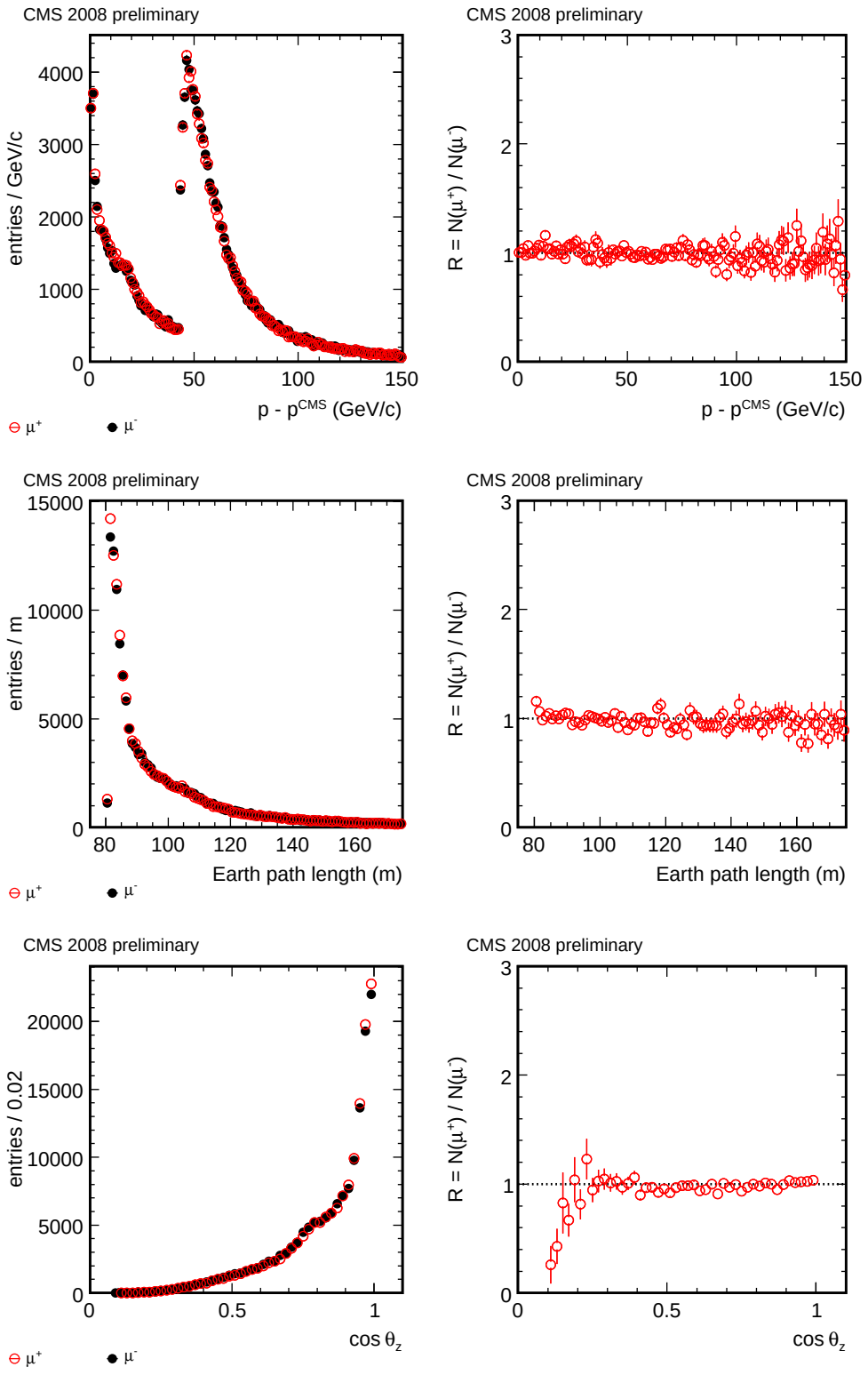

Figure 6-14. Left: distributions of μ^+ and μ^-, with the second normalized to the first (for a better shape comparison) vs. variables relevant to the path the muons take through the earth to reach CMS. Right: ratio of the normalized distributions.

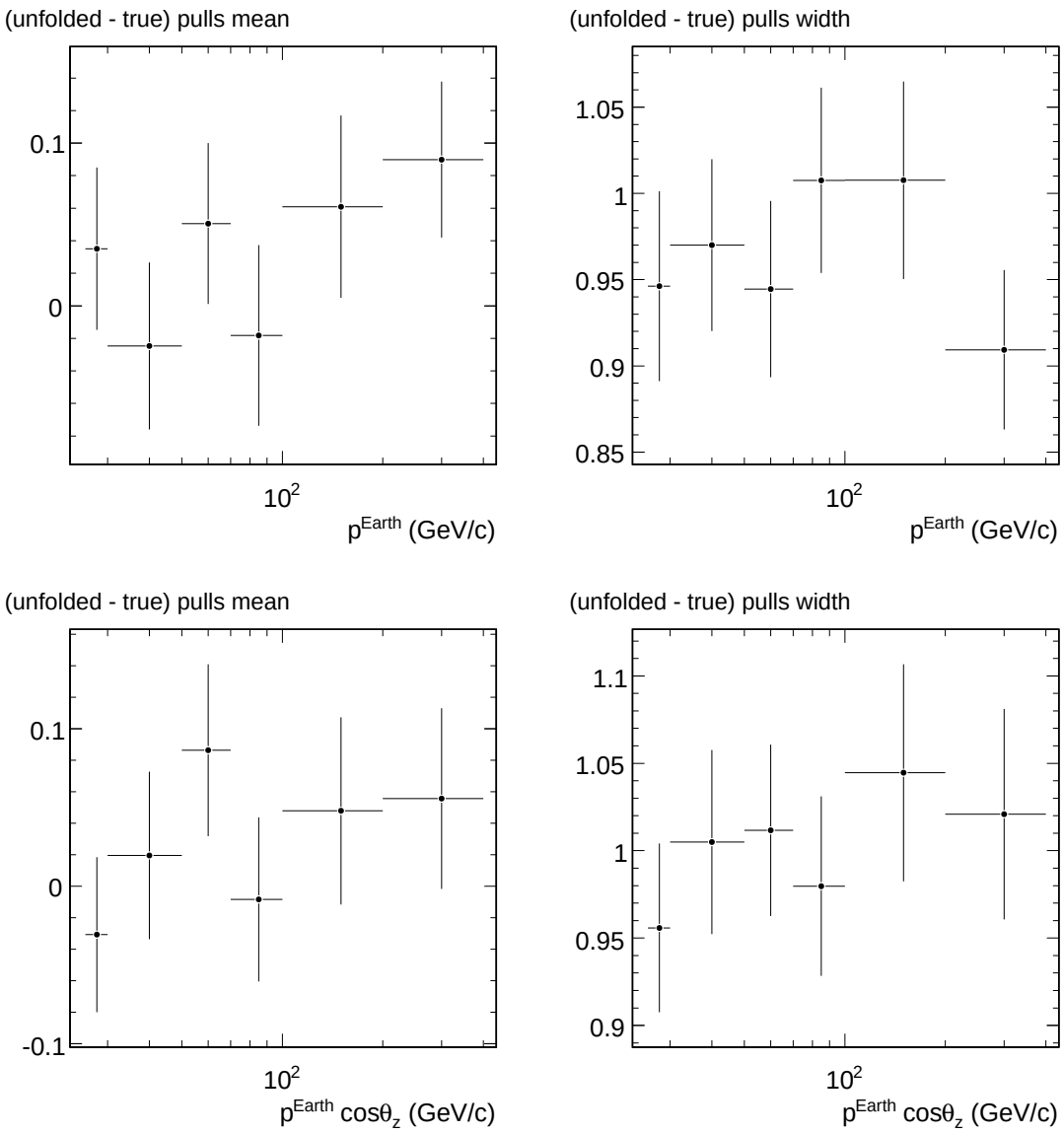

Figure 6-15. Charge ratio pulls distributions for 500 experiments. (Left) Pulls means. (Right) Pulls widths. (Top) In p bins. (Bottom) In $p\cos\theta_z$ bins.

Table 6-1. Selection relative biases in p bins

DT

p range (GeV/c)	R	σ/R (%) stat.	$\sqrt{\xi^2+\sigma_\xi^2}$	ξ	σ_ξ	ξ/σ_ξ
30 - 50	1.2682	1.15	2.56	-1.28	2.22	-0.58
50 - 70	1.3020	1.22	0.45	-0.42	0.17	-2.51
70 - 100	1.2745	0.87	0.18	-0.13	0.12	-1.04
100 - 200	1.2798	0.83	0.23	-0.20	0.12	-1.73
200 - 400	1.2945	1.60	0.27	0.16	0.22	0.74
400 - ∞	1.3493	3.53	0.62	-0.40	0.47	-0.85

SL2

p range (GeV/c)	R	σ/R (%) stat.	$\sqrt{\xi^2+\sigma_\xi^2}$	ξ	σ_ξ	ξ/σ_ξ
30 - 50	1.2682	1.15	1.12	-0.01	1.12	-0.01
50 - 70	1.3020	1.22	0.14	-0.11	0.09	-1.34
70 - 100	1.2745	0.87	0.18	-0.17	0.07	-2.44
100 - 200	1.2798	0.83	0.16	-0.14	0.07	-1.95
200 - 400	1.2945	1.60	0.16	0.05	0.15	0.36
400 - ∞	1.3493	3.53	0.44	0.29	0.33	0.87

TOB

p range (GeV/c)	R	σ/R (%) stat.	$\sqrt{\xi^2+\sigma_\xi^2}$	ξ	σ_ξ	ξ/σ_ξ
30 - 50	1.2682	1.15	1.75	0.89	1.51	0.59
50 - 70	1.3020	1.22	0.13	0.11	0.07	1.55
70 - 100	1.2745	0.87	0.06	0.04	0.04	0.99
100 - 200	1.2798	0.83	0.12	-0.12	0.04	-2.88
200 - 400	1.2945	1.60	0.17	-0.15	0.08	-1.89
400 - ∞	1.3493	3.53	0.59	-0.55	0.21	-2.61

χ^2

p range (GeV/c)	R	σ/R (%) stat.	$\sqrt{\xi^2+\sigma_\xi^2}$	ξ	σ_ξ	ξ/σ_ξ
30 - 50	1.2682	1.15	0.88	0.30	0.83	0.36
50 - 70	1.3020	1.22	0.13	-0.11	0.07	-1.71
70 - 100	1.2745	0.87	0.07	-0.05	0.06	-0.84
100 - 200	1.2798	0.83	0.11	0.08	0.07	1.03
200 - 400	1.2945	1.60	0.58	-0.55	0.19	-2.91
400 - ∞	1.3493	3.53	0.91	-0.75	0.52	-1.45

Table 6-2. Selection relative biases in $p\cos\theta_z$ bins

DT						
		σ/R (%)				
$p\cos\theta_z$ range (GeV/c)	R	stat.	$\sqrt{\xi^2+\sigma_\xi^2}$	ξ	σ_ξ	ξ/σ_ξ
30 - 50	1.2653	1.11	0.78	0.42	0.66	0.65
50 - 70	1.2795	0.85	0.85	-0.84	0.11	-7.59
70 - 100	1.2815	0.89	0.49	0.47	0.13	3.78
100 - 200	1.2913	1.04	0.16	0.02	0.15	0.14
200 - 400	1.3359	2.52	0.84	0.76	0.35	2.18
400 - ∞	1.4395	6.39	1.22	-0.88	0.85	-1.03
SL2						
		σ/R (%)				
$p\cos\theta_z$ range (GeV/c)	R	stat.	$\sqrt{\xi^2+\sigma_\xi^2}$	ξ	σ_ξ	ξ/σ_ξ
30 - 50	1.2653	1.11	0.35	-0.05	0.35	-0.14
50 - 70	1.2795	0.85	0.13	-0.12	0.06	-2.05
70 - 100	1.2815	0.89	0.21	-0.20	0.07	-2.67
100 - 200	1.2913	1.04	0.11	-0.04	0.10	-0.37
200 - 400	1.3359	2.52	0.26	0.10	0.24	0.42
400 - ∞	1.4395	6.39	0.83	0.60	0.57	1.04
TOB						
		σ/R (%)				
$p\cos\theta_z$ range (GeV/c)	R	stat.	$\sqrt{\xi^2+\sigma_\xi^2}$	ξ	σ_ξ	ξ/σ_ξ
30 - 50	1.2653	1.11	1.30	-1.17	0.56	-2.08
50 - 70	1.2795	0.85	0.11	-0.10	0.04	-2.31
70 - 100	1.2815	0.89	0.05	0.04	0.04	0.96
100 - 200	1.2913	1.04	0.10	0.08	0.05	1.82
200 - 400	1.3359	2.52	0.11	-0.01	0.11	-0.07
400 - ∞	1.4395	6.39	0.24	0.07	0.23	0.32
χ^2						
		σ/R (%)				
$p\cos\theta_z$ range (GeV/c)	R	stat.	$\sqrt{\xi^2+\sigma_\xi^2}$	ξ	σ_ξ	ξ/σ_ξ
30 - 50	1.2653	1.11	0.31	-0.14	0.28	-0.51
50 - 70	1.2795	0.85	0.09	-0.08	0.05	-1.72
70 - 100	1.2815	0.89	0.09	0.05	0.07	0.78
100 - 200	1.2913	1.04	0.22	-0.19	0.12	-1.55
200 - 400	1.3359	2.52	0.94	-0.87	0.36	-2.40
400 - ∞	1.4395	6.39	1.87	-1.53	1.09	-1.40

Table 6-3. Total systematic uncertainty

		σ/R (%)								
p range (GeV/c)	R	stat.	syst.	selection	alignment	B field	trigger	rates	rock	resolution
30 - 50	1.268	1.15	2.13	$\pm$1.59	$\mp$0.10	$\pm$0.20	$\mp$0.47	$\pm$1.30	$\mp$0.26	$\mp$0.04
50 - 70	1.302	1.22	0.63	$\pm$0.45	$\pm$0.01	$\mp$0.01	$\mp$0.25	$\pm$0.10	$\mp$0.35	$\mp$0.07
70 - 100	1.274	0.87	0.74	$\pm$0.14	$\pm$0.10	$\pm$0.01	$\mp$0.10	$\pm$0.10	$\pm$0.70	$\mp$0.03
100 - 200	1.280	0.83	0.33	$\pm$0.25	$\mp$0.08	$\mp$0.16	$\mp$0.01	$\pm$0.10	$\mp$0.04	$\mp$0.08
200 - 400	1.295	1.60	1.25	$\pm$0.59	$\mp$0.22	$\pm$0.44	$\pm$0.14	$\pm$0.10	$\pm$0.84	$\pm$0.48
400 - ∞	1.349	3.53	3.48	$\pm$1.01	$\mp$0.99	$\mp$2.55	$\pm$0.59	$\pm$0.10	$\pm$1.21	$\pm$1.33
		σ/R (%)								
$p\cos\theta_z$ range (GeV/c)	R	stat.	syst.	selection	alignment	B field	trigger	rates	rock	resolution
30 - 50	1.265	1.11	1.96	$\pm$1.25	$\mp$0.00	$\pm$0.10	$\pm$0.46	$\pm$1.39	$\mp$0.36	$\mp$0.05
50 - 70	1.280	0.85	1.00	$\pm$0.85	$\pm$0.10	$\mp$0.07	$\pm$0.09	$\pm$0.03	$\pm$0.51	$\mp$0.07
70 - 100	1.281	0.89	0.73	$\pm$0.48	$\mp$0.43	$\mp$0.13	$\pm$0.12	$\pm$0.03	$\mp$0.27	$\mp$0.10
100 - 200	1.291	1.04	0.60	$\pm$0.19	$\pm$0.18	$\pm$0.18	$\pm$0.02	$\pm$0.03	$\pm$0.49	$\pm$0.13
200 - 400	1.336	2.52	1.90	$\pm$1.16	$\pm$0.93	$\mp$0.67	$\pm$0.09	$\pm$0.03	$\pm$0.47	$\pm$0.86
400 - ∞	1.440	6.39	4.68	$\pm$1.76	$\pm$0.58	$\mp$2.39	$\mp$0.44	$\pm$0.03	$\pm$0.44	$\pm$3.52

CHAPTER 7
RESULT OF GLOBAL MUON ANALYSIS

The main focus of this dissertation is the measure of charge ratio in cosmic muons using global muon tracks. The results of this analysis, obtained using the methodology of Chapter 5 and with the calculation of systematic uncertainty as in Chapter 6, are presented here. The systematic uncertainties, broken down according to their source, are presented in Figure 7-1. The total error from all sources, statistical and systematic, are provided in Figure 7-2. The statistical and systematic uncertainties are found to be of roughly equal importance; combining for a total uncertainty of 2% in the lowest momentum bin, 5% in the highest bin, with a minimum of about 1% in between. The unfolded ratios of positive to negative muons is summarized in Table 7-1, and illustrated in Figure 7-3. It is observed that the charge ratio is approximately 1.27 (as predicted) at low momenta; and increasing at high momenta – up to about 1.4 above 600 GeV/c.

Because the final measurement of charge ratio is based on the combined results of all three analyses (the earth surface analysis, this analysis, plus the other underground analysis); the precise fits – such as the result for the fraction of pions and kaons producing muons – from this one analysis are not shown here. Instead, they may be found as a fit for all CMS data in the next chapter.

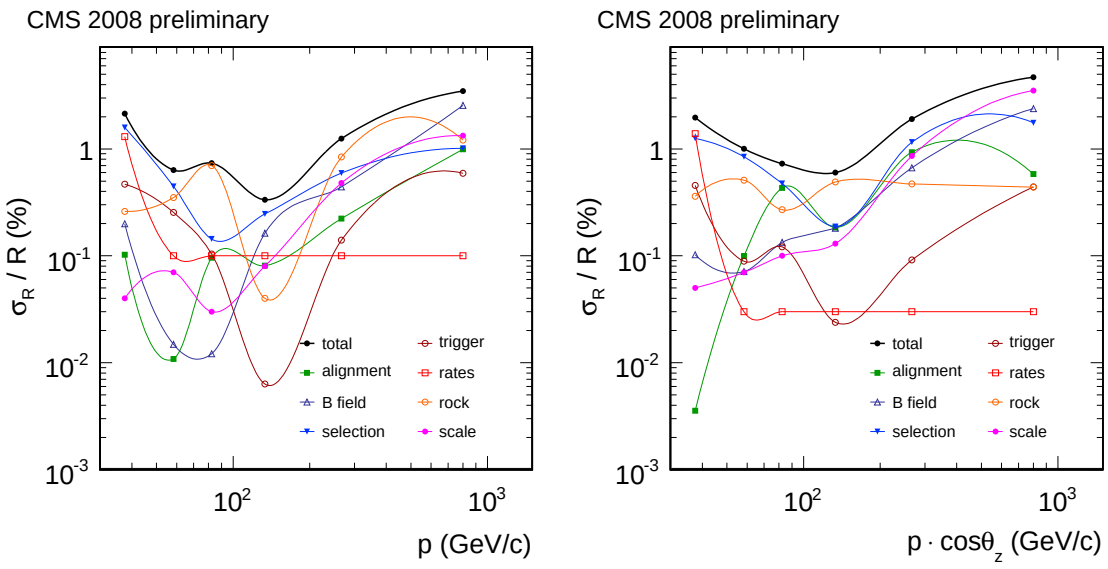

Figure 7-1. Individual systematic uncertainties for global muon analysis

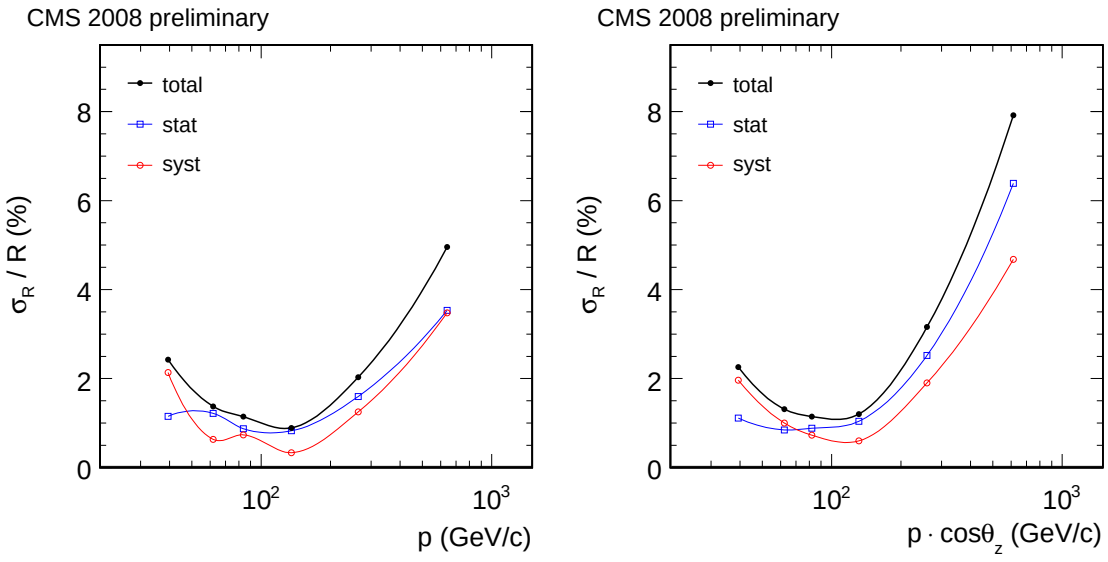

Figure 7-2. (Blue open squares) Measured charge ratio relative statistical uncertainties. (Black solid circles) Unfolded charge ratio relative statistical uncertainties. (Red lines) Unfolded charge ratio relative systematic uncertainties. Left: presented in p bins. Right: in $p\cos\theta_z$ bins.

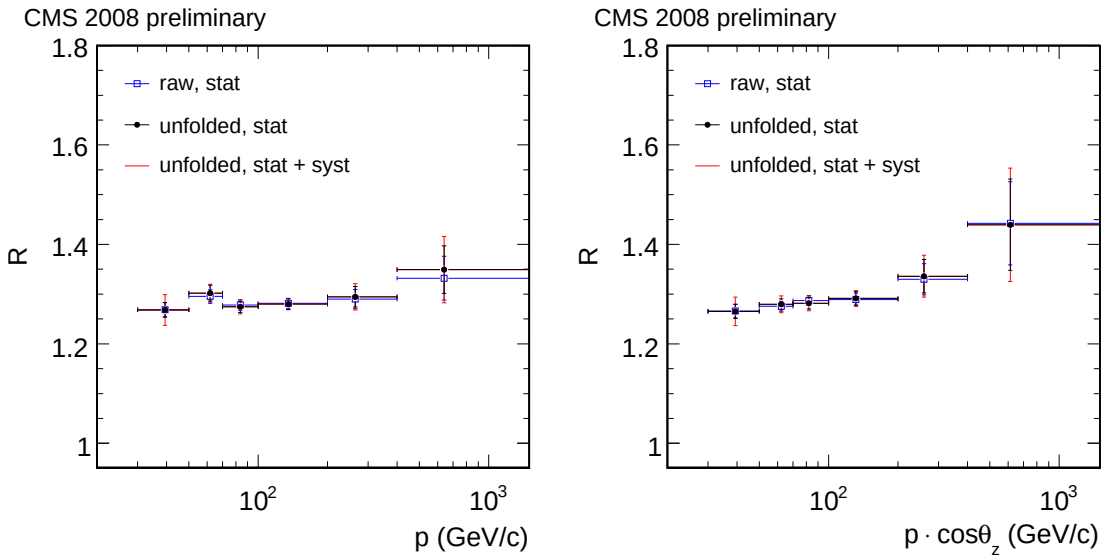

Figure 7-3. (Blue open squares) Measured charge ratio. (Black solid circles) Unfolded charge ratio, statistical error only. (Red lines) Statistical and systematic errors. Left: In p bins. Right: in $p\cos\theta_z$ bins.

Table 7-1. Unfolded charge ratio as a function of p and $p\cos\theta_z$ with all corrections applied, along with the statistical and systematic uncertainties.

p range (GeV/c)	average (GeV/c)	R	σ_{stat}	σ_{syst}
30 - 50	39	1.268 ± 0.031	0.015	0.027
50 - 70	62	1.302 ± 0.018	0.016	0.008
70 - 100	84	1.274 ± 0.015	0.011	0.009
100 - 200	135	1.280 ± 0.011	0.011	0.004
200 - 400	263	1.295 ± 0.026	0.021	0.016
400 - ∞	640	1.349 ± 0.067	0.048	0.047
$p\cos\theta_z$ range (GeV/c)	average (GeV/c)	R	σ_{stat}	σ_{syst}
30 - 50	39	1.265 ± 0.029	0.014	0.025
50 - 70	62	1.280 ± 0.017	0.011	0.013
70 - 100	82	1.281 ± 0.015	0.011	0.009
100 - 200	131	1.291 ± 0.016	0.013	0.008
200 - 400	259	1.336 ± 0.042	0.034	0.025
400 - ∞	613	1.440 ± 0.114	0.092	0.067

CHAPTER 8
COMBINED RESULT OF CHARGE RATIO MEASUREMENT

8.1 Systematic Uncertainties

Systematic uncertainties arise from reconstruction and instrumental effects that can affect differently the detection efficiency and momentum measurement of μ^+ and μ^-. They are evaluated as a function of the muon momentum estimated on the earth surface. The systematic uncertainties of the global muon CRAFT analysis were described in Chapter 6. The stand-alone muon analysis based on the same data-set had shared, or similarly estimated, errors; with a few differences, *eg.*, to produce an additional correction for charge mis-assignment. The MTCC uncertainties were largely based on the limited detector resolution, given the fact that it was only partially instrumented, and did not require many sophisticated error assessments since the data was collected on the earth surface.

Within each analysis, several of the systematic uncertainties are assumed to be correlated between momentum bins – including the trigger efficiency,[1] charge mis-assignment, and asymmetries in the detector acceptance. In the global and stand-alone muon analyses, systematic uncertainties from material densities, event selection, alignment, and magnetic field, are treated as uncorrelated between momentum bins; however correlated between the two analyses.

For the 2008 CRAFT (underground) analyses, the magnetic field is known with high precision in the region inside the superconducting solenoid, however with less precision in the steel return yoke [76]. Systematic effects on the charge ratio due to the uncertainty on the magnetic field are less than 1%. A possible bias in the positive and negative muon rates, due to asymmetries in detector acceptance and uncertainties in

[1] The trigger efficiency "turn-on" occurs around a few GeV/c – just enough to penetrate a few layers of the steel yoke – and much below the 10 GeV/c threshold used in the analyses.

the material densities used in the material map (known within 5%), yields a negligible uncertainty on the charge ratio except for in the lowest momentum bin. Additional biases due to selection are expected, however predicted to be small (below 1%). The hardware trigger has a slight asymmetry with regards to its efficiency on positive and negative muons, again less than 1%, and which is correlated between the two underground analyses. The effect of such trigger bias has been estimated using information from each half of the detector, using a so-called tag-and-probe technique to test for the presence of a trigger in one side given a trigger in the opposite side of the detector. In the 2006 MTCC (surface) analysis, systematic uncertainties arise mainly from the finite precision of the detector alignment parameters [82], from the correction of the charge mis-assignment probability, and from the slightly larger uncertainty, $\sim$5%, in the scale of the magnetic field in the steel return yoke.

In the global muon analysis, the effect of charge mis-assignment is small (due to the accurate momentum resolution within the silicon tracker), and ranges from less than 0.01% at 10 GeV/c to about 1% at 500 GeV/c. These mis-assignments are automatically corrected for in the unfolding procedure, using a data-driven estimation of the detector resolution. In the underground stand-alone muon analysis, charge mis-assignment is estimated and corrected for using the Monte Carlo simulation, with an additional uncertainty due to the difference of momentum resolution between the Monte Carlo and the data. Possible effects from potential residual mis-alignment that could lead to momentum migrations and incorrect charge assignments were evaluated by studying various realistic mis-alignment scenarios in data and simulation. Only the two highest momentum bins are potentially affected by such a mis-alignment, yielding a bias in the charge ratio around 1% in the two highest momentum bins for the global-muon analysis. For the standalone-muon analysis, the effect in the charge ratio is less than 1% up to 400GeV/c, and 4% in the highest momentum bin. The alignment uncertainties assumed in these analyses are well confirmed by the latest results from LHC collisions [83].

8.2 Measurement of the Cosmic Muon Charge Ratio

The results from the 2006 (earth surface) data are presented in Figure 8-1, both uncorrected and after applied corrections for energy loss in the detector and the rate of charge mis-assignment. Results from the two CRAFT analysis are presented, as observed within the detector at the PCA and as a function of transverse momentum, in Figure 8-2; and as a function of momentum at the earth surface, before and after corrections, in Figure 8-3.

The total systematic uncertainties in the three analyses are summarized in Table 8-1, as a function of p and $p\cos\theta_z$ at the Earth's surface. The final results of all three analyses are shown in Figure 8-4 as a function of the muon momentum. In the region where the results overlap, agreement between them is good; so the individual analyses are combined by constructing a covariance matrix of the results and using standard multi-variate analysis techniques [84, 85]. The resulting data points are given in Table 8-2 as a function of p and $p\cos\theta_z$. They are shown in Figure 8-4 (a) as a function of p, and in Figure 8-4 (b) as a function of $p\cos\theta_z$.

8.2.1 Measured Charge Ratio Below 100 GeV/c

In the region $p < 100$ GeV/c, there is a measurement of six p bins from the MTCC analysis and three p bins from the CRAFT analyses. The measured charge ratio in this range is treated as a constant, with these twelve data points combining to form a single measurement of the charge ratio using the same prescription for correlations between the analyses as in the previous section. The resulting measurement is found to be:

$$R = 1.2766 \pm 0.0032\,(\text{stat.}) \pm 0.0032\,(\text{syst.})\,,\ \frac{\chi^2}{ndf} = 7.3/11$$

This result is in good agreement with previous measurements [87–89] and represents a significant improvement in precision. For the vertical component, $p \cdot \cos\theta_z < 100$ GeV/c, the procedure is repeated; with the result:

$$R = 1.2772 \pm 0.0032\,(\text{stat.}) \pm 0.0036\,(\text{syst.})\,,\ \frac{\chi^2}{ndf} = 15.3/11$$

. . . where the slightly larger χ^2 is indicative that the fit is less consistent with the a constant charge ratio hypothesis. In the plots for $p \cdot \cos\theta_z$, the charge ratio is seen to begin rising before 100 GeV/c. Restricting the fit to 70 GeV/c or less yields a better (more constant) result:

$$R = 1.2728 \pm 0.0039\,(\text{stat.}) \pm 0.0040\,(\text{syst.})\,,\ \frac{\chi^2}{ndf} = 4.0/8$$

8.2.2 Charge Ratio Between 5 GeV/c and 1 TeV/c

Considering the full $p\cos\theta_z$ range measured, a sloped rise in the charge ratio is seen, as shown in Fig. 8-4. Comparing to previous measurements in the same momentum ranges, the CMS results agree well where there is overlap: with the L3+C measurement [87] below 400 GeV/c, and with the UTAH [86], MINOS [93] and OPERA [24] measurements above 400 GeV/c. Additional measurements from other experiments [23, 87–92] are not shown in the plot, however are similarly consistent with the result.

In Equation 1–3, the parameterized expression [25] for the charge ratio was given. A fit performed to the combined CMS charge ratio measurement, in the entire $p\cos\theta_z$ region, and with a fixed relative amount of kaon production, yields $f_\pi = 0.553 \pm 0.005$, and $f_K = 0.66 \pm 0.06$, with a $\chi^2/ndf = 7.8/7$. Figure 8-4 illustrates the fit to CMS data, together with a fit performed on previous measurements from L3+C and MINOS [26]. The value of f_π is consistent with the prediction of $R = 1.27$ for pions [27] cited in Chapter 1; as this result gives $R_\pi = 1.24 \pm 0.03$. The value of f_K yields $R_K = 2.0 \pm 0.5$ – the result indicates that the charge ratio in cosmic kaons is indeed higher than in pions.

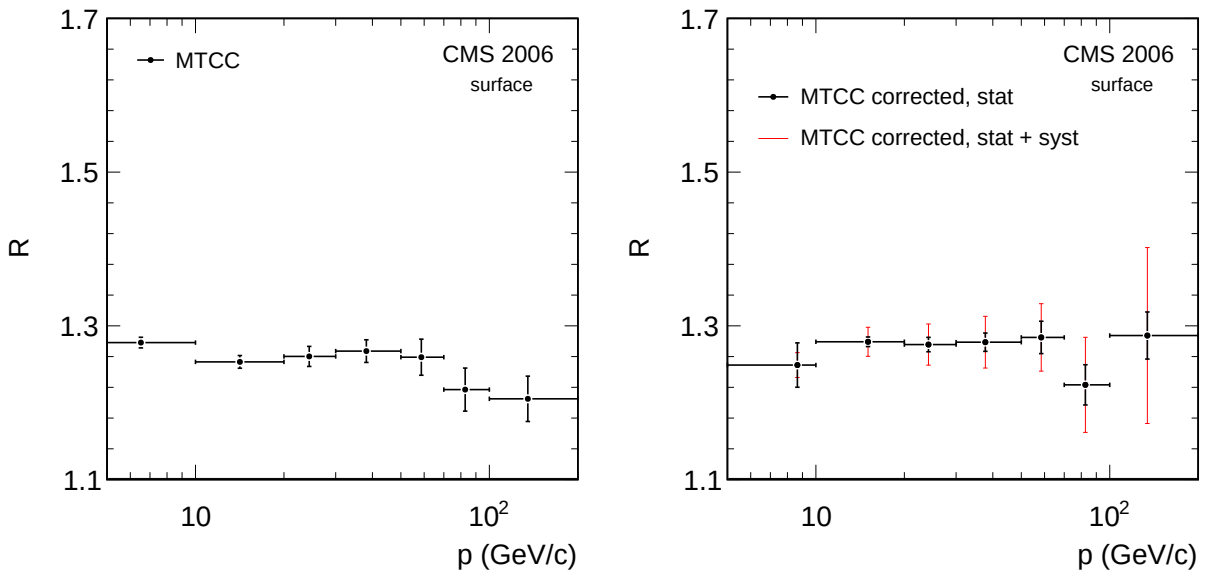

Figure 8-1. Results from 2006 MTCC analysis. Left: uncorrected charge ratio as a function of momentum. Right: charge ratio with corrections for energy loss within CMS and for charge mis-assignment as a function of momentum.

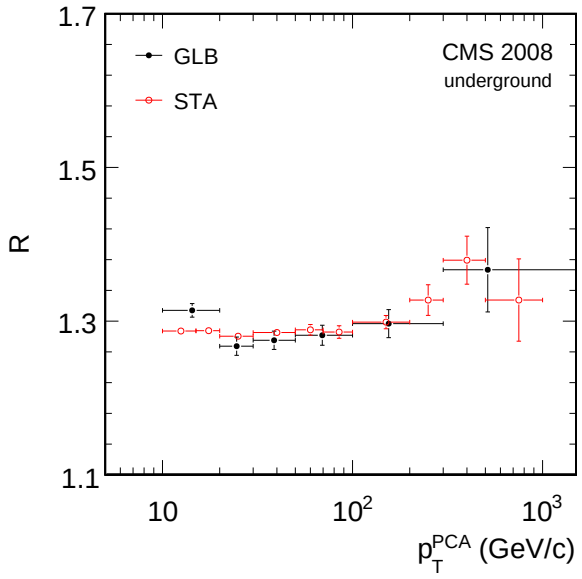

Figure 8-2. Result of 2008 CRAFT analyses. Cosmic muon charge ratio, uncorrected and measured at the PCA as a function of transverse momentum. Solid circles: global muon analysis. Red open circles: stand-alone muon analysis. Only statistical errors displayed.

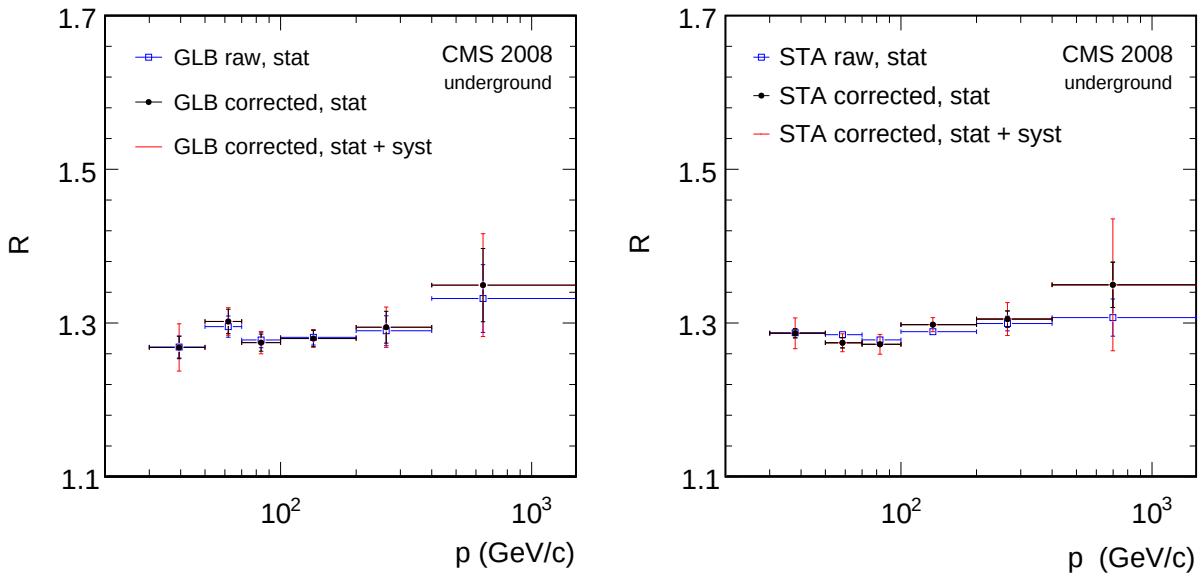

Figure 8-3. Result of 2008 CRAFT analyses. Cosmic muon charge ratio, extrapolated to the earth surface, as a function of the muon momentum at the earth surface. Left: global muon analysis. Right: stand-alone muon analysis. Open squares indicate the uncorrected, pre-unfolded ratio, and closed circles are the unfolded ratio with statistical error only. The lines denote statistical and systematic uncertainties added in quadrature.

Table 8-1. Charge ratio R and relative statistical (stat.) and systematic (syst.) uncertainties in bins of p (GeV/c), for surface data and from both analyses of underground data. The relative uncertainties are expressed in %.

p	2006 surface			2008 global-muon			2008 standalone-muon		
range	R	stat.	syst.	R	stat.	syst.	R	stat.	syst.
5 – 10	1.249	2.3	1.3	–	–	–	–	–	–
10 – 20	1.279	0.5	1.5	–	–	–	–	–	–
20 – 30	1.276	0.7	2.1	–	–	–	–	–	–
30 – 50	1.279	0.9	2.6	1.268	1.2	2.1	1.287	0.5	1.5
50 – 70	1.285	1.6	3.4	1.302	1.2	0.6	1.274	0.5	0.8
70 – 100	1.223	2.1	5.1	1.274	0.9	0.7	1.272	0.4	0.9
100 – 200	1.287	2.4	8.9	1.280	0.8	0.3	1.298	0.3	0.6
200 – 400	–	–	–	1.295	1.6	1.3	1.305	0.8	1.4
$>$ 400	–	–	–	1.349	3.5	3.5	1.350	2.2	6.0

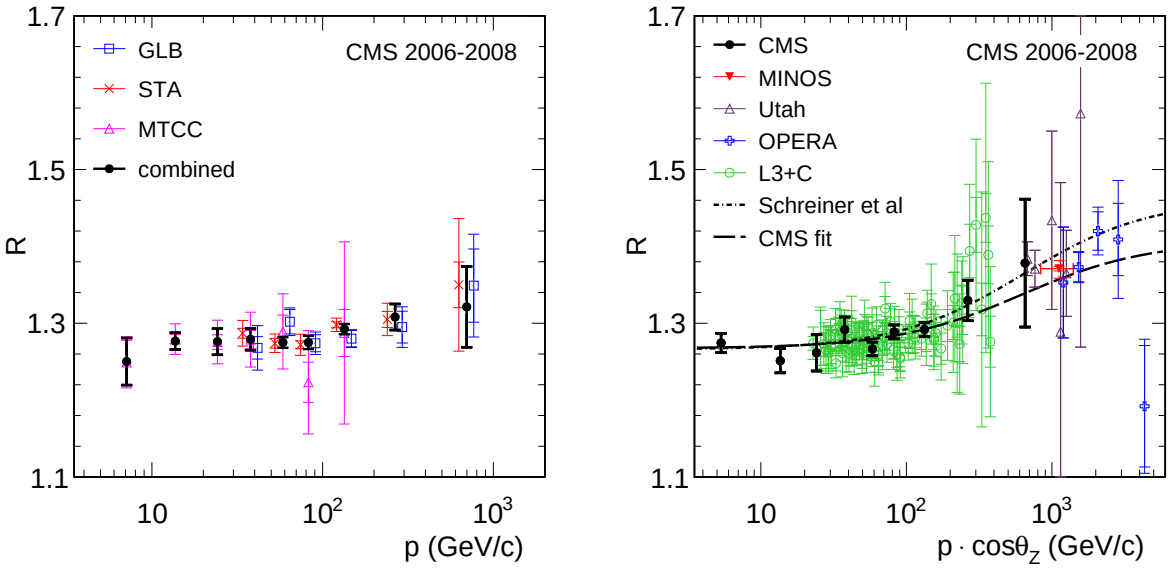

Figure 8-4. Combined result of charge ratio from all analyses. Left: the three CMS results, and their combination, as a function of the muon momentum. Data points are placed at the bin average, with the points from the stand-alone and global muon analyses offset horizontally by ±10% for clarity. Right: The final CMS result, as a function of the vertical component of the muon momentum, together with some previous measurements and a fit of the pion-kaon model to the CMS data.

Table 8-2. The muon charge ratio R from the combination of all three CMS analyses, as a function of p and $p\cos\theta_z$, in GeV/c, together with the combined statistical and systematic relative uncertainty, in %

p range	$\langle p \rangle$	R	uncertainty	$p\cos\theta_z$ range	$\langle p\cos\theta_z \rangle$	R	uncertainty
5 – 10	7.0	1.250	2.45	2.5 – 10	5.3	1.274	0.99
10 – 20	13.7	1.277	0.85	10 – 20	13.6	1.251	1.26
20 – 30	24.2	1.276	1.34	20 – 30	24.1	1.262	1.88
30 – 50	37.8	1.279	1.10	30 – 50	37.7	1.292	1.27
50 – 70	58.5	1.275	0.54	50 – 70	58.4	1.267	0.71
70 – 100	82.5	1.275	0.68	70 – 100	82.4	1.289	0.70
100 – 200	134.0	1.292	0.52	100 – 200	133.1	1.292	0.72
200 – 400	265.8	1.308	1.29	200 – 400	264.0	1.330	1.99
$>$ 400	698.0	1.321	3.98	$>$ 400	654.0	1.378	6.04

CHAPTER 9
CONCLUSIONS

Cosmic muons have provided the Compact Muon Solenoid with a wealth of useful data, which has been previously used for commissioning the detector [94–103], but has now been utilized to produce the first measurement of physics involving muons at the completed CMS detector. The ratio of positive to negative cosmic muon fluxes has been measured, and from this measurement; a new, precision estimate on the relative fractions of muon producing pion and kaon decays has been obtained [104, 105]. The final result for the measurement of the cosmic muon charge ratio from CMS – being combined from three separate analyses – is found to be in agreement with previous measurements, but with a higher precision up to a muon momenta of 500 GeV/c.

This dissertation detailed one of three analyses performed as part of the charge ratio measurement. The analysis was conducted on 2008 (underground) data, including information from both silicon tracking and muon spectrometers. In this analysis, data-driven techniques were used to estimate the detector resolution; the validity of which has been confirmed using numerous Monte Carlo tests, both idealized and realistic. Energy loss in the earth was estimated using an analytical extrapolator (with additional effects due to straggling energy losses accounted for) in order to convert measured particle curvatures within CMS to measurements at the surface of the earth, and a matrix unfolding technique was used to convert the measured particle counts into an estimate of the true particle counts.

APPENDIX A
TESTS OF THE DATA-DRIVEN RESOLUTION

A.1 Random Number Tests

A.1.1 Uncorrelated Measurements

In Section 5.4, the data-driven estimation of detector resolution is defined. In order to test the validity of such an estimator in general; a pair of random numbers, C_1 and C_2 (meant to be suggestive of the two independent measures of track curvature), are generated according to some resolution function – either Gaussian, exponential, or a superposition. As with the actual measures of curvature for the data, the half-sum gives the best approximation of the true value; however in this case, the distribution of the half-sum is centered on zero by construction, such that the half-sum is (also, by construction) equal to the resolution function. If the half-difference is identical to the half-sum within the limits of statistical uncertainty, it is therefore a valid description of the input resolution function.

Figure A-1 shows the agreement between the two resolutions if both of the measurements are Gaussian functions of the same width. In Figure A-2, both are generated according to the same exponential probability distribution. In both cases, the distributions of the half sum and half difference agree well. Although there is no reason to expect the resolution should be different between the top and bottom tracks, the test was also expanded to the unlikely scenario in which the two measurements are dominated by different resolution effects. In Figure A-3, one of the measurements has exponential smearing and the other has Gaussian, while in Figure A-4, both measurements are have the same Gaussian or exponential type of resolution, but one of the measurements is smeared a factor of three times more than other. In all cases there is quite good agreement between the half-sum and half-difference distributions, indicating that the half-difference represents the resolution well.

A.1.2 Selection on Independent Measures

A temptation in this analysis is to only accept events in which the top and bottom leg agree about the charge of the muon. To simulate how this affects the result, the distributions of the half-sum and half-difference are compared if events are accepted according to whether the two measurements agree on the sign of the measurement. The outcome is shown in Figure A-5, the two distributions disagree. In the weaker case, selection may be applied such that the difference between the measures is cut off at certain value, by selecting on events with curvatures which differ by no more than a set amount. The result is displayed in Figure A-6. Again, it is clear that the half-difference is a poor estimator of the true resolution.

From these tests, it is clear that the relative or absolute agreements between the measurements must *not* be used as a selection variable if the half-difference is to be used to estimate resolution effects. Such selection results in "sculpting" the half-difference, which does little more than hide the actual detector resolution.

A.2 Comparison with the Realistic Monte Carlo

The resolution estimator in Monte Carlo is compared with the data in Figure A-7, showing that the actual detector performance was relatively worse than the simulation predicts. The results are summarized in Figure A-8.

In Section 5.4, it was suggested that the half-difference between the two measurements was underestimating the true resolution; and in Figure 5-12, the amount of the necessary correction to convert the half-difference into a more accurate resolution estimator was defined. Figure A-9 gives the actual correlation between the top and bottom measures of curvature in the Monte Carlo, and shows that the two measurements *are* correlated with each other. The correlation is found to be nearly negligible for low momentum tracks, but increases significantly with momentum. Assuming Gaussian error distributions, the under-estimation factors (printed out in Table A.2) can be predicted via

an analytical formula. Assuming that the widths of the top and bottom measurements of curvature are the same ($\sigma_T = \sigma_B = \sigma$) then:

$$
\begin{aligned}
a &= \frac{1}{2}; \quad \sigma_1 = \sigma_2 = \sigma \\
C^+ &= a\,C_1 + a\,C_2 \\
C^- &= a\,C_1 - a\,C_2 \\
\sigma^+ &= a^2\sigma^2 + a^2\sigma^2 + 2a^2\ COV_{1,2} \\
\sigma^- &= a^2\sigma^2 + a^2\sigma^2 - 2a^2\ COV_{1,2} \\
\frac{\sigma^-}{\sigma^+} &= \sqrt{\frac{\sigma^2 - COV_{1,2}}{\sigma^2 + COV_{1,2}}} \\
\frac{\sigma^-}{\sigma^+} &= \sqrt{\frac{1 - \rho_{1,2}}{1 + \rho_{1,2}}}
\end{aligned}
\tag{A–1}
$$

The amount of correction required may be predicted by the strength of the covariance between the two measurements. In Table A.2, the predicted ratios are compared with those previously observed. In general, the predicted value is found to lie somewhat between the value from the Gaussian fit and the RMS; and furthermore, that the prediction agrees with the value obtained from the RMS to better than 10%.

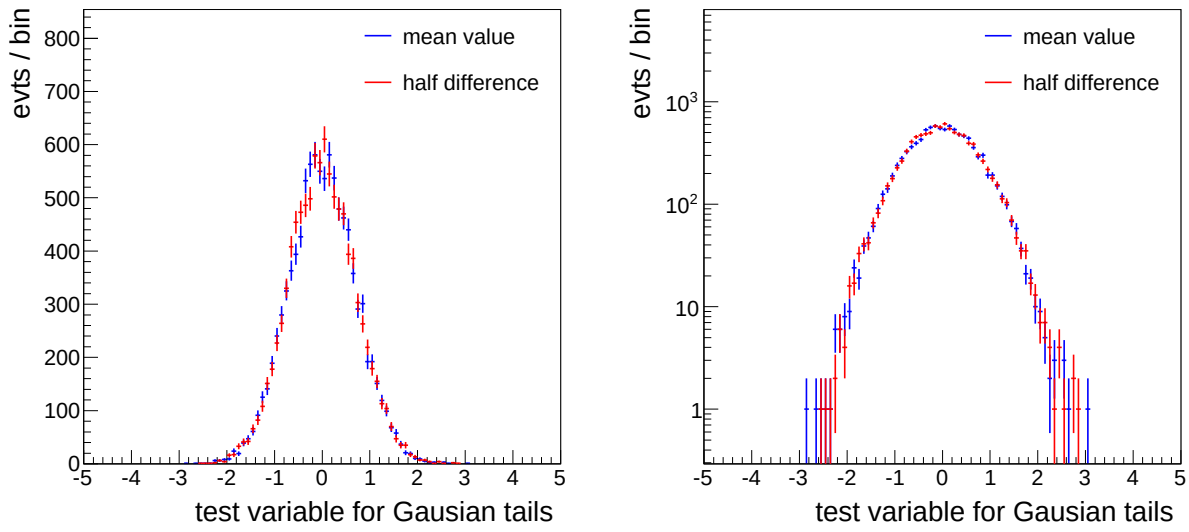

Figure A-1. Comparison of the half-sum and half-difference distributions for Gaussian smearing with the same resolution for top and bottom. In the left panel, in linear scale; in the right panel, logarithmic scale.

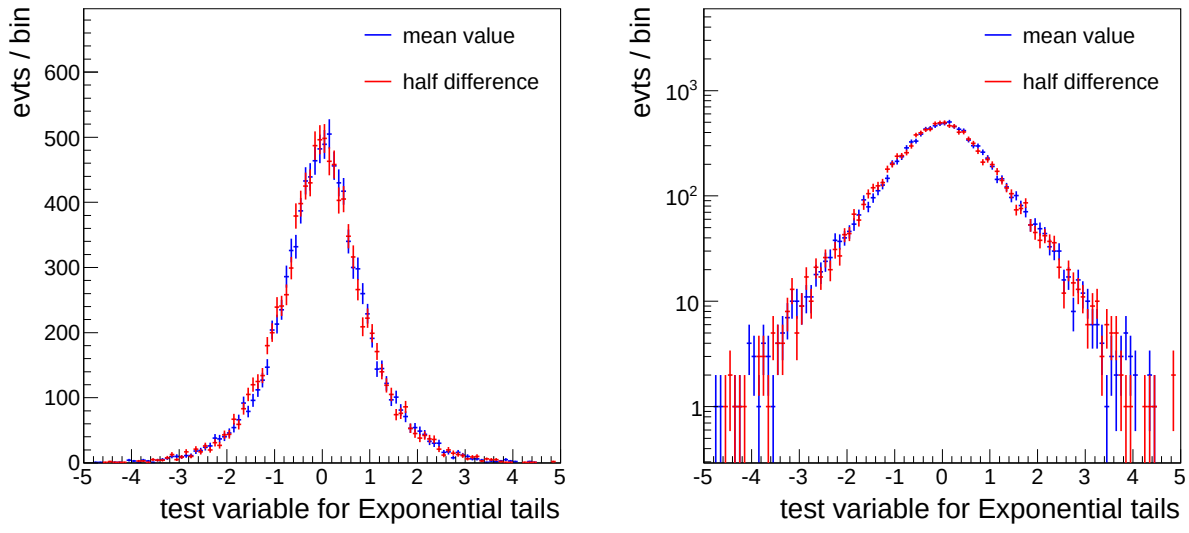

Figure A-2. Comparison of the half-sum and half-difference distributions for exponential smearing with the same resolution for top and bottom. In the left panel, in linear scale; in the right panel, logarithmic scale.

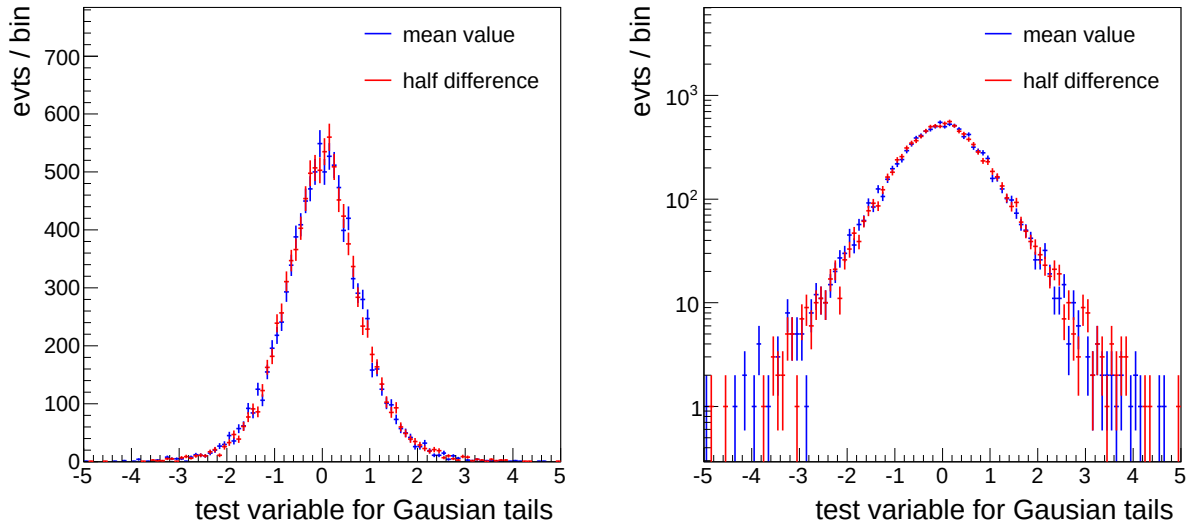

Figure A-3. Comparison of the half-sum and half-difference distributions for a combination of Gaussian and exponential smearing. In the left panel, in linear scale; in the right panel, logarithmic scale.

Table A-1. The corrections to the resolution, $\sigma(d_C)/\sigma(deltaC)$ and corresponding RMS ratios compared with the analytical prediction.

p_T^{PCA} range (GeV/c)	$\sigma(d_C)/\sigma(\delta C)$	$rms(d_C)/rms(\delta C)$	$\rho_{1,2}$[%]	predicted ratio
10 - 20	0.97	0.97	2.75	0.973
20 - 30	0.91	0.93	8.35	0.920
30 - 50	0.82	0.89	14.9	0.861
50 - 100	0.72	0.82	24.3	0.780
100 - 300	0.64	0.83	27.1	0.757
300 - ∞	0.59	0.88	19.2	0.823

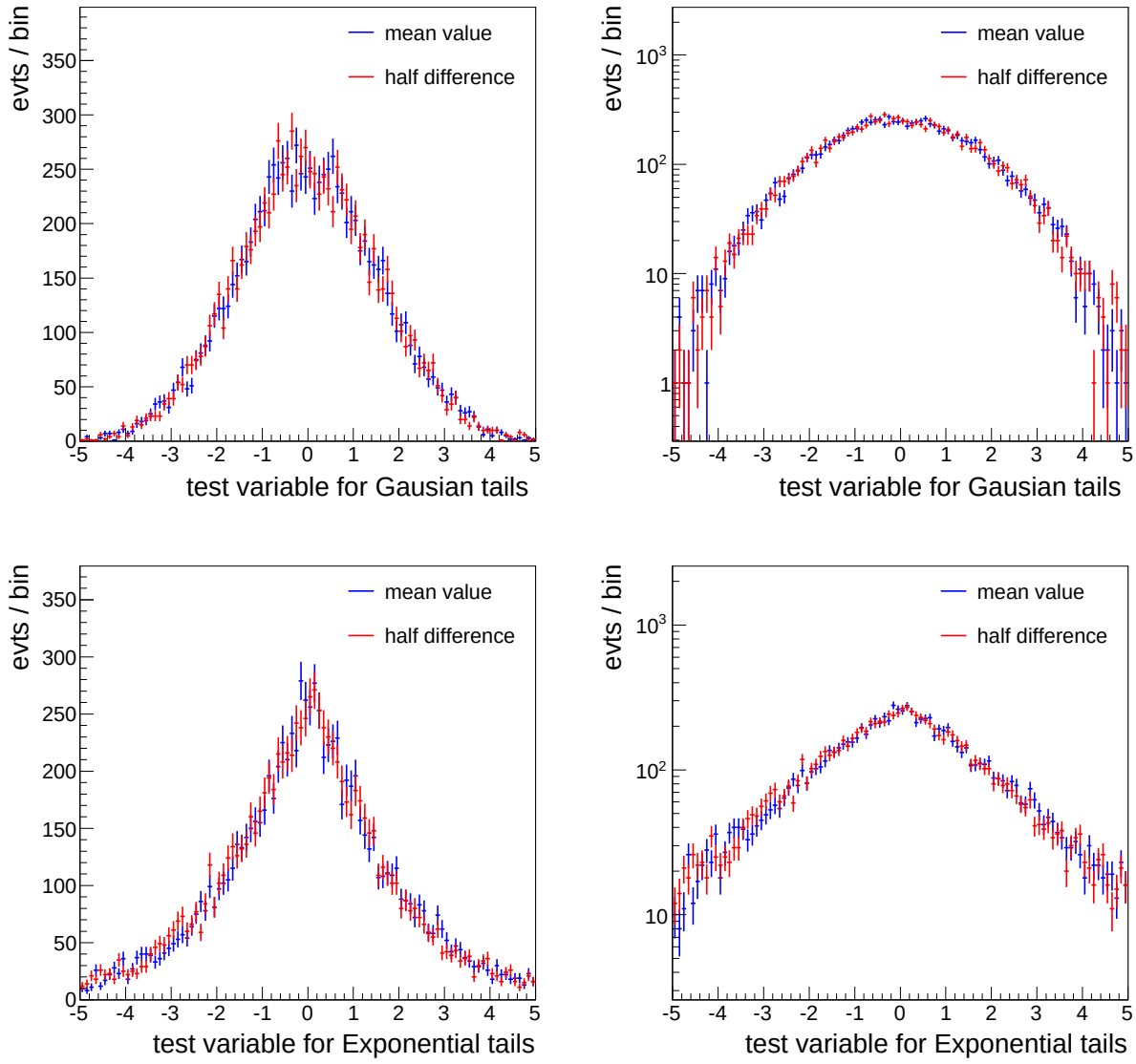

Figure A-4. Comparison of the half-sum and half-difference distributions for different resolutions between top and bottom. In the top left panel, Gaussian smearing where the resolution of one leg is three times worse than the other. In the top right panel, the same distribution in logarithmic scale. In the bottom left panel, exponential smearing where the lifetime for one leg is three times larger than the other. In the right panel, the same distribution in logarithmic scale.

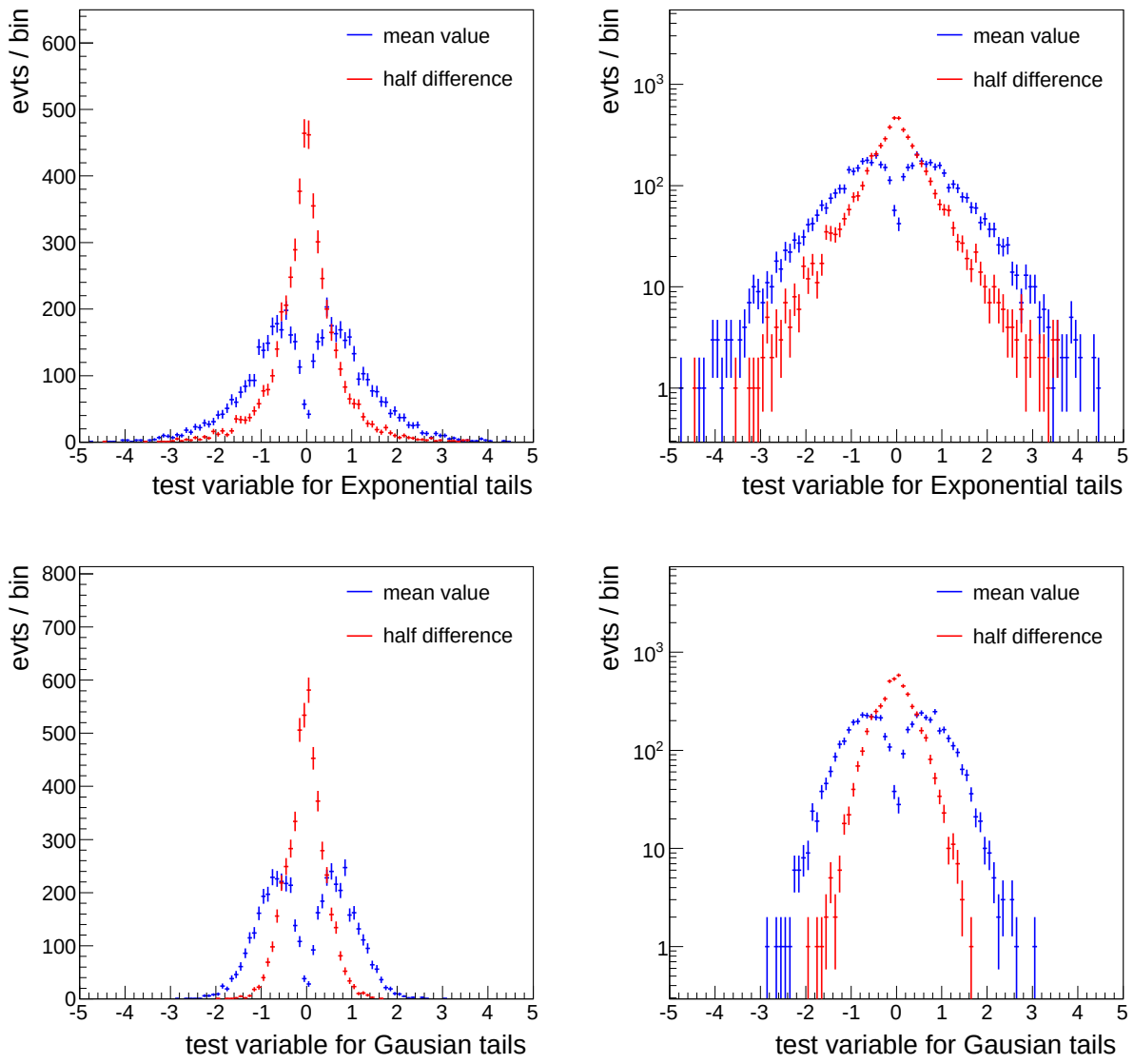

Figure A-5. Tests of the resolution function behavior when picking events in such a fashion as to "sculpt" the half-difference distribution by selecting on events which agree on curvature. Events were picked such that the curvature between the top and bottom leg agree.

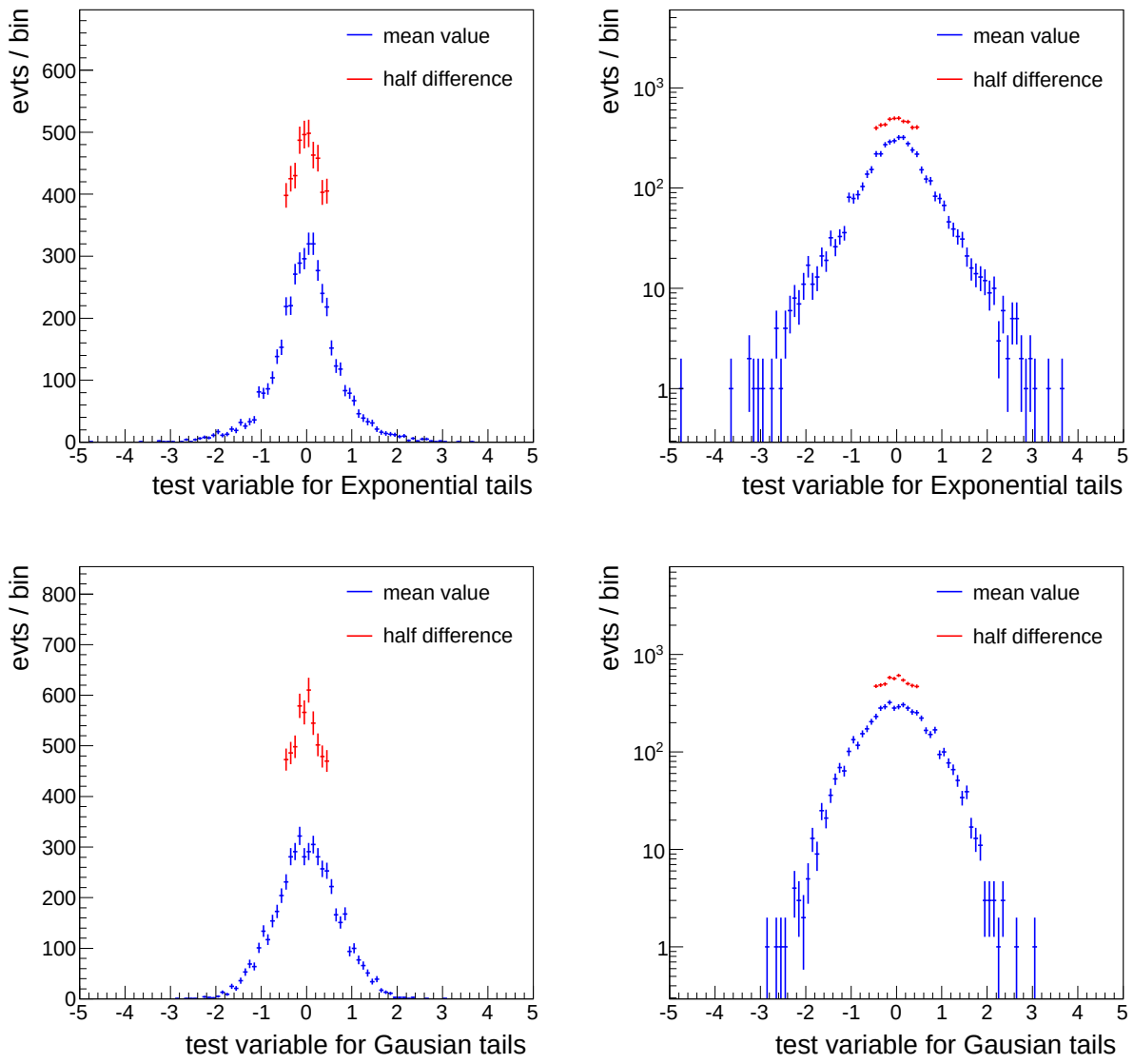

Figure A-6. Tests of the resolution function behavior when picking events in such a fashion as to “sculpt” the half-difference distribution by selecting on events which tend to agree on curvature. Events were picked such that the curvature difference is less than two between the top and bottom leg.

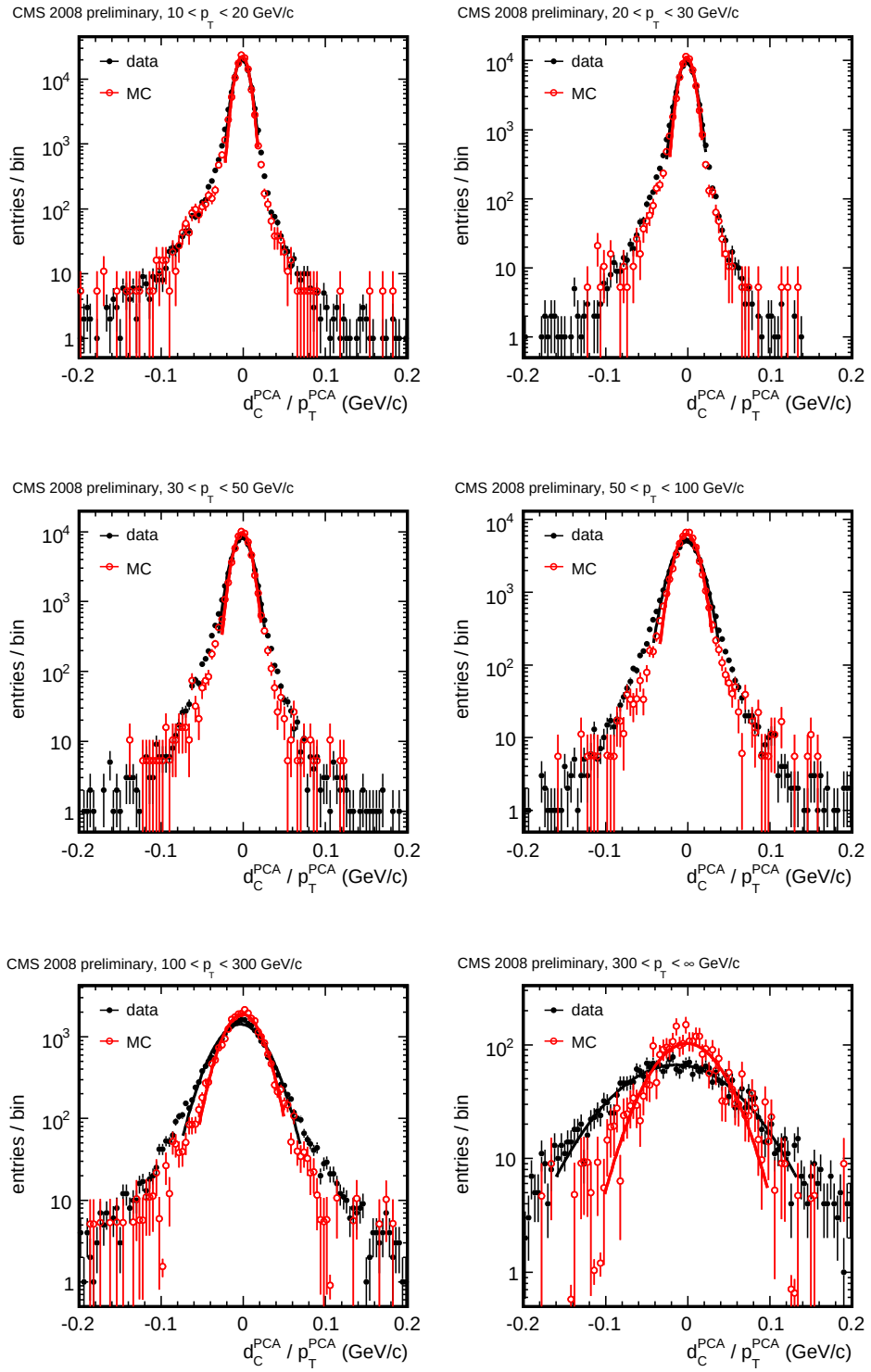

Figure A-7. Data (black solid circles) and Monte Carlo (red open circles) momentum resolution at the PCA in p_T^{PCA} bins.

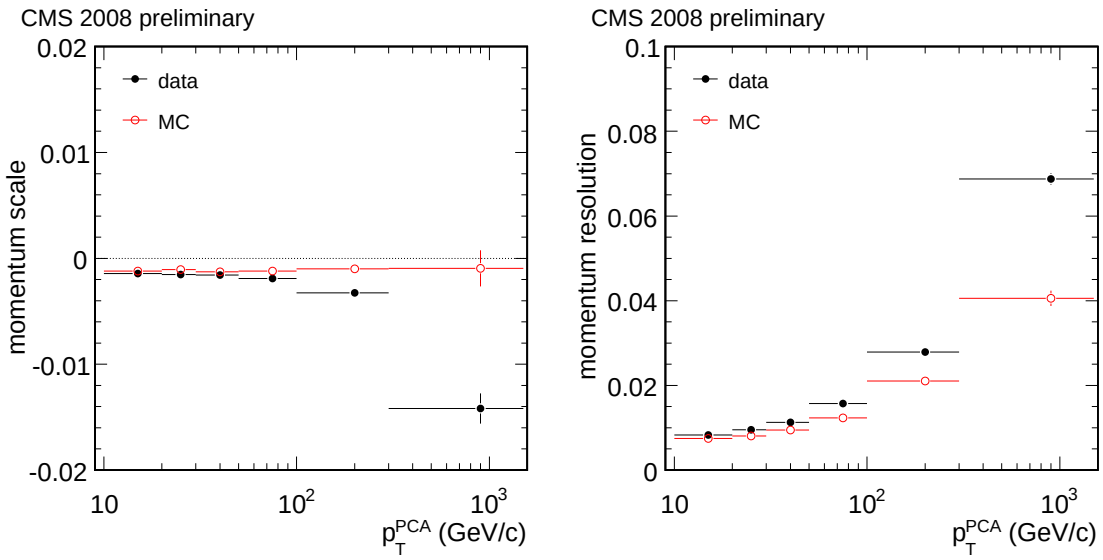

Figure A-8. Data (black solid circles) and Monte Carlo (red open circles). Left: mean value of Gaussian fits (momentum scale). Right: width of fits (momentum resolution).

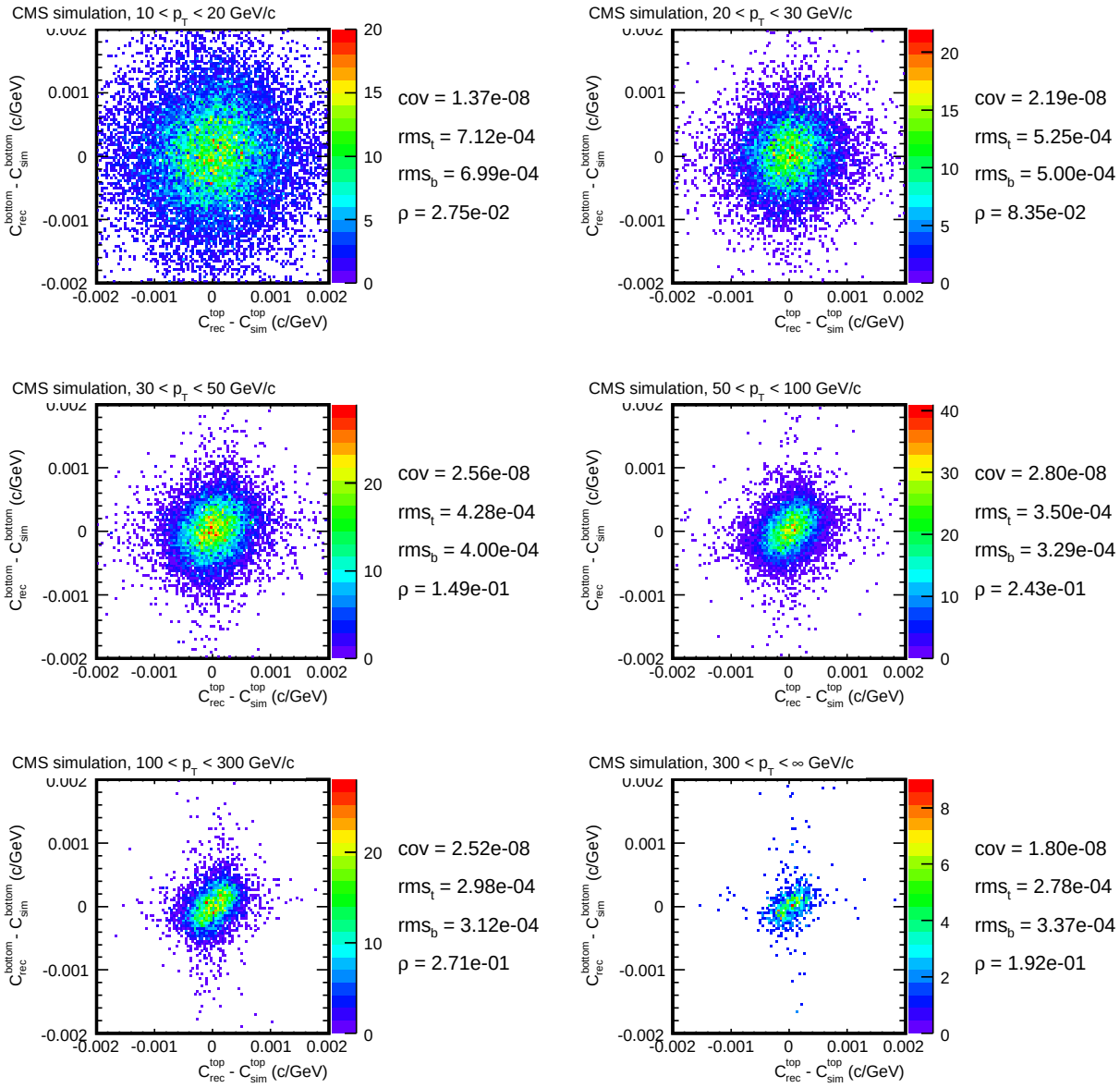

Figure A-9. Correlation between top and bottom individual true resolutions, in bins of true transverse momentum at the PCA.

APPENDIX B
ATMOSPHERIC DEPTH

B.1 Introduction

The CMS experiment is located at 46° 18′ 34” north latitude, 6° 4′ 37” east longitude; where ground-level is roughly 505 m above sea-level. The atmospheric conditions during CRAFT08 were measured using meteorological data reported by the Geneva Cointrin International Airport [106], approximately 5 miles away, and simulated to high altitudes using the NRLMSISE-00 (US Naval Research Laboratory, Mass Spectrometer and Incoherent Scatter Radar, Extended) model [107].

B.2 Measured Atmospheric Pressure

Published weather data is calibrated according to the station elevation; such that the reported pressures are actually extrapolations to sea-level, P_{msl}; rather than the actual $P_{station}$.[1] In order to convert the reported values to meaningful atmospheric densities, the data must be recalibrated to the appropriate altitude – in this case; from sea-level, to the station elevation (430 m) and finally, to the elevation above Point-5 (505 m). These conversions are performed by applying the ideal gas relation, Equation B–1.

$$P = P_0 \cdot e^{\frac{-h \cdot M \cdot g}{R \cdot T}} \tag{B–1}$$

Here, h is the altitudinal difference between P and P_0, M is the molecular weight of the gas, g is acceleration due to gravity, T is temperature in Kelvin, and R is the gas constant. The International Standard Atmosphere (ISA) was used for this study: $g = 9.807$, $M = 28.964\ g/mol$, and $R = 8.3145\ J/K \cdot mol$.

[1] This is so that isobar pressure contour maps are not unduly influenced by topography; but complicates any application of the data in this context.

B.3 Effective Elevation

The effective elevation, in terms of atmospheric depth, is quite fluid with time. It may be computed by solving Equation B–1 for h, using the standard atmospheric pressure (101.325 kPa for the ISA) as its reference pressure. The resulting elevation as a function of time is presented in Figure B-3.

B.4 Atmospheric Density

The local air density, near ground level, may be measured [108] from:

$$\rho = \frac{(P_d \cdot M_d + P_v \cdot M_v)}{R \cdot T} \tag{B–2}$$

. . . where P_d and P_v are the partial pressures of dry air and water vapor, T is the temperature in Kelvin, R is the universal gas constant, and M_d and M_v are the molecular weights of dry air and water vapor, respectively. The partial pressure of water vapor was computed using the Lowe [109] approximation (which depends only on the measured dewpoint temperature).[2]

B.5 NRLMSISE-00 Atmospheric Simulation

NRLMSISE-00 is typically used for atmospheric simulations in rocketry and satellite applications, but suits the requirements of this study well. The model was used to simulate the atmospheric densities above CMS as a function of both time and altitude, using the main drivers of the upper atmosphere – solar ultra-violet radiation [110] and geomagnetic heating [111] as inputs. Low altitude meteoroligical effects are accounted for indirectly by simulating from the effective, atmospheric altitude (computed previously) rather than the true elevation.

The air density at ground level, computed from the weather station data using Equation B–2, and simulated directly in NRLMSISE-00, is illustrated in Figure B-2.

[2] The polynomial approximation introduces a negligible error – thousandths of a percent – presumed much smaller than the measurement accuracy.

The *high altitude* uncertainties on the NRLMSISE-00 model have been solved elsewhere using low orbital satellite data [112], and has been found to vary from 10-15% up to around 200 km, rising to a maximum of 30% at altitudes near 600 km. By comparison with measured values (after correcting for elevation) an error of at most 2% is observed at ground level.

The resulting, altitude dependent, simulations of atmospheric density are indicated in Figure B-1. Also indicated in the figure are the total (altitude dependent) variations in the resulting densities (over the duration of the experiment), and the theoretical uncertainty. Nearly all of the integrated atmospheric mass is in the first 30 km above ground level, where the total error and time-dependent variations are quite small.

B.6 Summary

The effective elevation, considering the mass of air above CMS as a function of time during the 2008 CRAFT exercise is given in Figure B-3. Given that the earth material is at least 1500 times more dense than air, the 500 m elevation of the surface at CMS is equivalent to no more than 30 cm of moraine. Including atmospheric effects, the effective altitude during CRAFT varied from just below 300 m to more than 600 m; or between 24 cm and 36 cm of moraine equivalent. Given that material uncertainty above CMS is already 5 m of moraines, no additional uncertainty is expected from the small variations in the atmosphere.

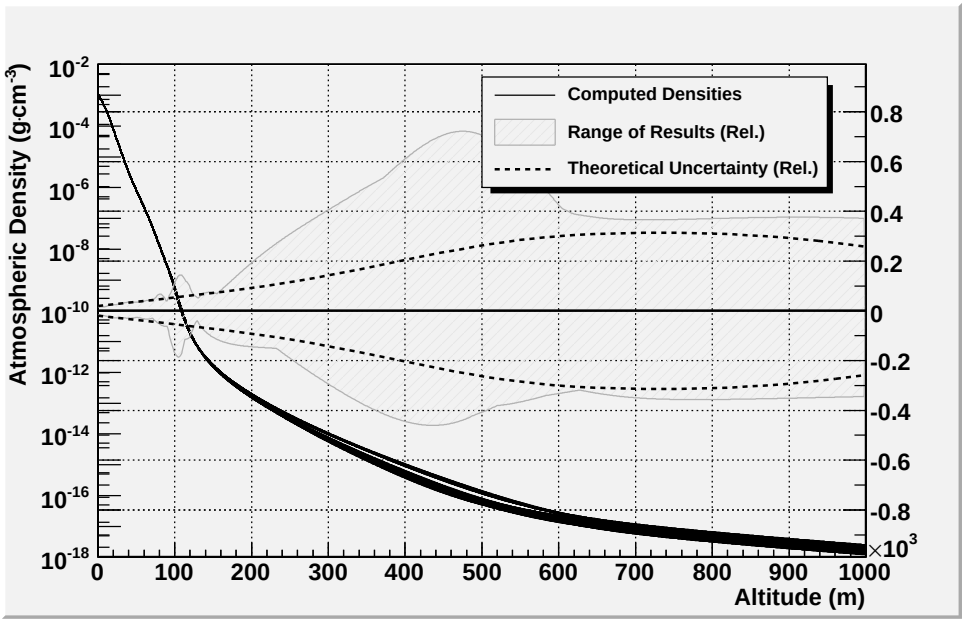

Figure B-1. Air densities as a function of altitude during CRAFT08 using NRLMSISE-00.

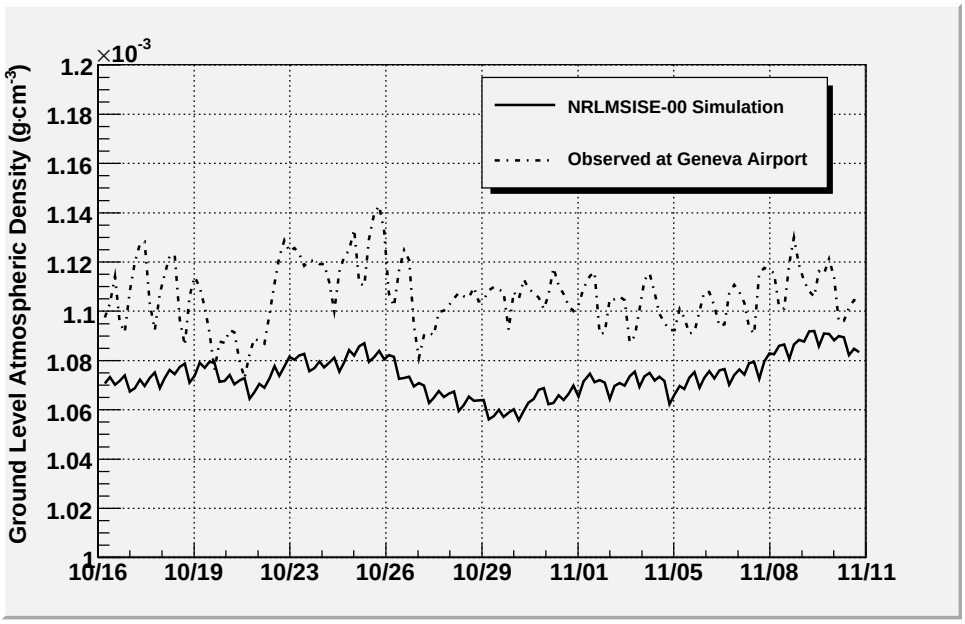

Figure B-2. Air densities at ground level: measured from Geneva International Airport data and simulated using NRLMSISE-00.

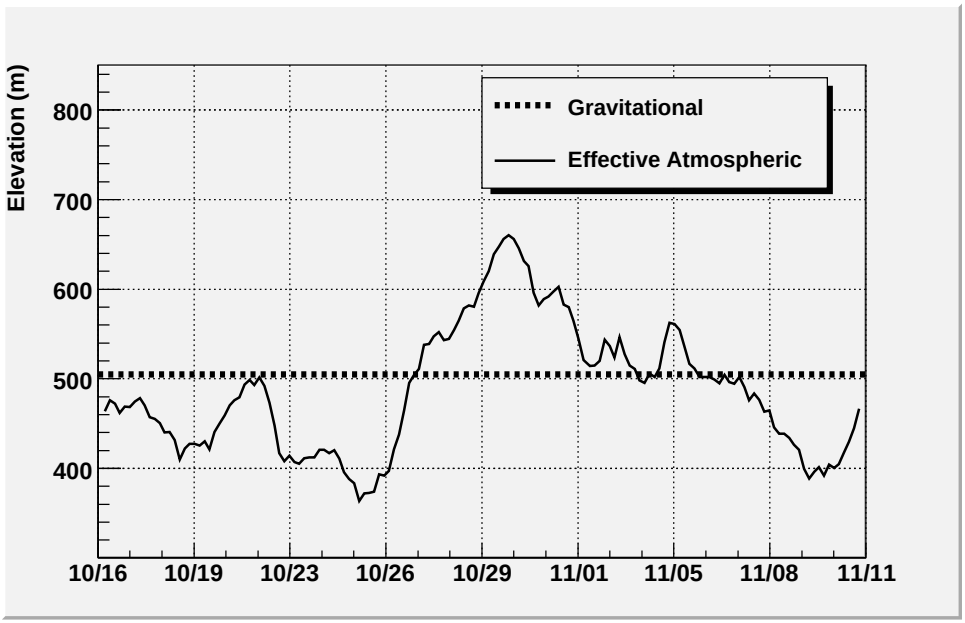

Figure B-3. The effective elevation of ground level above CMS during the time of the experiment, using data published by the Geneva Airport.

.

REFERENCES

[1] T. Wulf, "About the radiation of high penetration capacity contained in the atmosphere," *Physikalische Zeitschrift*, 1910.

[2] J. R. Partington, "Discovery of Radon," *Nature*, vol. 179, pp. 912, 1957.

[3] V. F. Hess, "About the absorption of gamma rays in the atmosphere," *Physikalische Zeitschrift*, 1911.

[4] V. F. Hess, "About Observations of the Penetration through-going Radiation During 7 Balloon Flights," *Physikalische Zeitschrift*, 1912.

[5] D. Pacini, "La radiazione penetrante alla superficie ed in seno alle acque," *Il Nuovo Cimento Serie VI*, vol. 3, pp. 93–100, 1912.

[6] R. Millikan, "Cosmic-Ray Ionization and Electroscope-Constants as a Function of Pressure," *Phys. Rev.*, vol. 39, pp. 397–402, 1931.

[7] A. H. Compton, "An Apparent Effect of Galactic Rotation on the Intensity of Cosmic Rays", *Phys. Rev.*, vol. 47, pp. 817–821, 1935.

[8] B. Rossi, "Directional Measurements of the Cosmic Rays Near the Geomagnetic Equator," *Phys. Rev.*, vol. 45, n. 3, pp. 212–214, 1934 .

[9] C. D. Anderson and S. H. Neddermeyer, "Cloud Chamber Observations of Cosmic Rays at 4300 Meters Elevation and Near Sea-Level," *Phys. Rev.*, vol. 50, pp. 263–271, Aug. 1936.

[10] S. H. Neddermeyer and C. D. Anderson, "Note on the nature of cosmic-ray particles," *Phys. Rev.*, vol 51, pp. 884–886, Mar. 1937.

[11] C. F. Powell, *et al.*, "Processes Involving Charged Mesons," *Nature* vol. 159, pp. 694–697., 1947.

[12] J. A. Van Allen, "The Nature and Intensity of the Cosmic Radiation," Physics and Medicine of the Upper Atmosphere, *The University of New Mexico Press*, Albuquerque, pp. 239–266, 1952.

[13] B. Rossi, "Cosmic Rays," *McGraw-Hill*, New York, 1964.

[14] A. M. Hillas, "Cosmic Rays," *Pergamon Press*, Oxford, 1972.

[15] Y. Uchiyama, F. A. Aharonian, T. Tanaka, T. Takahashi, and Y. Maeda, "Extremely fast acceleration of cosmic rays in a supernova remnant," *Nature*, vol. 449, pp 576–578, Oct. 2007.

[16] The Pierre Auger Collaboration, "Correlation of the Highest-Energy Cosmic Rays with Nearby Extragalactic Objects," *Science*, vol. 318, n. 5852, pp. 938–943, Nov. 2007.

[17] F. Fraschetti, "On the acceleration of ultra-high-energy cosmic rays," *Phil. Trans. R. Soc.*, vol. 366, pp. 4417–4428, 2008.

[18] J. D. Hague, "Correlation of the highest energy cosmic rays with nearby extragalactic objects in Pierre Auger Observatory data," presented at the 31st International Cosmic Ray Conference, Łódź, Poland, July 2009.

[19] T. Stanev, "High Energy Cosmic Rays," 2nd Edition, *Springer Berlin Heidelberg*, 2009.

[20] T. K. Gaisser and T. Stanev, *et al.*, "Review of Particle Physics (2008) and 2009 partial update for the 2010 edition (http://pdg.lbl.gov)," *Phys. Lett. B.*, vol. 667, Jan. 2010.

[21] S. P. Swordy, "The Energy Spectra and Anisotropies of Cosmic Rays," *Space Science Reviews*, vol. 99, pp. 85–94, 2001.

[22] K. Yoshida, R. Ohmori, T. Kobayashi, Y. Komori, Y. Sato, and J. Nishimura, "Cosmic-ray spectra of primary protons and high altitude muons deconvolved from observed atmospheric gamma rays," *Phys. Rev. D*, vol. 74, pp. 083511, Oct. 2006.

[23] T. Hebbeker and C. Timmermans, "A Compilation of High Energy Atmospheric Muon Data at Sea Level," *Astropart. Phys.*, vol. 18, pp. 107–127, 2002.

[24] OPERA Collaboration, "Measurement of the atmospheric muon charge ratio with the OPERA detector", *submitted to Eur. Phys. J.*, 2010.

[25] T. K. Gaisser, "Cosmic Rays and Particle Physics," *Cambridge University Press*, 1990.

[26] P. A. Schreiner, J. Reichenbacher, and M. C. Goodman, "Interpretation of the Underground Muon Charge Ratio", *Astropart. Phys.*, vol. 32, issue 1, pp. 61, 2009.

[27] G. Fiorentini, V. Naumov, and F. Villante, "Atmospheric neutrino flux supported by recent muon experiments", *Phys. Lett. B*, vol. 510, pp. 173, 2001.

[28] O. Brüning, P. Collier, P. Lebrun, S. Myers, R. Ostojic, J. Poole, P. Proudlock, *et al.*, "LHC Design Report", CERN-2004-003-V-2, 2004.

[29] J. Evans and P. Bryant, "LHC Machine", *JINST*, vol. 3, pp. S08001, 2008.

[30] CERN, published to the web: "http://lhc-proj-qawg.web.cern.ch/lhc-proj-qawg/LHCQAP/Instructions/images/maplhc.gif," "Map of CERN sites and LHC access points," retrieved on Feb. 4th, 2010.

[31] CMS Collaboration, "CMS Technical Design Report", CERN-LHCC-94-38, 1994.

[32] CMS Collaboration, "The CMS Experiment at the CERN LHC", *JINST* vol. 3, pp. S08004, 2008.

[33] ATLAS Collaboration, "ATLAS detector and physics performance. Technical design report. Vol. 2," ATLAS-TDR-15, 1999.

[34] TOTEM Collaboration, "TOTEM: Technical design report. Total cross section, elastic scattering and diffraction dissociation at the Large Hadron Collider at CERN," CERN-LHCC-2004-002, Jan. 2004.

[35] LHCf Collaboration, "Technical Design Report of the LHCf experiment," CERN-LHCC-2006-004, Feb. 2006.

[36] Alice Collaboration, "The alice experiment at the CERN LHC," *Nucl. Phys. B - Proc. Suppl.*, vol. 117, supp. 1, pp. 62–64, Apr. 2003.

[37] LHCb Collaboration, "LHCb: Technical Proposal," CERN-LHCC-98-004, 1998.

[38] M. Chirnside, "The 66,000 Ton Myth," *The Irish Titanic Historical Society's White Star Journal*," vol. 15, no. 3, pp. 20–21, 2007.

[39] J. Bryner, published to the web: "http://www.livescience.com/technology/091103-cruise-ship-floats.html", "How the World's Largest Cruise Ship Floats," *LiveScience.com*, Nov. 2009.

[40] A. Robb, "Optical geometry of motion, a new view of the theory of relativity," *Cambridge University Press: Heffner and Sons*, 1911.

[41] CERN, "ATLAS cavern ready for its detector," *CERN Courier*, Jul. 1st, 2003.

[42] CERN, "CMS cavern ready for its detector," *CERN Courier*, Mar. 1st, 2005.

[43] CMS Collaboration, published to the web: "http://cms.web.cern.ch/cms/Media," retrieved on Feb. 7th, 2010.

[44] CMS Collaboration, "CMS Magnet Technical Design Report", CERN-LHCC-97-10, 1997.

[45] CMS Collaboration, "CMS Tracker Technical Design Report", CERN-LHCC-98-6, 1998; Addendum CERN-LHCC-2000-16, 2000.

[46] M. Teckenbrock, "Making Good Things Fit in Small Packages," *CD Tracks Newsletter*, Nov. 2008.

[47] CMS Collaboration, "CMS ECAL Technical Design Report", CERN-LHCC-97-33, 1997.

[48] CMS Collaboration, "CMS HCAL Technical Design Report", CERN-LHCC-97-31, 1997.

[49] CMS Collaboration, "CMS Muon Technical Design Report", CERN-LHCC-97-32, 1997.

[50] M. Aldaya and P. Garcia-Abia, "Measurement of the charge ratio of cosmic muons using CMS data" CMS-NOTE 2008/016.

[51] M. Aldaya, P. Garcia-Abia, M. Mulders, "Updated measurement of the charge ratio of cosmic muons using MTCC data," CMS-NOTE AN-2010/011, 2010.

[52] CMS Collaboration, "The CMS Magnet Test and Cosmic Challenge", CMS-NOTE 2007/005, 2007.

[53] A. Ball and A. Sharma, "CMS collaboration takes on a cosmic challenge," *CERN Courier*, Mar. 2nd, 2007.

[54] D. Lazic for the CMS Collaboration, "The CMS Magnet Test and Cosmic Challenge (MTCC) Operational Experience and Lessons Learnt," *Nucl. Phys. B – Proceedings Supplements*, vol. 172, pp. 3–7, Oct. 2007.

[55] CMS Collaboration, "Commissioning of the CMS experiment and the cosmic run at four tesla", *JINST* vol. 5, pp. T03001, 2010.

[56] CMS Collaboration, "CMS Trigger Technical Design Report", CERN-LHCC-2000-38, 2000.

[57] A. Calderon, U. Gasparini, A. Gresele, A. Fanfani, S. Marcellini, *et al.*, "Measurement of Charge Ratio in Cosmic Rays using Standalone Muon Reconstruction in CRAFT Data," CMS-NOTE AN-2010/013, 2010.

[58] I. K. Furic, T. N. Kypreos, J. Piedra, and P. Avery, D. Bourilkov, M. Chen, R. Cousins, C. Jiang, C. Liu, N. Neumeister, Y. Pakhotin, J. Pivarski, A. Safanov, M. Schmitt, J. Tucker, *et al.*, "Measurement of the Charge Ratio in Cosmic Rays using Global Muon Reconstruction in CRAFT Data," CMS-NOTE AN-2009/102, 2009.

[59] I. K. Furic, T. N. Kypreos, J. Piedra, and P. Avery, D. Bourilkov, M. Chen, R. Cousins, C. Jiang, C. Liu, N. Neumeister, Y. Pakhotin, J. Pivarski, A. Safanov, M. Schmitt, J. Tucker, *et al.*, "Upgraded Measurement of the Charge Ratio of Cosmic Rays using Global Muon Reconstruction in CRAFT Data," CMS-NOTE AN-2009/190, 2009.

[60] J. Piedra, "Measurement of the cosmic muon charge asymmetry," presented at the Europhysics Conference on High Energy Physics, Krakow, Poland, 2009.

[61] CMS Collaboration, "CMS Physics Technical Design Report (Volume 1)," CERN-LHCC-2006-02, 2006.

[62] W. Adam, *et al.*, "Track and vertex reconstruction in CMS," *Nuclear Instruments and Methods in Physics Research Section A*, vol. 582, issue 3, pp. 781–784, Dec. 2007.

[63] C. Liu, *et al.* "Reconstruction of cosmic and beam-halo muons with the CMS detector," *Eur. Phys. J. C*, vol. 56, pp. 449–460, Jul. 2008.

[64] MACRO Collaboration, "The Observation of Upgoing Charged Particles Produced by High Energy Muons in Underground Detectors," *Astropart. Phys.*, vol. 9, issue 2, pp. 105–117, Aug. 1998.

[65] P. Biallass and T. Hebbeker, "Parametrization of the Cosmic Muon Flux for the Generator CMSCGEN," *arXiv:0907.5514* [astro-ph.IM], Jul. 2009.

[66] D. Heck et al., "CORSIKA, A Monte Carlo to simulate Extensive Air Showers", *Forschungszentrum Karlsruhe, Report FZKA*, 1998.

[67] L. Sonnenschein for the CMS Collaboration, "CMS: Cosmic muons in simulation and measured data," presented at the Workshop on Neutrino Physics at CERN, Geneva, Switzerland, 2009.

[68] L. Sonnenschein for the CMS Collaboration, "CMS: Cosmic muons in simulation and measured data," presented at the XXth Hadron Collider Physics Symposium, Evian, France, 2009.

[69] L. Sonnenschein for the CMS Collaboration, "Cosmic muons in simulation and measured data", presented at the XXIV International Symposium on Lepton Photon Interactions at High Energies, Hamburg, Germany, Aug. 2009.

[70] S. Agostinelli et al., "GEANT4: A simulation toolkit", *Nucl. Inst. Meth. A* vol. 506, pp. 250, 2003.

[71] G. Cowan, "A Survey of Unfolding Methods for Particle Physics," presented at the Conference on Advanced Statistical Techniques in Particle Physics, Durham, England, Mar. 2002.

[72] A. Höcker and V. Kartvelishvili, "SVD Approach to Data Unfolding," *Nuclear Instruments and Methods in Physics Research Section A*, vol. 372, issue 3, no. 1, pp. 469–481, Apr. 1996.

[73] G.D'Agostini, "A multidimensional unfolding method based on Bayes theorem," *Nuclear Instruments and Methods in Physics Research Section A*, vol. 362, issue 2-3, pp. 487–498, Aug. 1995.

[74] CMS Collaboration, "Performance of CMS muon reconstruction in cosmic-ray events", *JINST*, vol. 5, pp. T03022, 2010.

[75] G. Flucke *et al.*, "CMS silicon tracker alignment strategy with the Millepede II algorithm", *JINST*, vol. 3, pp. P09002, 2008.

[76] CMS Collaboration, "Precise mapping of the magnetic field in the CMS barrel yoke using cosmic rays", *JINST* vol. 5, pp. T03021, 2010.

[77] S. Ivy-Ochs, H. Kerschner, A. Reuther, F. Preusser, K. Heine, M. Maisch, P. Kubik, and C. Schluchter, "Chronology of the last glacial cycle in the European Alps," *Journal of Quaternary Science*, vol. 23, issue 6-7, pp. 559–573, Aug. 2008.

[78] Géotechnique Appliquée Dériaz S.A., "Projet LHC - Reconnaissances de la molasse - Rapport de synthése," Jul. 1997.

[79] H. Rammer, "Two New Caverns for LHC Experiments: ATLAS and CMS," presented at the CERN-ST Workshop, Chamonix, France, 1998.

[80] CMS Collaboration, "Alignment of the CMS muon system with cosmic-ray and beam-halo muons", *JINST*, vol. 5, pp. T03020, 2010.

[81] CMS Collaboration, "Alignment of the CMS silicon tracker during commissioning with cosmic rays", *JINST*, vol. 5, pp. T03009, 2010.

[82] CMS Collaboration, "Simulation of Cosmic Muons and Comparison with Data from the Cosmic Challenge using Drift Tube Chambers," CMS-NOTE, 2007.

[83] CMS Collaboration, "Tracking and Vertexing Results from First Collisions", CMS-PAS, 2010.

[84] L. Lyons, D. Gibaut, and P. Clifford, "How to Combine Correlated Estimates of a Single Physical Quantity", *Nucl. Inst. Meth. A*, vol. 270, pp. 110, 1988.

[85] A. Valassi, "Combining correlated measurements of several different physical quantities", *Nucl. Inst. Meth. A*, vol. 500, pp. 391, 2003.

[86] G. K. Ashley, J. W. Keuffel, and M. O. Larson, "Charge ratio of ultra-high-energy cosmic-ray muons," *Phys. Rev. D*, vol. 12, no. 1, pp. 20, 1975.

[87] L3 Collaboration, "Measurement of the atmospheric muon spectrum from 20 to 3000 GeV", *Phys. Lett. B* vol. 598, pp. 15, 2004.

[88] J. M. Baxendale, C. J. Hume, and M. G. Thompson, "Precise measurement of the sea level muon charge ratio," *J. Phys. G: Nucl. Phys.* vol. 1, pp. 781, 1975.

[89] B. C. Rastin, "An accurate measurement of the sea-level muon spectrum within the range 4 to 3000 GeV/c," *J. Phys. G: Nucl. Phys.* vol. 10, pp. 1629, 1984.

[90] CAPRICE Collaboration, "Measurements of Ground-Level Muons at Two Geomagnetic Locations," *Phys. Rev. Lett.*, vol. 83, pp. 4241–4244, Jul. 1999.

[91] ALEPH Collaboration, "Cosmic Ray Results from the CosmoALEPH Experiment," *Nucl. Phys. B – Proc. Suppl.*, vol. 175–176, pp. 286–293, Nov. 2007.

[92] BESS Collaboration, "Cosmic ray data and their interpretation: about BESS experiment," *Nucl. Phys. B Proc. Suppl.*, vol. 149, pp. 175–176, 2008.

[93] MINOS Collaboration, "Measurement of the atmospheric muon charge ratio at TeV energies with MINOS," *Phys. Rev. D*, vol. 76, pp. 052003, 2007.

[94] A. C. Tazon for the CMS Collaboration, "Muon reconstruction performance using cosmic rays in CMS," presented at Symmetries and Spin Workshop (Prague Advanced Study Institute), Prague, Czech Republic, 2009.

[95] CMS Collaboration, "Commissioning the CMS Silicon Strip Tracker prior to Operations with Cosmic Ray Muons," *CMS Note*, NOTE-2009/021, 2009.

[96] G. Kaussen for the CMS Tracker Collaboration, "The CMS Strip Tracker Calibration, Methods and Experience with Cosmic Ray Data," presented at the IEEE

Nuclear Science Symposium and Medical Imaging Conference, Orlando, Florida, 2009.

[97] M. Dinardo for the CMS Tracker Collaboration, "Cosmic Ray Study of the CMS Pixel Tracker," presented at the IEEE Nuclear Science Symposium and Medical Imaging Conference, Orlando, Florida, 2009.

[98] R. Rougny for the CMS Tracker Collaboration, "Commissioning the CMS pixel detector with Cosmic Rays," presented at the 11th ICATPP Conference on Astoparticle, Particle, Space Physics, Detectors and Medical Physics Applications, Villa Olmo, Italy, 2009.

[99] M. Malberti for the CMS ECAL Collaboration, "Commissioning of the CMS ECAL calibration with muons from cosmic rays and beam dumps," presented at the IEEE Nuclear Science Symposium and Medical Imaging Conference, Orlando, Florida, 2009.

[100] V. Hagopian for the CMS HCAL Collaboration, "The Performance of the CMS Hadron Calorimeter with Cosmic Muons," presented at the 11th ICATPP Conference on Astoparticle, Particle, Space Physics, Detectors and Medical Physics Applications, Villa Olmo, Italy, Oct. 2009.

[101] T. Maki for the CMS Collaboration, "Commissioning the CMS trigger with cosmic rays," presented at the Europhysics Conference on High Energy Physics, Krakow, Poland, 2009.

[102] S. Bansal, J. B. Singh, K. Muzamdar, I. Mikulec, "Data driven methods for estimation of L1 trigger efficiency using CRAFT08 Cosmic Muon data," *CMS Note*, IN-2009/024, 2009.

[103] D. Piccolo for the CMS Muon Collaboration, "Resistive Plate Chambers performance with Cosmic Rays in the CMS experiment," presented at the 11th Pisa Meeting on Advanced Detectors: Frontier Detectors for Frontier Physics, Pisa, Italy, 2009.

[104] CMS Collaboration, "Measurement of the charge asymmetry of atmospheric muons with the CMS detector," CMS-PAS, 2010.

[105] CMS Collaboration, "Measurement of the charge ratio of atmospheric muons with the CMS detector," arXiv:1005.5332v1 [hep-ex], *submitted to Phys. Lett. B*, 2010.

[106] Weather Underground, published to the web: "http://www.wunderground.com/history/airport/LSGG," "History for Geneva, Switzerland (Meteorological Data)," retrieved on Mar. 10th, 2010.

[107] J. M. Picone, A. E. Hedin, D. P. Drob, and A. C. Aikin, "NRLMSISE-00 empirical model of the atmosphere: Statistical comparisons and scientific issues," *J. Geophys. Res.*, vol. 107, pp. 1468, Dec. 2002.

[108] W. Brutsaert, "Evaporation Into the Atmosphere," *D. Reidel Publishing Company*, pp. 37–38, 2007.

[109] P. R. Lowe, "An Approximating Polynomial for the Computation of Saturation Vapor Pressure," *Journal of Applied Meterology*, vol. 16, no. 1, pp. 100–103, Jan. 1977.

[110] NOAA Space Weather Prediction Center, published to the web: "http://www.swpc.noaa.gov/ftpdir/indices/old_indices/2008_DGD.txt," "Daily Geomagnetic Data 2008," Jan. 2009.

[111] NOAA National Geophysical Data Center, published to the web: "ftp://ftp.ngdc.noaa.gov/STP/SOLAR_DATA/SOLAR_RADIO/FLUX/2008.ADJ," "Adjusted Daily Solar Flux 2008," Jan. 2009.

[112] F. A. Marcos, B. R. Bowman and R. E. Sheehan, "Accuracy of earth's themospheric neutral density models," *Amer. Inst. of Aero. and Astro.*, pp. 6167, 2006.

BIOGRAPHICAL SKETCH

Michael Schmitt is a fifth generation Floridian, born in Hollywood Florida. From a young age Michael was eager to discover the workings of the world around him. He graduated from high school in 1999 and post graduation began pursuing higher education at Palm Beach Community College. During his enrollment at Palm Beach Community College, he received academic recognition many times. Among these include the President's Honor Certificate and an honor for Academic Excellence in mathematics.

Michael began his undergraduate work at the University of Florida in August of 2001 and sought hands on experience as a Demonstration Laboratory Assistant. In 2002, he took on additional responsibilities as an Undergraduate Research Assistant working on the Collider Detector at Fermilab, based near Chicago. He received his Bachelor's of Science degree (with a major of Physics) with highest honors in 2003, and was granted an Alumni Fellowship position with the Univerity of Florida.

Over the past seven years, Michael has been a teaching assistant, a research assistant on two major particle physics collaborations, and a wonderful husband. He is an incredibly diverse and knowledgeable individual, who is looking forward to a future where he can continue to learn, develop, and overcome new challenges.

Photograph of the author standing in front of the *z*-minus end-cap of the CMS detector (at a height of three to four stories) taken on September 20th, 2006. At this time, CMS was in the midst of a “cosmic-shutdown”; MTCC (Phase-I) ended in August, but would resume in October (Phase-II). On November 2nd, five weeks after this photograph was taken, the machine began its piecemeal descent 100 m into the earth; a process which would take fourteen months to complete. Another nine months would pass before the data on which this thesis was based could be collected. *Thanks to Dr. Arno Heister for taking this photograph*.